© Copyright [2018]

Yifeng Liu

Study of Size Reduction, Reliability and Lead Safety of an Intra-Cochlear Lead-Zirconate-Titanate Micro-Actuator

Yifeng Liu

A dissertation
submitted in partial fulfillment of the
requirements for the degree of

Doctor of Philosophy

University of Washington
2018

Reading Committee:

I. Y. (Steve) Shen, Chair
Guozhong Cao
Junlan Wang

Program Authorized to Offer Degree:

Mechanical Engineering

University of Washington

Abstract

Study of Size Reduction, Reliability and Lead Safety of an Intra-Cochlear Lead-Zirconate-Titanate Micro-Actuator

Yifeng Liu

Co-Chairs of the Supervisory Committee:

Professor I.Y.(Steve) Shen

Department of Mechanical Engineering

Professor Guozhong Cao

Department of Material Science and Engineering

To rehabilitate hearing loss, researchers have developed hearing aids with combined electric and acoustic stimulations to attain better speech recognition in the last decade. Such hearing aids incorporate an electrode array implanted inside cochlear (i.e., the electric stimulation) and a traditional acoustics-based hearing aid in the ear canal (i.e., the acoustic stimulation). Since the electric stimulation component is in vitro and the acoustic stimulation component is in vitro, these devices not only pose a challenging task for surgeon to implant but also inherit disadvantages of traditional hearing aids (e.g., occlusion). To realize combined electric and acoustic stimulations that are totally implantable inside the inner ear, the author's research team has been developing a novel intra-cochlear lead-zirconate-titanate (PZT) micro-

actuator to generate acoustic wave directly in the inner ear. Current design of the intra-cochlear micro-actuator is a square PZT diaphragm anchored at all four edges forming a tiny speaker. The purpose of this dissertation is to address three major challenges encountered while developing next-generation micro-actuators. They are size reduction, reliability and lead safety.

For size reduction, a partially released diaphragm structure is proposed in the dissertation. As the previous fully anchored diaphragm scales down in size, its deflection is substantially reduced, and the micro-actuator becomes ineffective. To increase actuation strength, two opposite diaphragm edges are released to enhance the flexibility of the diaphragm. A PZT intra-cochlear micro-actuator probe with three partially released diaphragms at the tip of a cantilever is also fabricated by through etching two slots on each diaphragm. To enable the open slots, new fabrication procedures (e.g., treatment of cat ears, annealing of bottom electrodes to remove electrode non-uniformity, etching of PZT and double-side etching to form open slots) are developed and discussed in detail in the dissertation. After the intra-cochlear PZT micro-actuator probe is fabricated, its frequency response function is measured experimentally and predicted via a finite element analysis (FEA). Both measurements and FEA predictions indicate that the sensitivity is dominated by the diaphragm deflection, while the first natural frequency is dominated by the cantilever structure. Furthermore, parametric studies indicate that precise control of the thickness of unetched silicon layer and elimination of residual silicon are critical to achieve designed micro-actuator performance,

For reliability, three series of tests are performed to investigate possible failure mechanisms. They are in-air tests, soaking tests, and in-fluid driving tests. The first two tests specifically focus on structural failure and electrical failure, respectively, while the third test

investigates their combined effects. Test results indicate that the electrical failure usually occurs prior to the structural failure. Moreover, the electrical failure can be detected by monitoring parallel resistance extracted from electrical impedance measurements. When a sudden and significant drop in the parallel impedance occurs, it implies that the surrounding fluid has infiltrated the encapsulation layer (parylene), resulting in electrical failure. As a result, the parallel resistance can be utilized as an indicator to monitor integrity of the intra-cochlear micro-actuator, especially when it is placed inside the inner ear. On the contrary, the structural failure manifests itself in sudden reduction of frequency response functions. As a result, the structural failure is most likely caused by delamination of the top electrodes from the PZT diaphragm. Finally, methods to improve the encapsulation layer and reliability are proposed.

For lead leaching, the possibility of replacing PZT with a lead-free piezoelectric material, especially the biocompatible polymer PVDF, is first explored. An FEA is conducted to assess the feasibility of using PVDF as an alternative material for intra-cochlear micro-actuators. The FEA results indicate that PVDF cannot effectively drive the intra-cochlear micro-actuators in fluid with large enough response due to its small piezoelectric constants. Next, the amount of lead that could possibly be leached from a PZT micro-actuator encapsulated by parylene is investigated. A series of long-term tests are performed by driving PZT micro-actuators in artificial perilymph to complete failure. Then samples from the artificial perilymph are collected, and the leached lead is measured via inductive coupled plasma mass spectrometry (ICP-MS). The test results confirm a concentration of 51ng/mL in the worst-case scenario, while the lead advisory level in blood published by the Center of Disease Control is not to exceed 100 ng/mL.

Keywords: PZT, thin film, cochlear implant, partially released, reliability, lead leaching

TABLE OF CONTENTS

List of Figures iv

List of Tables vii

Chapter 1. Introduction 1

1.1 PZT Diaphragm Structured Micro-Actuators 3

1.2 First-Generation PZT Micro-Actuators 5

1.3 Problems and Challenges 6

1.3.1 Challenge 1: Size reduction 7

1.3.2 Challenge 2: Reliability 9

1.3.3 Challenge 3: Lead safety 10

1.4 Thesis Outline 11

Chapter 2. Size Reductin And Development Of the 2nd Generation PZT Micro-Actautor 13

2.1 Design 13

2.1.1 Parameter assignment 14

2.1.2 The full and proportional 1/2 model 16

2.1.3 Cantilever model vs. partially released model 19

2.1.4 Acoustic analysis of the partially released model 22

2.1.5 Challenges of the partially released design 27

2.2 Fabrication 28

2.2.1 Brief fabrication flow 29

2.2.2 Pre-fabrication designs 31

2.2.3 Patterning of bottom electrode and elimination of "cat ears" 36

2.2.4 Annealing of bottom electrode 40

2.2.5 Patterning of PZT 44

2.2.6 Fabrication of partially released diaphragm by double side etching 47

2.2.7 The fabricated 2-G probe 48

2.3 Measurements and Discussions 50

2.3.1 Experimental setup 50

2.3.2 The frequency response function 52

2.3.3 Identification of the first natural frequency 52

2.3.4 Identification of the low frequency FRF 55

2.3.5 Interpretation of the static gain 56

2.3.6 Further discussions 59

2.4 Parametric Study and Optimization 60

2.4.1 Size of the diaphragm 60

2.4.2 Thickness of the unetched silicon layer 61

2.4.3 Width of the open slots 64

2.4.4 Size of the top electrodes 68

2.4.5 The optimized model 69

Chapter 3. Study of Reliability 71

3.1 Setup of Reliability Tests 72

3.1.1 Sample setup 72

3.1.2 Experimental setup 73

3.1.3 Electrical model setup 74

3.2 In-Air Reliability Tests 79
3.3 Soaking Test in Artificial Perilymph 81
3.3.1 Stage-1: Effective encapsulation 83
3.3.2 Stage-2: Encapsulation failure 84
3.3.3 Stage-3: Massive electrical leakage 86
3.4 Long-term Driving Test in Artificial Perilymph 87
3.5 The Failure Model 91
3.6 Potential Improvements 93
Chapter 4. Study of Lead Safety 95
4.1 Alternative Piezoelectric Materials 95
4.1.1 Double-layer beam model 96
4.1.2 Fully anchored diaphragm model 99
4.1.3 Tube model 100
4.2 Study of Lead Leaching 103
Chapter 5. Conclusions and Future Works 107
5.1 Conclusions 107
5.2 Future Works 109
Bibliography 111
Appendix A 115

LIST OF FIGURES

Figure 1-1: Hybrid implant with an intracochlear acoustic actuator 2
Figure 1-2: Front side and backside of the 1st generation PZT micro-actuator 6
Figure 2-1: Finite element model of the full-size fully anchored actuator 17
Figure 2-2: Finite element model of the proportional 1/2 model..................................... 19
Figure 2-3: Potential actuator designs.. 20
Figure 2-4: Finite element model of the partially released actuator 22
Figure 2-5: The finite element acoustic model 25
Figure 2-6: FE analysis on 1st mode shape, static gain and acoustic pressure field at 1kHz for both the open slot model and the isolated model.................................. 26
Figure 2-7: Fabrication flow of PZT micro-actuator with partially released diaphragm 30
Figure 2-8: Actuator layout designs.. 32
Figure 2-9: The mask design of the 2-G probe at the tip portion 34
Figure 2-10: The alignment mark designs 35
Figure 2-11: Difference in positive and negative photo-resists in patterning by lift-off.. 37
Figure 2-12: The existence and elimination of the “cat ear” 39
Figure 2-13: The bottom electrode annealing 43
Figure 2-14: The PZT layer fabrication and PZT shreds processing............................... 45
Figure 2-15. Optical microscopic photos of the PZT under cut at the patterning boundaries 46
Figure 2-16: The front side and backside etching pattern design for the 2-G probes....... 48
Figure 2-17: The functioning tip of the fabricated 2-G PZT micro-actuator,................... 49
Figure 2-18: Actuator fixture for frequency response function measurements 51
Figure 2-19: The experimental setup for frequency response function measurement...... 51
Figure 2-20: Frequency response function of the 2-G probe... 52

Figure 2-21: FRF and finite element modal analysis on a 2-G probe, before and after excessive epoxy is applied ... 54
Figure 2-22. Frequency response function measured at different positions of the diaphragm ... 56
Figure 2-23. Bask side view of the probe tip after DRIE, showing two diaphragms ... 58
Figure 2-24. Finite element model of the partially released actuator with modified residual silicon and unetched silicon layer ... 59
Figure 2-25. Diaphragm static gain with respect to the unetched silicon layer thickness ... 62
Figure 2-26. The combination of square layout and radial layout ... 64
Figure 2-27. The schematic illustration of the backside diaphragm with residual silicon ... 66
Figure 2-28: Parametric study of the diaphragm static gain with respect to diaphragm total length and open slot width ... 67
Figure 2-29: Parametric study of the static gain with respect to the length of electrode .. 69
Figure 2-30: The optimized model of partially released diaphragm actuator ... 70
Figure 3-1: Sample setup for reliability tests in artificial perilymph ... 73
Figure 3-2. The electrical model for reliability test ... 78
Figure 3-3: The mechanical behavior of the diaphragm driving in air ... 80
Figure 3-4: The static gain as a function of time for the PZT diaphragm soaked in artificial perilymph without driving ... 82
Figure 3-5: The parallel resistance Rp (solid lines) and the heredity coefficient α (dashed lines) of the PZT diaphragm as a function of time, measured by either center top / bottom electrode pair (in blue color) or outer top / bottom electrode pair (in red color) ... 83
Figure 3-6: Impedance magnitude and extracted parallel resistance Rp of a bare actuator soaked in artificial perilymph, compared with the actuator diaphragm in stage-2 of the soaking test ... 86
Figure 3-7: The static gain as a function of time for the PZT diaphragm driven in artificial perilymph by a 1V voltage at 10 kHz ... 89

Figure 3-8: The parallel resistance Rp (solid lines) of the PZT diaphragm as a function of time, measured by either center top / bottom electrode pair (in blue color) or outer top / bottom electrode pair (in red color) 90
Figure 3-9: Proposed failure mechanism of the PZT diaphragm..................................... 93
Figure 4-1: FE model of a piezoelectric cantilever beam adopting a double layer structure.. 98
Figure 4-2: FE model of a piezoelectric micro-actuator adopting fully anchored structure.. 100
Figure 4-3: FE model of a piezoelectric actuator adopting tube structure...................... 102

LIST OF TABLES

Table 2-1. Material properties of PZT 15
Table 2-2. Material properties of other materials 15
Table 2-3. The thickness parameters for the first generation PZT micro actuator 15
Table 3-1. Extracted electrical parameters before and after reliability test in air 81
Table 4-1. Material properties of PVDF 97
Table 4-2. Results of the lead leaching tests 105

ACKNOWLEDGEMENTS

I wish to express sincere appreciation to my home department, Mechanical Engineering, for their long-term support, and especially to my academic advisors, Professor I.Y. Shen and Professor G.Z. Cao, for their knowledge, patience, guidance, and inspiration.

I also would like to thank my thesis committee members, Professor Junlan Wang, Professor Jae-Hyun Chung, and Professor Robert B. Darling (GSR), for their generous help and valuable instructions.

Meanwhile, I want to thank all my lab mates. They are Weiwei Xu, Wei-Che Tai, Robert B. Manson, Mark Jankauski, Ya-Fang Chen, Sergiy M. Taylakov and Samantha Hoang. With absence of their endless support, my project would not move forward smoothly.

A very special thank is given to my wife, Ling Sun, and my two lovely kids, Elvin Liu and Nathan Liu, for their understanding, support and devotion.

At last, I want to express deep appreciation to all my friends, who unselfishly share their life experience and happiness with me.

Chapter 1. INTRODUCTION

Hearing loss is the total or partial inability to hear or recognize sound. Sensorineural hearing loss, a special disability of such type, is commonly found among old people and people working in noisy environments. It is caused by dysfunction or loss of cochlear hair cells, which do not regenerate. Therefore, the disability is permanent and special hearing devices are needed for patients to rehabilitate their hearings. Traditional hearing devices include hearing aids and cochlear implants. A hearing aid is an in vitro device that generates acoustic signals. It is placed in an ear canal to amplify incoming sound, providing enhanced stimulation to cochlear hair cells. It is primarily designed for patients with minor hearing loss. For people with profound hearing loss, cochlear implants are recommended. The core of a cochlear implant is an electrode array that directly stimulates the hearing nerve bypassing the hair cells. It is an in vivo device that requires implantation through surgery.

Patients with moderate hearing loss, however, belong to neither of these two groups. On one hand, their hair cells are partially damaged that mechanical stimulations (via hearing aids) can no longer provide effective rehabilitation of high-frequency hearing. On the other hand, they are not qualified to receive cochlear implants because part of their hair cells still preserve certain functionalities. Placement of a cochlear implant could damage those healthy hair cells and therefore the residual hearing.

Recent studies show that a combined electric-acoustic stimulation (EAS) could provide a solution to people with moderate hearing loss. An EAS typically consists of a mechanical acoustic component and a shortened electrode array. The mechanical component generates acoustic waves that stimulates the functional hair cells like a traditional hearing aid, while the

shortened electrode array stimulates the high-frequency auditory nerves like a cochlear implant. Such rehabilitation strategy preserves the healthy hair cells because the electrode array is shortened. Furthermore, it is proved that EAS can significantly enhance speech recognition even in environments with considerable background noise. [1] [2] [3] [4] [5] [6] [7].

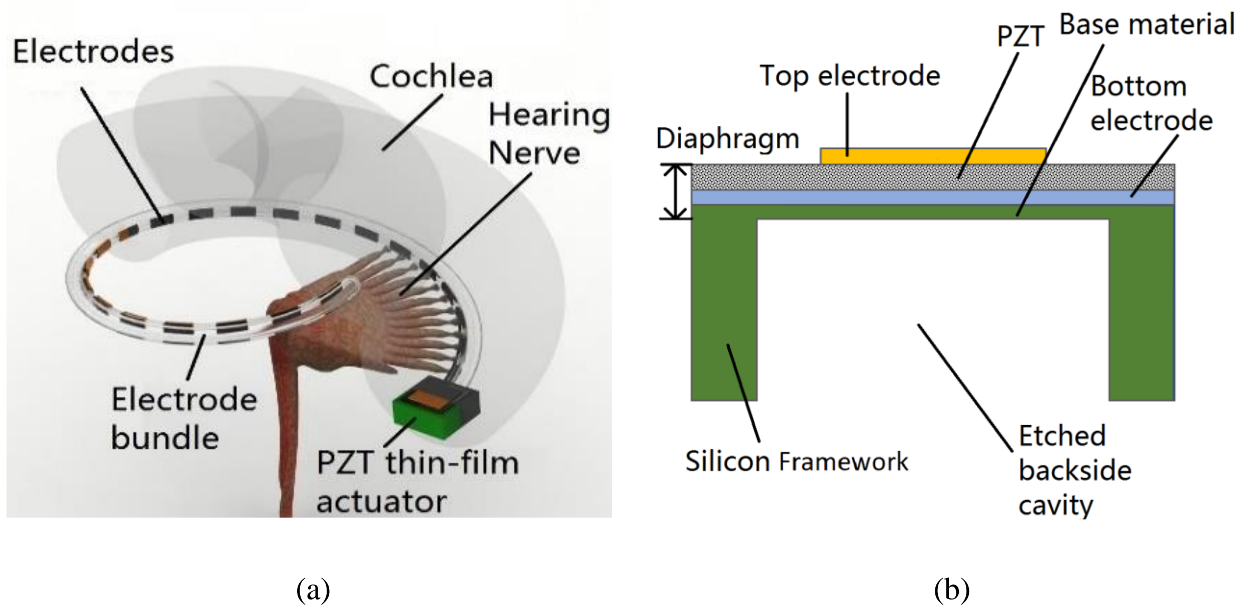

(a) (b)

Figure 1-1: Hybrid implant with an intracochlear acoustic actuator
(a) the hybrid implant in cochlea; (b) Cross sectional view of the actuator

Nevertheless, current EAS devices involves cooperation between an in vitro device (i.e., a conventional hearing aid) and an in vivo device (i.e., a cochlear implant with a shortened electrode). This setup has two major drawbacks. First, the separated devices can induce coordination problems that require the patients to adjust the hearing devices continuously. Second, the hearing aid receiver may block the ear canal (i.e., occlusive effects), which may cause lower sound quality, discomfort and infection.

Motivated by the needs above, Professor Shen's research team has proposed and studied a hybrid cochlear implant as shown in Figure 1-1(a) for the last decade. Unlike the conventional EAS devices, the hybrid device provides both acoustic and electrical stimulations inside the cochlea. The electrical stimulation remains from a shortened electrode array, while the acoustic stimulation is produced via an intra-cochlear acoustic micro-actuator. The micro-actuator is placed in scala tympani, serving as a tiny speaker in human inner ear. Such configuration provides a potential solution to resolve the problems of conventional EAS devices explained above.

1.1 PZT Diaphragm Structured Micro-Actuators

There are two requirements for the proposed intra-cochlear acoustic micro-actuators. First, the actuator must be small enough (less than 1 mm in width and in length) to fit into the narrow space in cochlea before the first turn. Second, acoustic waves generated by the intra-cochlear micro-actuators must reach specific pressure levels to be detected by hair cells. One common solution to meet both requirements is to use piezoelectric materials in the form of thin films to drive the intra-cochlear micro-actuators. Piezoelectric materials are desirable for their large bandwidth and fast response. For acoustic wave generation, a diaphragm structure is often used to increase displacement of the micro-actuators.

Piezoelectric thin films have seen wide applications as sensors and actuators including dynamic micro-pumps [8], atomic force microscopes [9, 10, 11], hard disk drives [12, 13], ultrasound transducers [14, 15], bio sensors [16, 17] and actuators [18]. Especially, diaphragm structured designs are seen in various applications such as microphones [19, 20, 21, 22], pressure sensors [23, 24] and acoustic actuators [25, 26, 27]. Figure 1-1(b) shows the cross-sectional view

of a typical piezoelectric diaphragm design. The key component is a piezoelectric thin film, sandwiched by a top electrode and a bottom electrode. The thin film structure is usually fully anchored to bulk materials such as silicon. After poling (applying a higher DC voltage for a specific amount of time), an electrical potential difference between the top and bottom electrode will induce an in-plane strain in the piezoelectric thin film. When the piezoelectric layer is off the neutral plane, a bending moment is produced accordingly, thus deforming the diaphragm in the out-of-plane direction.

The performance of a piezoelectric diaphragm as an actuator is typically evaluated by its static gain and bandwidth. The static gain is the displacement produced by unit voltage applied to the electrodes (e.g., nm/V) when the driving frequency is far below the first natural frequency. The bandwidth is the frequency range below the first natural frequency, in which the frequency response function (FRF) roughly remains a constant. The constant is referred to as "static gain".

In addition to the above thin film structures (i.e., one piezoelectric layer and two electrode layers), a layer of base material usually is present underneath the bottom electrode. This base material layer has the following functions. First, in real fabrication, thin films are usually formed by wet or dry etching of the bulk material from the backside. The thin base layer appears in the fabrication process as an etch stop, protecting the thin diaphragm above. Second, the base material is often very rigid and adheres well to the anchoring structure, thus providing a reliable support to carry the thin film structures. Third, the thickness of the base material layer can be controlled to produce desirable overall stiffness and distance off the neutral plane to obtain designed static gain and bandwidth.

In the intra-cochlear micro-actuator applications, we choose lead-zirconate-titanate (PZT) as the piezoelectric material. PZT is known for its large piezoelectric constants and high rigidity

(e.g. $d_{33} = 289$ pC/N and $C_{11} = 139$ GPa for bulk PZT-4). The large piezoelectric constants are crucial to in producing a large static gain, while the high rigidity ensures wide enough bandwidth. Such properties make PZT an attractive material for micro-actuators. Since the actuators will be fabricated via semiconductor processes, silicon is chosen to anchor the diaphragm because its processing methods are highly standardized.

1.2 First-Generation PZT Micro-Actuators

Professor Shen's research team has previously developed a PZT micro-actuator for intra-cochlear applications [25] [28]. Figure 1-2 shows the front and back view of the micro-actuator. It adopts a fully anchored diaphragm structure placed at the tip of a silicon beam for easy operations. The diaphragm takes the same configuration as in Figure 1-1. Namely, the base material is a thin layer of silicon oxide and silicon nitride. The bottom electrode consists of 100 nm platinum and 50 nm titanium. The top electrode consists of 500 nm gold and 25 nm chromium. The PZT is fabricated via sol gel methods, producing a thin film of approximately 1 μm in thickness. The total size of the diaphragm is 800 μm by 800 μm, leaving 100 μm thick silicon as the diaphragm anchors. Moreover, the actuator adopts a dual electrode design including a center electrode and an outer electrode, separated by a gap of 30 μm.

The diaphragm will deform when voltage is applied between the bottom electrode and either of the two top electrodes. To achieve maximum deflection, one can apply out of phase voltages to the center and outer electrodes while the bottom electrode is grounded [26]. Since the actuator is designed to operate in perilymph [29], it is coated with a thin layer of parylene (approximately 25 nm in thickness, refer to Figure.13 of [25]). The entire device, including the actuator and the holding silicon beam, is referred to as "1-G probe" for the rest of the dissertation.

The 1-G probe has been fully characterized. The static gain is typically 10 – 50 nm/V in air and 20 – 70 nm/V in fluid. Its first natural frequency is over 70 kHz in air and over 20 kHz in fluid, leaving a steady and flat region in its frequency response function (FRF) throughout the audible frequencies. Also, feasibility of the 1-G probe has been successfully demonstrated in acute animal tests via a guinea pig model. Auditory brainstem response stimulated by the micro-actuator is comparable to the input signal [30].

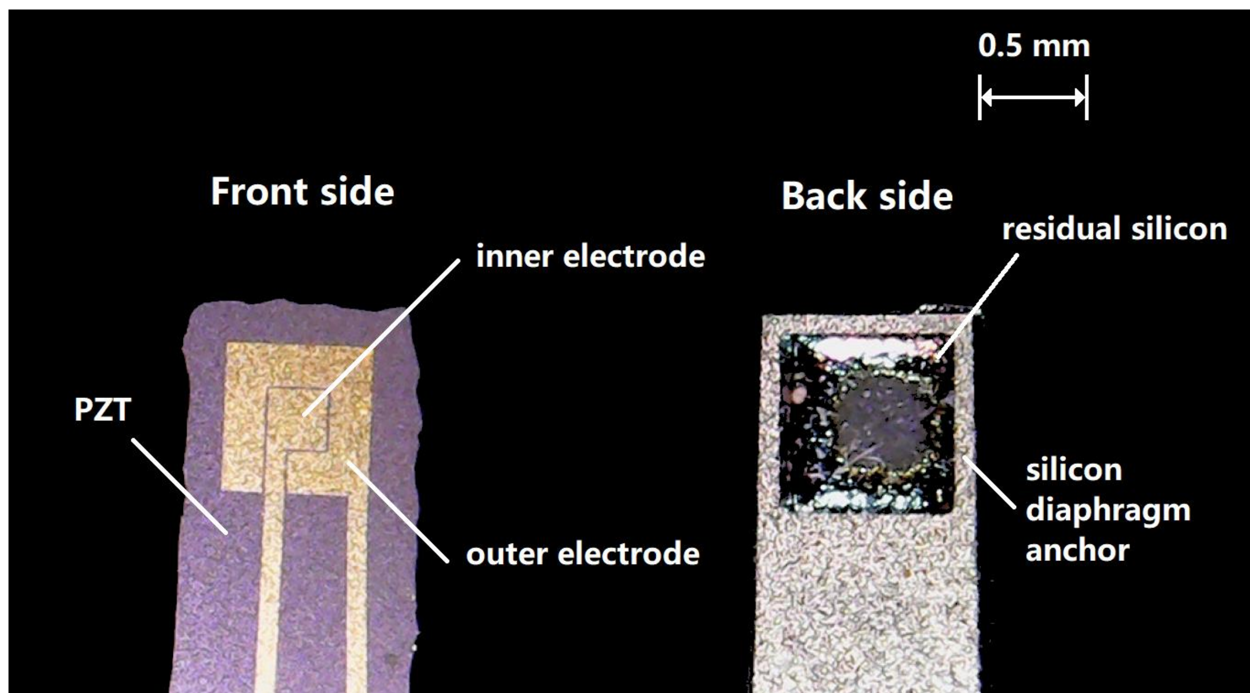

Figure 1-2: Front side and backside of the 1st generation PZT micro-actuator

1.3 Problems and Challenges

Although the feasibility of the 1-G probe and the fully anchored PZT diaphragm has been demonstrated, there are major challenges to use the 1-G probe for future chronic animal tests.

The major challenges include size reduction, reliability, and lead leaching. They are explained in detail as follows.

1.3.1 Challenge 1: Size reduction

The first challenge is the size of the micro-actuator. Previous animal tests showed that the probe can barely enter the basal turns of cochlea and could cause damage during the surgical implantation. It is also difficult to adjust the orientations of the probe due to its large size. Therefore, it is suggested by the surgeon that the total width of the actuator should not exceed 700 μm.

The size reduction, however, is not a trivial task if the same actuator performance is needed. First of all, dimensions in thickness direction is hard to change. For example, a thinner PZT layer may cause short circuit and a thinner electrode may delaminate from the substrate or PZT. According to the classical plate theory, maximal out-of-plane deflection of a fully anchored rectangular plate is

$$w_{max} = c_1 \frac{p \cdot min(L_x, L_y)^4}{Et^3} \quad \text{Eqn. 1}$$

where p is a uniform pressure applied on the plate in z-direction (i.e., out-of-plane direction), L_x and L_y are the length and width of the plate, E is the Young's modulus, t is the thickness of the plate, and c_1 is a constant coefficient. For square plates (i.e., $L_x = L_y$), $c_1 = 0.0138$. As the in-plane dimensions reduce, the out-of-plane deflection w_{max} drops significantly in the form of fourth order. Furthermore, the area of electrodes will become smaller accordingly, producing less actuation in the PZT layer and further reducing the out-of-plane deflection.

Another problem that causes the static gain to drop is residual silicon. As shown in previously literature (refer to Figure 3 & 4 of [27]), residual silicon is formed during the fabrication process in the backside deep reactive ion etching (DRIE) step. In particular, the backside etching is non-uniform because of the complicated topology of the etched surface. Since the etch depth is as thick as the entire wafer substrate, such non-uniformity may accumulate leaving a “ring” of residual silicon around the four sides of the etched cavity. The size of the residual silicon is sensitive to etching parameters, and it varies around 60 μm into the diaphragm. The cross section of the residual silicon takes a triangular shape with the largest thickness appearing near the diaphragm boundaries at the anchor, typically 20 – 50 μm in thickness.

The existence of the residual silicon is not all that disadvantageous to the micro-actuators. For example, the presence of residual silicon improves diaphragm integrity. Since the cross section takes a triangular shape, the residual silicon serves as a transitional structure between the diaphragm and the anchor, thus reducing stress concentration at the diaphragm boundaries.

As the micro-actuator is reduced in size, the disadvantages from residual silicon outweighs the advantages. Since silicon is very rigid and average thickness of the residual silicon is much larger than that of the diaphragm (i.e., over 10 μm vs. 2 μm), one can literally consider the diaphragm occupied by the residual silicon as ineffective areas because it barely deforms when voltage is applied. As the micro-actuator reduces in size, the effective diaphragm area (i.e., area not occupied by the residual silicon) becomes significantly smaller compared to the total diaphragm area. As a result, the actual out-of-plane deflection is much smaller than the theoretical prediction. To make the situation even worse, it is found in fabrication process that the residual silicon may conversely become larger as one reduces the diaphragm dimensions. The

effects of such phenomenon are shown in the later chapter (section 2.1) through a finite element (FE) model analysis. The results indicate significant reduction in the diaphragm deflection.

In short, the actuator diaphragm will no longer have large enough out-of-plane deflection to effectively drive the perilymph fluid if one simply reduces the in-plane dimension proportionally. Therefore, the diaphragm must be re-designed in order to reduce the size without compromising too much performance (i.e., out-of-plane deflection and bandwidth).

1.3.2 Challenge 2: Reliability

The second challenge is the reliability and integrity of the micro-actuator, especially in long-term conditions (e.g., chronic animal tests). Previous characterizations are mainly for short-term performance, as one can typically drive the micro-actuator and measure its mechanical properties (i.e., FRF) within 15 minutes. Long-term properties, such as service life and failure mechanism, of the micro-actuators remain largely unknown. Although we have performed a short-term integrity test (for about 50 hours, refer to [25]) by monitoring the FRF behavior over time, such test has a major drawback, that is, the FRF behavior may not be available in other test conditions. For example, the designed service condition of the micro-actuators is in human cochlea, which is a small space filled with perilymph (a conductive salty fluid). The fluid environment may cause short circuit of the micro-actuators after long-term use. Since the micro-actuators are implanted inside cochlea, FRF measurements are not available to detect the short circuit and micro-actuator failure. Therefore, a reliable method is required for the in-time monitoring of the micro-actuator status.

1.3.3 Challenge 3: Lead safety

The third challenge is a theoretical concern of lead leaching. Although PZT is a stable solid insoluble to the surrounding fluid such as perilymph, there is still possibility that lead may slowly leach into the fluid in long term service, either in forms of ions or small particles. There are two potential approaches to the lead leaching problem.

The first approach is to replace PZT with another piezoelectric material, such as biocompatible piezoelectric polymer PVDF. Apparently, this approach solves the lead leaching issue since no lead exists in the device. However, it is not trivial to realize. First, the feasibility of replacing material must be demonstrated (e.g., by finite element simulations). The material should have high stiffness and large piezoelectric constants to ensure same level performance (i.e., static gain and bandwidth). Second, a new fabrication process must be developed to integrate the replacing material into the micro-actuator application.

The second approach is to deposit an encapsulation material to properly seal the lead from leaching into fluid. This approach has already been performed, since the parylene layer encapsulating the 1-G probe can also service to prevent lead from leaching into the surrounding perilymph. However, since PZT is still utilized, three unknowns must be solved. First, the effectiveness of parylene encapsulation must be determined. Second, the level of lead leaching in case the parylene encapsulation is compromised must be evaluated. Third, again, a method to monitor the integrity of parylene encapsulation must be developed to detect occurrence of encapsulation failure in time.

1.4 THESIS OUTLINE

This dissertation is based on an intra-cochlear PZT micro-actuator previously developed by Prof. Shen's research team, and solves three major problems before the chronic animal test. They are the size reduction of the micro-actuator, the reliability in long-term driving, and the issue of lead safety.

For the study of size reduction, it is first demonstrated by FE analysis that a proportional size reduction using fully anchored boundary condition would significantly reduce the static gain of the diaphragm. Then a partially released diaphragm is proposed by through etching two open slots on the sides in lateral direction. The partially released design is proved by FE analysis to have large enough static gain and bandwidth. Acoustic analysis is also done to investigate the influence of the open slots to the acoustic pressure field, as well as the added mass effect. The fabrication of such device, however, is not a trivial task. Therefore, the fabrication of the partially released actuator is shown in detail. The newly fabricated actuator is then characterized by measuring its frequency response function. The small static gain and the abnormally low first natural frequency is discussed and demonstrated by experimental methods. Finally, a series of parametric studies are performed to determine optimal geometrical parameters to maximize the performance.

For the study of reliability, long-term tests are performed using the first generation PZT actuators (i.e., the 1-G probes with fully anchored diaphragms). The test setup is first shown. Especially, the sample setup for long-term test should avoid issues such as evaporation and contamination. Three long-term tests are then performed. They are the in-air test, the soaking test and the long-term driving test. To interpret the results, an electrical model is established to extract the parallel resistance of the diaphragm. The results show three stages of relatively stable

performance. The major failure mechanism is electrical failure due to infiltration of the parylene layer. Finally, potential solutions to enhance the effectiveness of encapsulation are proposed.

For the study of lead safety, we first investigate the possibility of replacing PZT with a lead-free piezoelectric material. Potential candidates include common piezoelectric ceramics such as ZnO and AlN, as well as PVDF, a piezoelectric bio-compatible polymer. Especially, the feasibility of PVDF is researched in detail via finite element simulations. The FEA results indicate that other piezoelectric materials including PVDF typically acquire too small piezoelectric constants to effectively drive the diaphragm of the intra-cochlear micro-actuator. Next, we evaluate the level of lead leaching in to following way. The PZT micro-actuators (i.e., the 1-G probes) are driving continuously in artificial perilymph until complete failure. The artificial perilymph is then collected, and the leached lead concentration is measured via inductive coupled plasma mass spectrometry (ICP-MS). The results confirm a concentration of 51 ng/mL in the worst-case scenario, while the lead advisory level in blood published by the Center of Disease Control is not to exceed 100 ng/mL.

Chapter 2. SIZE REDUCTIN AND DEVELOPMENT OF THE 2ND GENERATION PZT MICRO-ACTAUTOR

This chapter shows the development of the 2nd generation PZT micro-actuator of which the diaphragm is successfully reduced without scarifying performance significantly. The partially released design is first introduced, which is demonstrated by finite element simulations. Then the fabrication of actuator adopting such design is shown in detail and the challenges during fabrication are explained. After fabrication, frequency response function of the actuator probe is measured. The abnormally small first natural frequency and static gain are interpreted and justified using both FE analysis and experiments. Finally, a series of parametric studies are carried, and an optimized model is proposed as guidelines of future fabrications.

2.1 DESIGN

Static gain and bandwidth are the two major criteria in the re-design of PZT diaphragm. The static gain, which refers to the out-of-plane deflection of the PZT diaphragm driven in low frequencies divided by the applied voltage (unit: nm/V), is closely related to intensity of the generated acoustic wave. The bandwidth refers to a relatively flat and steady region in the frequency response function. For PZT diaphragms, it is largely determined by the 1st natural frequency.

To quantitatively evaluate these two parameters, we refer to finite element (FE) model analysis. A brief outline is as follows, followed by detailed discussions. An FE model of the 1-G actuator (refer to as “full model” for the rest of the dissertation) is first established and simulated. In order to investigate the effects of direct (and proportional) size reduction, another FE model

that is 1/2 in all diaphragm in-plane dimensions (refer to as "proportional 1/2 model" for the rest of the dissertation) is then presented and evaluated. The simulation results show that the static gain is significantly reduced for the proportional 1/2 model. To enhance the performance, two potential design candidates are presented. They are cantilever beam model and partially released model. Again, FE analysis is utilized to evaluate these two designs. It is later shown that the partially released design is successful in reducing the diaphragm stiffness and enhancing the static gain. Finally, acoustic behaviors including pressure field change and added mass effect are evaluated, especially for the partially released design.

2.1.1 Parameter assignment

There are four sets of parameters kept unchanged throughout the simulations. The first set is piezoelectric properties, which are 5.43% of bulk PZT-4 [31]. The number 5.43% is based on previous research on the d_{33} estimations in [32]. Here, we roughly assume that all the other piezoelectric constants including d_{31} are reduced proportionally. The second set of parameters is basic material properties, such as density and elasticity. Especially, the properties of the PZT layer are assigned to be same as that of PZT-4, shown in Table 2-1. The other materials such as silicon and electrode metals are shown in Table 2-2. Here we just roughly estimate the material properties, especially the piezoelectric constants, because it is not a crucial condition for comparing performances of different designs, since the out-of-plane deflection will only change proportionally if a different set of piezoelectric constants is utilized. The third controlled parameter is the thickness of each layer. As is discussed above, the dimensions in thickness directions are kept unchanged throughout the simulations and are listed in Table 2-3. Finally, the boundary conditions and loading conditions are kept unchanged. For boundary conditions, the

actuator adopts “fully clamped” condition at the silicon anchor toward the probe side (refer to Figure 2-1). For loading conditions, the bottom electrode is grounded (i.e., voltage = 0V) and an electrical voltage of 1V is applied to the center top electrode. Here we choose not to drive the outer top electrode for simplicity.

Table 2-1. Material properties of PZT

Material property	Value
Density: ρ (kg/m^3)	7500
Compliance elasticity: [C](GPa)	$$\begin{bmatrix} 139.00 & 77.83 & 74.28 & 0 & 0 & 0 \\ 77.83 & 139.00 & 74.28 & 0 & 0 & 0 \\ 74.28 & 74.28 & 115.41 & 0 & 0 & 0 \\ 0 & 0 & 0 & 25.64 & 0 & 0 \\ 0 & 0 & 0 & 0 & 25.64 & 0 \\ 0 & 0 & 0 & 0 & 0 & 30.58 \end{bmatrix}$$
Piezo-electric constant: [d] (pC/N)	$$\begin{bmatrix} 0 & 0 & 0 & 0 & 26.933 & 0 \\ 0 & 0 & 0 & 26.933 & 0 & 0 \\ -6.679 & -6.679 & 15.693 & 0 & 0 & 0 \end{bmatrix}$$

Table 2-2. Material properties of other materials

Material	Density (kg/m^3)	Isotropic Elasticity (GPa)	Poisson's Ratio
Silicon	2330	202	0.33
Gold	19280	80	0.42
Platinum	21450	168	0.38

Table 2-3. The thickness parameters for the first generation PZT micro actuator

Parameters	Thickness (μm)
Passive silicon membrane	0.4
Bottom electrode	0.19
PZT thin film	1.13
Top electrode	0.5
Actuator total thickness	250

2.1.2 The full and proportional 1/2 model

The full model is established to simulate the case of 1-G probe. The total width of the actuator is 1000 μm, of which the diaphragm occupies an 800 μm × 800 μm square at the center, leaving 100 μm silicon anchor on each side. The finite element model is shown in Figure 2-1, with Figure 2-1 (a) and (b) showing the front side and backside views respectively. The residual silicon at the diaphragm boundaries is again modeled (Figure 2-1 (b)) as a ring-shaped incline of 60 μm in width, starting from 0.5 μm, increasing linearly in thickness till 20 μm. The inclined zone is followed by a flat zone of 15 μm in width. The total width of the residual silicon is therefore 75 μm into the diaphragm. The flat zone is modeled for model simplicity since residual silicon as thick as 20 μm barely moves in simulations. Figure 2-1 (c) shows the cross section of the diaphragm. Note that the layer configurations are the same as the in Figure 1-1 (b). Also note that the “diaphragm anchor (Si)” is in fact the projection from the side view and is therefore not part of the diaphragm. Again, the actuator adopts “fully clamped” boundary condition shown in Figure 2-1 (d).

When an electric voltage of 1V is applied across the top center and bottom electrodes, FE analysis (Figure 2-1 (e)) gives a static gain of 18.22 m/V. Modal analysis is also performed. The 1st natural frequency is 35.51 kHz, as shown in Figure 2-1 (f).

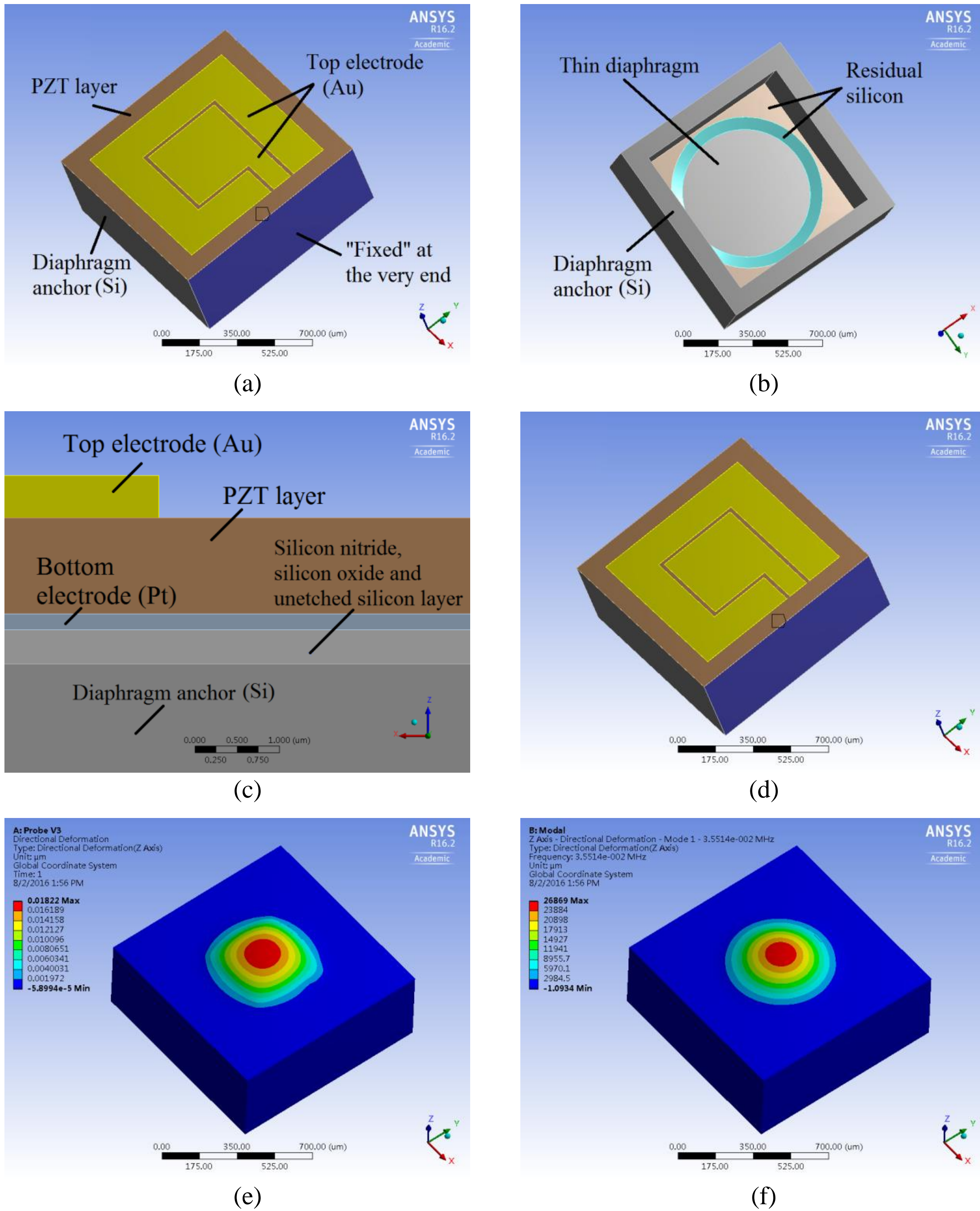

Figure 2-1: Finite element model of the full-size fully anchored actuator
(a) the front side view; (b) the backside view;
(c) the cross-sectional view; (d) the “fully clamped” boundary condition;
(e) static analysis, static gain = 18.22 nm/V;
(f) modal analysis, 1st natural frequency = 35.51 kHz

The full model is then scaled down by proportionally reducing 50% of the in-plane dimensions. One exception is the size of residual silicon, which is assumed to occupy same distance into the diaphragm as before. The front side and backside view of the proportional 1/2 model is shown in Figure 2-2(a) and (b). From Figure 2-2(b), one can easily see that the percentage of the diaphragm occupied by residual silicon is much larger compared with the full scale model (i.e., Figure 2-1(b)). Under the same boundary and loading conditions, FE static analysis shows an out-of-plane deflection of 3.39 nm/V (Figure 2-2(c)), only 18.22% of the full model. However, according to modal analysis, the first natural frequency is as high as 231.28 kHz (c.f. Figure 2-2), which is over 5 times larger than that of the full model. The extremely high natural frequency means a too stiff diaphragm. In order to enhance the static gain, the diaphragm should be re-designed to reduce the overall stiffness.

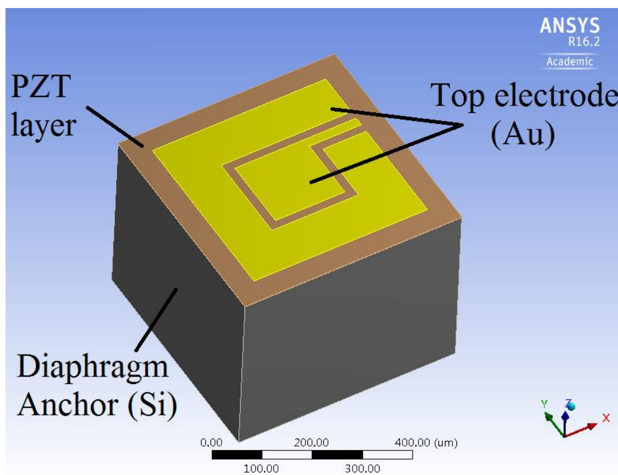

(a)

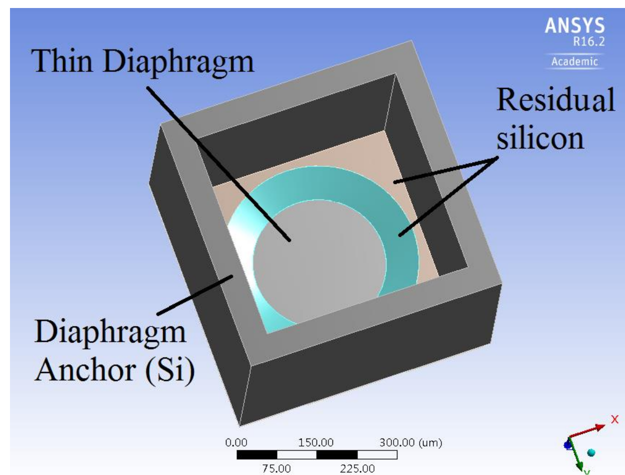

(b)

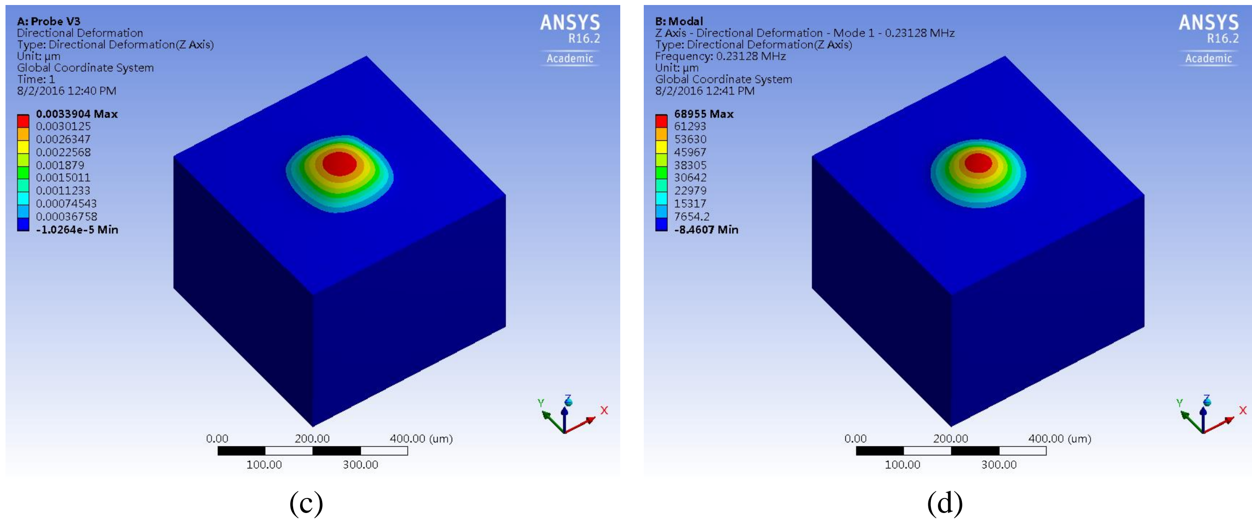

(c) (d)

Figure 2-2: Finite element model of the proportional 1/2 model
(a) the front side view; (b) the backside view;
(e) static analysis, static gain = 3.39 nm/V;
(f) modal analysis, 1st natural frequency = 231.28 kHz

2.1.3 Cantilever model vs. partially released model

Since boundary conditions can significantly affect the stiffness of a structure, the primary strategy for diaphragm re-design is to modify its boundary conditions. One obvious design would be a cantilever plate, by through etching three open slots on the sides of the fully anchored diaphragm (shown in Figure 2-3(a)). Theoretically speaking, by accepting such design, the stiffness may become much lower than a fully anchored diaphragm. However, the cantilever design has several drawbacks. One of them is wrapping. Namely, stress is accumulated during the fabrication process due to the vastly different layer treatments such as high temperature deposition and sintering. After the actuator is fabricated, this internal stress is not likely to be released, causing permanent bending and wrapping to the thin cantilever. The permanent wrapping is considered as a defect since it alters the diaphragm deflection and the direction of wave transmission. Even worse, the diaphragm wrapping conditions are totally unpredictable

since one lack control over the stress produced at each fabrication step. In addition to wrapping, a more important issue is liability. Ceramic materials such as PZT are in general very brittle, especially when fabricated into micro-scale cantilevers. The effect of wrapping discussed above may also cause failure to the PZT layer, such as cracking and delamination. Finally, even if one could successfully fabricate PZT micro-actuators with cantilever diaphragms, it is still extremely fragile from a structural point of view and is very likely to break during operations such as implant surgery or clinical applications.

An alternative design would be a partially released design. Instead of releasing three sides of the diaphragm, one can release only the two opposite sides in the lateral direction as shown in Figure 2-3(b). By adding another anchor to the diaphragm on the opposite side, the structure becomes much more reliable. The wrapping issue is also solved since both ends are now anchored. Although the overall stiffness of the diaphragm will not decrease as much as in the cantilever case, there is a small margin of adjustment over the stiffness, as one can choose to fabricate diaphragms of different lengths (i.e., in the longitudinal direction).

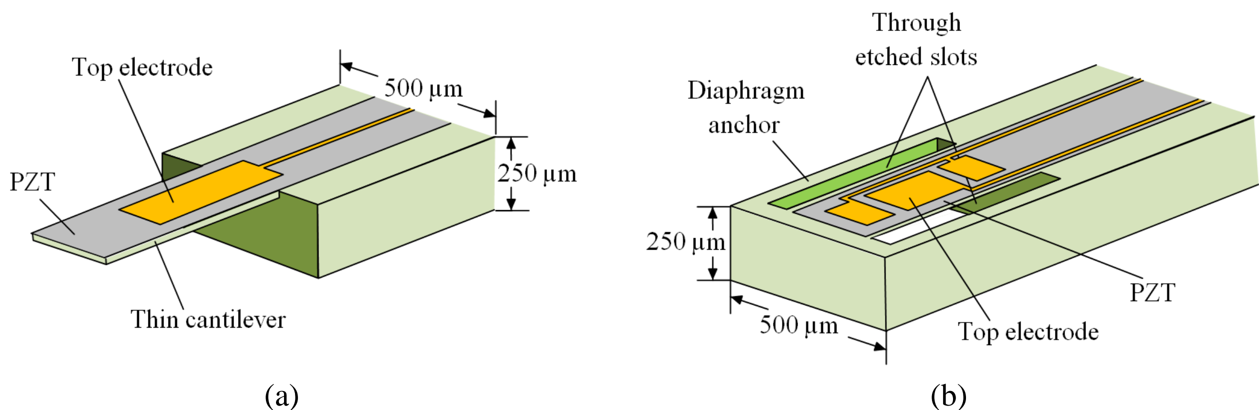

Figure 2-3: Potential actuator designs
(a) cantilever design; (b) partially released diaphragm design.

To demonstrate the above statements, again we refer to FE analysis. An FE model of PZT actuator with partially released diaphragm (referred to as “partially released model” for the rest of the dissertation) is established and shown in Figure 2-4 (a) & (b). The total width of the actuator is also 500 μm, same as the proportional 1/2 model, and the total length is 550 μm. Residual silicon still exists in the backside of the diaphragm and is modeled as the same size as in the proportional 1/2 model. However, since the open slots are formed by through etching, the residual silicon material underneath will be etched as well. This phenomenon is included in the FE model and is illustrated in Figure 2-4(b).

We utilize the same boundary condition (i.e., fully clamped) and apply voltages of 1V and 0V to the center top electrode and the bottom electrode respectively. As shown in Figure 2-4 (c) & (d), the static structural analysis shows an out-of-plane deflection of 12.62 nm/V, and the modal analysis gives the first natural frequency to be 86.64 kHz. The out-of-plane deflection is slightly smaller than that of the full model (18.22 nm/V) but is acceptably large and shows significant improvement over the proportional 1/2 model (3.39 nm/V). The bandwidth is also reasonably large at 86.64 kHz, much higher than 20 kHz.

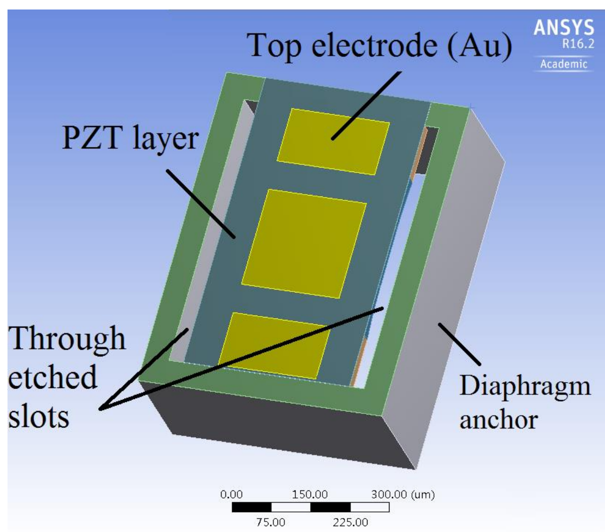

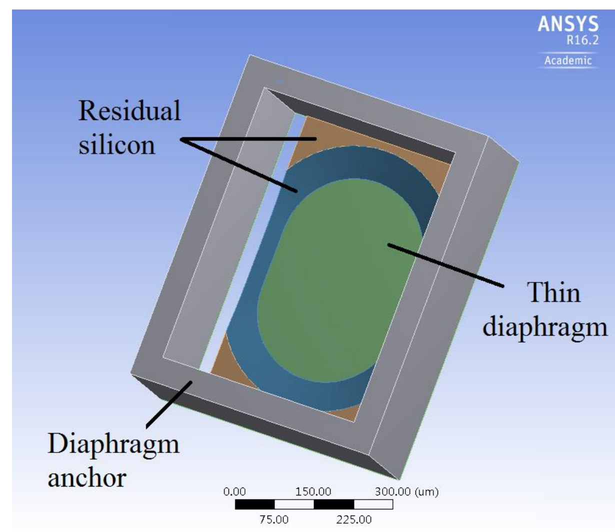

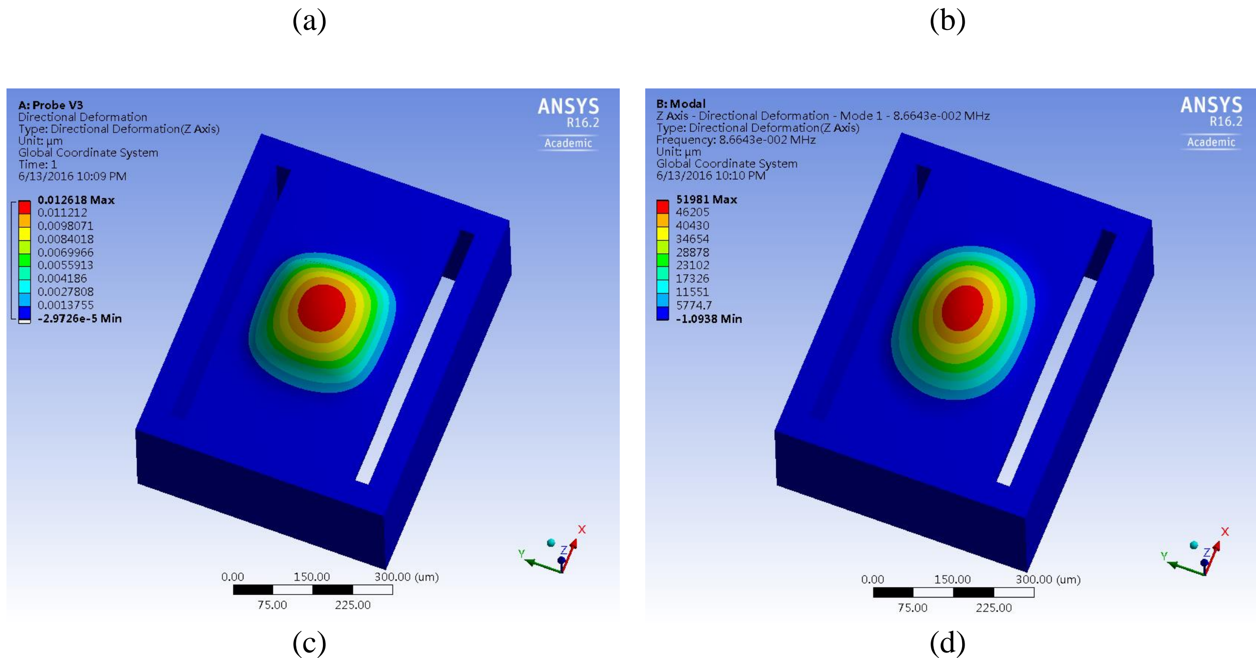

Figure 2-4: Finite element model of the partially released actuator
(a) the front side view; (b) the backside view;
(c) static analysis, static gain = 12.62 nm/V;
(d) modal analysis, 1st natural frequency = 86.64 kHz

2.1.4 Acoustic analysis of the partially released model

The FE models has demonstrated that the partially released design can significantly enlarge the static gain while keeping an ideal bandwidth. A large static gain, however, does not necessarily mean intensive acoustic pressure. Unlike fully anchored models, where there is no direct communication between the fluid at the two sides of the diaphragm, the existence of the open slots allows transmission of pressure waves and will therefore alter the acoustic pressure field. Moreover, because perilymph (or other kinds of fluid) has much higher density than air, when the actuator vibrates in such environment, there is added mass effect applied to the diaphragm, which may lower the 1st natural frequency, and therefore, the bandwidth. Especially,

when two slots are opened, the added mass effect may alter as well. To investigate the acoustic pressure and added mass effects, we again refer to finite element models as follows.

The purpose of the FE simulations is to investigate the influence of open slots to the acoustic pressure generated and the added mass effect. Therefore, two models are established for comparison. The first model is a PZT micro-actuator surrounded by acoustic materials simulating fluid environment. The PZT micro-actuator mostly follows the configurations as in the partially released model (c.f. Figure 2-4) except for three differences. First, we save calculation resources by utilizing a 1/4 model since the diaphragm is symmetric in both longitudinal and lateral directions. Second, the residual silicon is not modeled for simplicity. Third, the top electrode now spans the whole diaphragm in the lateral direction. Although such top electrode is infeasible to fabricate, it stands for the extreme condition that the diaphragm deflection near the slot area is maximized so that the pressure change near the open slot area can be easily observed. This model is referred to as "open slot model" for the rest of the dissertation.

The second model is established to serve as a compare model, for which two conditions must be met. First, the model should be very similar to the open slot model so that their mechanical properties such as static gains and 1st natural frequencies are very similar. Second, the diaphragm must be specially modeled so that it can isolate the acoustic pressure field on the two sides while still acquiring similar deformation profile as the open slot model. The above conditions can be satisfied by re-modeling the material in the open slot region (highlighted in Figure 2-5) as follows, while keeping all the other parameters unchanged.

For the open slot model, the material in the open slot region is assigned to be "acoustic body" since that space is filled with fluid in reality. For the compare model, it is modeled as "solid" instead, of which the Young's modulus is only 0.1 GPa, thus more than 3 orders of

magnitude smaller than the stiffness of the diaphragm, and the density is set to be only 1 kg/m^3. On one hand, the small stiffness and low density ensure the diaphragm to have same level static gain and first natural frequency, as well as very similar deformation profile. On the other hand, the "solid" material in the slot region can prevent acoustic pressure from transmitting to the other side of the diaphragm. We refer to this compare model as "isolated model" and the special material as "isolating material" for the rest of the dissertation.

Static and modal analysis are first performed on both models in air, using same boundary conditions as in Figure 2-4. The static gains and 1st natural frequencies are 37.14 nm/V, 18.78 kHz for the open slot model, and 38.68 nm/V, 18.85 kHz for the isolated model. The simulations suggest very close static gains and 1st natural frequencies. The corresponding deformation profiles of static analysis and the 1st vibration mode are shown in Figure 2-6 (a) and Figure 2-6 (c) for the open slot model, and in Figure 2-6 (b) and Figure 2-6 (d) for the isolated model, with the isolating material highlighted in red circle. On can see from the contour lines that the deformation profiles for both models are also very similar. Therefore, the in-air FEA validates our modeling of the isolating material.

For acoustic analysis, we are interested in two parameters, the pressure field at a typical driving frequency and the added mass effect (i.e., the 1st natural frequency drop when driving in fluid). In order to obtain the pressure field, we set up the boundary and loading conditions as follows. First, the actuators are again fully clamped at one end, while an electrical voltage of 1V is applied between the two electrodes. Here we choose to drive at 1 kHz. For the acoustic material, we assign the density to be 1000 kg/m^3, and the sound speed to be 1500 m/s (same as water). The pressure field contour plots are shown in Figure 2-6 (e) and (f) for the open slot model and the isolated model respectively. Notice that the solid parts (i.e., the actuator) is hidden

for easy observations (highlighted in white rectangles). One can immediately see from the two contour plots are the existence of open slots does change the pressure field significantly. This is especially true near the open slot regions. For the isolated model (c.f. Figure 2-6 (f)), since there is no fluid communication, the pressure is vastly different on two sides. When an open slot is created as in Figure 2-6 (e), the pressure evolves gradually via the slot. In addition to the pressure contour, we also observe an obvious decrease in acoustic pressure. For example, the maximum pressure obtained from the isolated model is 0.454 Pa, while the maximum pressure obtained from the open slot model is 0.230 Pa. The pressure drop is approximately 50% (i.e., $[(0.454 - 0.230)/0.454] \times 100\%$). From design point of view, although the diaphragm does become less effective in generating acoustic pressure by adopting a partially released design, the performance drop is still acceptably large, compared with the previous proportional 1/2 model.

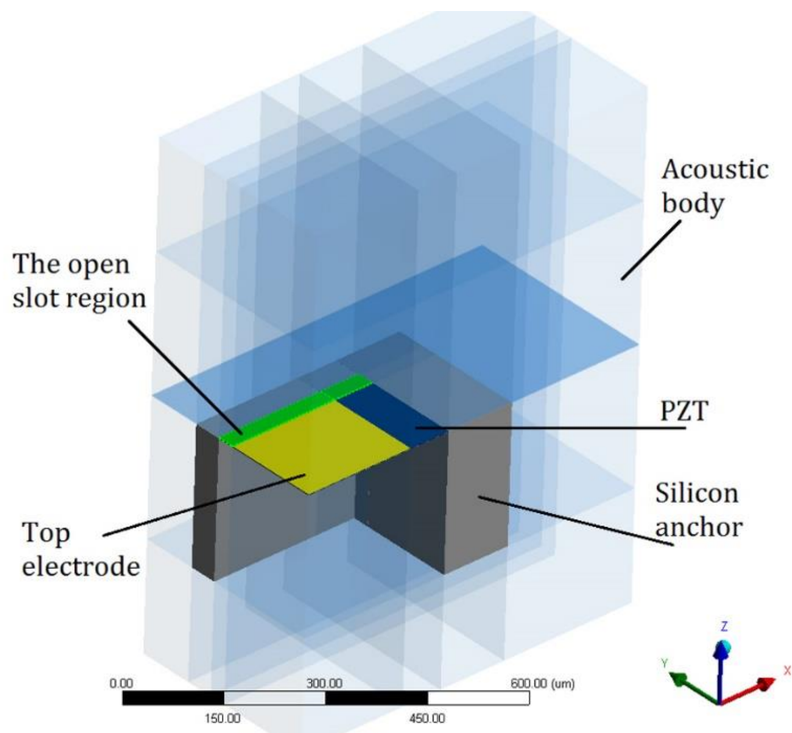

Figure 2-5: The finite element acoustic model

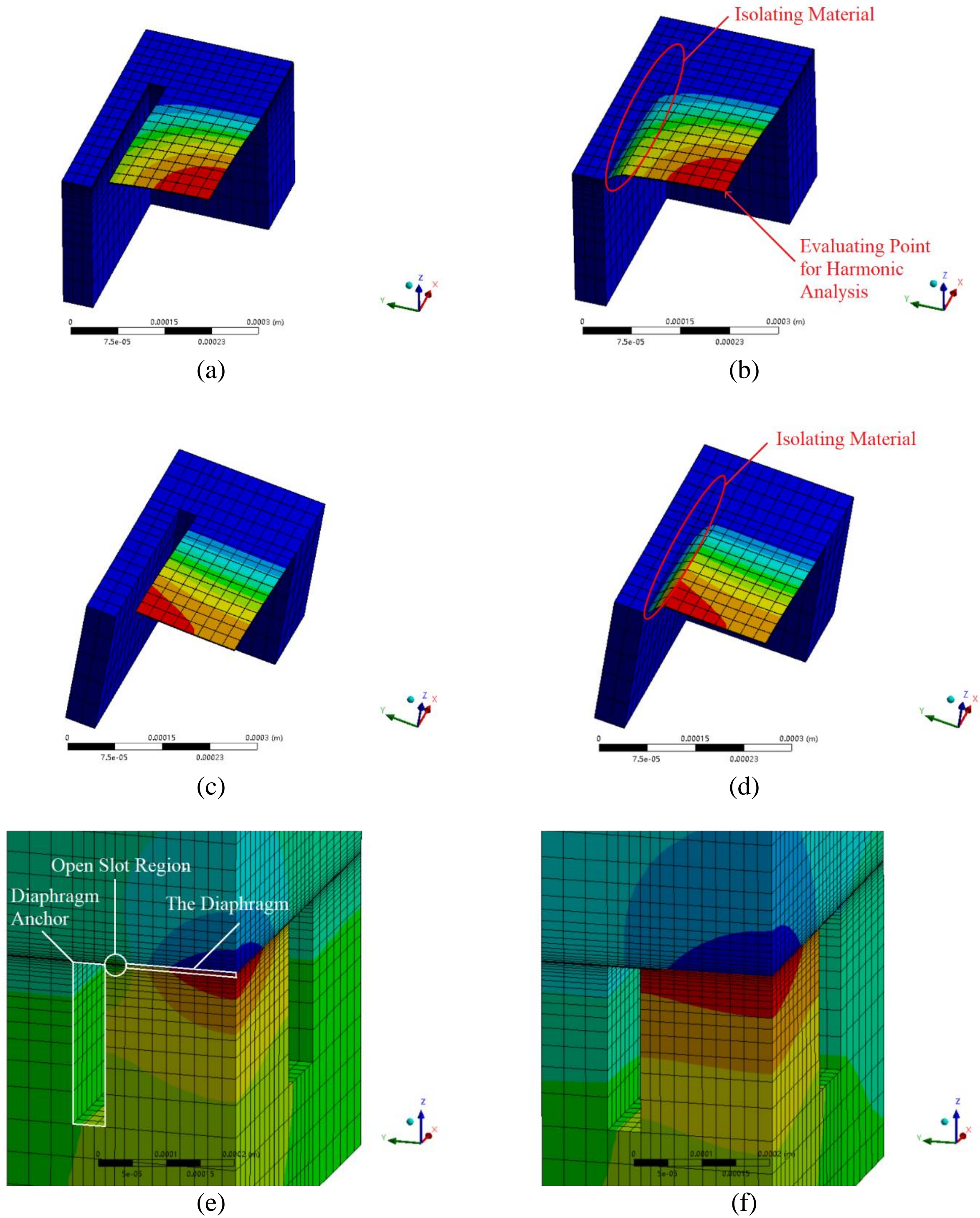

Figure 2-6: FE analysis on 1st mode shape, static gain and acoustic pressure field at 1kHz for both the open slot model and the isolated model
(a) static gain of open slot model; (b) static gain of isolated model;
(c) 1st mode shape of open slot model; (d) 1st mode shape of isolated model;
(e) acoustic pressure field of open slot model; (f) acoustic pressure field of isolated model

In order to investigate the added mass effect, the 1st natural frequencies in fluid need to be extracted by harmonic analysis. Namely, we apply same boundary conditions as before, while the driving voltage frequencies are ramped from 0 to 10 kHz. The damping ratio is set to be 0.01 throughout the simulations, and the deflection of a point at center of the diaphragm (shown in Figure 2-6 (b)) in z-direction (i.e., the out-of-plane direction) is evaluated. The results of the harmonic analysis suggest the 1st natural frequencies in fluid to be 5.16 kHz for the open slot model and 3.28 kHz for the isolated model. Comparing to the results of modal analysis in air (c.f. Figure 2-6 (c) and (d)), the 1st natural frequencies become 27.48% (i.e., $(5.16/18.78) \times 100\%$) for the open slot model and 17.40% (i.e., $(3.28/18.85) \times 100\%$) for the isolated model. Thus, by partially releasing the diaphragm, the added mass effect is reduced and the bandwidth is expanded. This is reasonable since the acoustic pressure on two sides of the diaphragm is now allowed to be released via the open slots, causing smaller pressure difference. Smaller pressure difference also means smaller added mass. From design point of view, the partially released diaphragm is advantageous in producing a larger bandwidth.

In summary, although the partially released model may reduce the acoustic pressure by about 50%, the bandwidth is conversely expanded. Therefore, from acoustic point of view, the partially released model is feasible for intra-cochlear micro-actuator applications.

2.1.5 Challenges of the partially released design

The partially released design shows promising performance in terms of static gain and bandwidth, as well as acoustic properties. However, there are several challenges existing along with this design. One challenge is from the residual silicon (discussed in Section 1.3). Namely, the presence of residual silicon further increases the stiffness of the diaphragm. Since the partial

release will be done by through etching all the material in the open slot area, including the residual silicon, the stiffness of the diaphragm will change at the same time. On the other hand, this also means that the width of the through etched slots may significantly affect the equivalent stiffness of the diaphragm. Therefore, it is important to determine the optimized width for the diaphragm. However, the actual size of the residual silicon after the scale down remains unknown.

Another challenge comes from fabrication. Although compared with the cantilever option, the partially released diaphragm is much more preferred, it is still not a trivial task in the sense of fabrication. Namely, the partially released structure adds much complications. In order to through etch the open slots, the top layers including the bottom electrodes, the PZT and the top electrode must be patterned to avoid those areas. Although the recipes for fabricating and patterning individual layers are well established in literature [28, 33], the influence of the patterns, especially their interactions when multiple layer patterning is performed, remains unknown. For example, it will be discussed in the fabrication session that the patterning of bottom electrode can cause non-uniformity to the annealing results due to the change of surface topology. Furthermore, as many as 6 layers of patterns must be properly aligned, which requires high accuracy. As multiple methods are to be involved in fabrication such as wet etching and high temperature annealing, the alignment mark must be both accurate and robust enough to guide the patterns.

2.2 Fabrication

This section shows the fabrication of the partially released actuator. A brief fabrication flow is first introduced as an overview, followed by discussions of detailed procedures. Namely,

in “pre-fabrication design” section, the actuator layout design, photo-mask design and alignment mark design are introduced. For fabrications, challenges such as bottom electrode patterning and annealing, patterning of PZT and formation of partially released diaphragm are shown. Finally, the fabricated actuator with partially released diaphragm will be illustrated.

2.2.1 Brief fabrication flow

Figure 2-7 schematically shows the fabrication flow of the intra-cochlear PZT micro-actuator with partially released diaphragm. Namely, standard 4”, <1-0-0> oriented, p-type wafers are utilized as substrates and are cleaned by standard RCA methods. As shown in Figure 2-7(a), 500 nm of silicon oxide and 200 nm of silicon nitride are first deposited on bare wafer as isolation layers using wet thermal oxidation and low-pressure chemical vapor deposition (LPCVD). After deposition, alignment marks are created on top of the substrate by photolithography and etching of silicon nitride. Bottom electrode consisting of 50 nm titanium and 100 nm platinum is then deposited onto the substrate by e-beam evaporation shown in Figure 2-7 (b). The patterns of bottom electrodes are created by lift-off. After the bottom electrode deposition, proper post treatments including sonicating bath and annealing are required to prepare the surface for PZT deposition. The PZT layer is fabricated by sol gel methods. Thus, the PZT sol gel is first made and deposited on substrates by spin coating. The substrates are then quickly transferred to furnace to be sintered at 650 ^{o}C. For the patterning of the PZT layer, 10: 1 buffered hydrofluoric acid (BHF) is first utilized to etch the PZT, followed by 37% hydrochloric acid (HCl) bath to dissolve the residual metal fluorides [33]. The substrate after PZT patterning is shown in Figure 2-7(c). We then use 25 nm of chromium as adhesion layer and 500 nm of gold as top electrode. These two metals are again deposited by e-beam evaporation and patterned

by lift-off (Figure 2-7(d)). The diaphragm is partially released by double side DRIE (Figure 2-7 (e) & (f)), which will be discussed in detail in section 2.2.6. After the two etching steps, the diaphragms are partially released and all actuators are separated from the substrate, ready for testing. A detailed fabrication recipe is attached in the end of this dissertation in Appendix A.

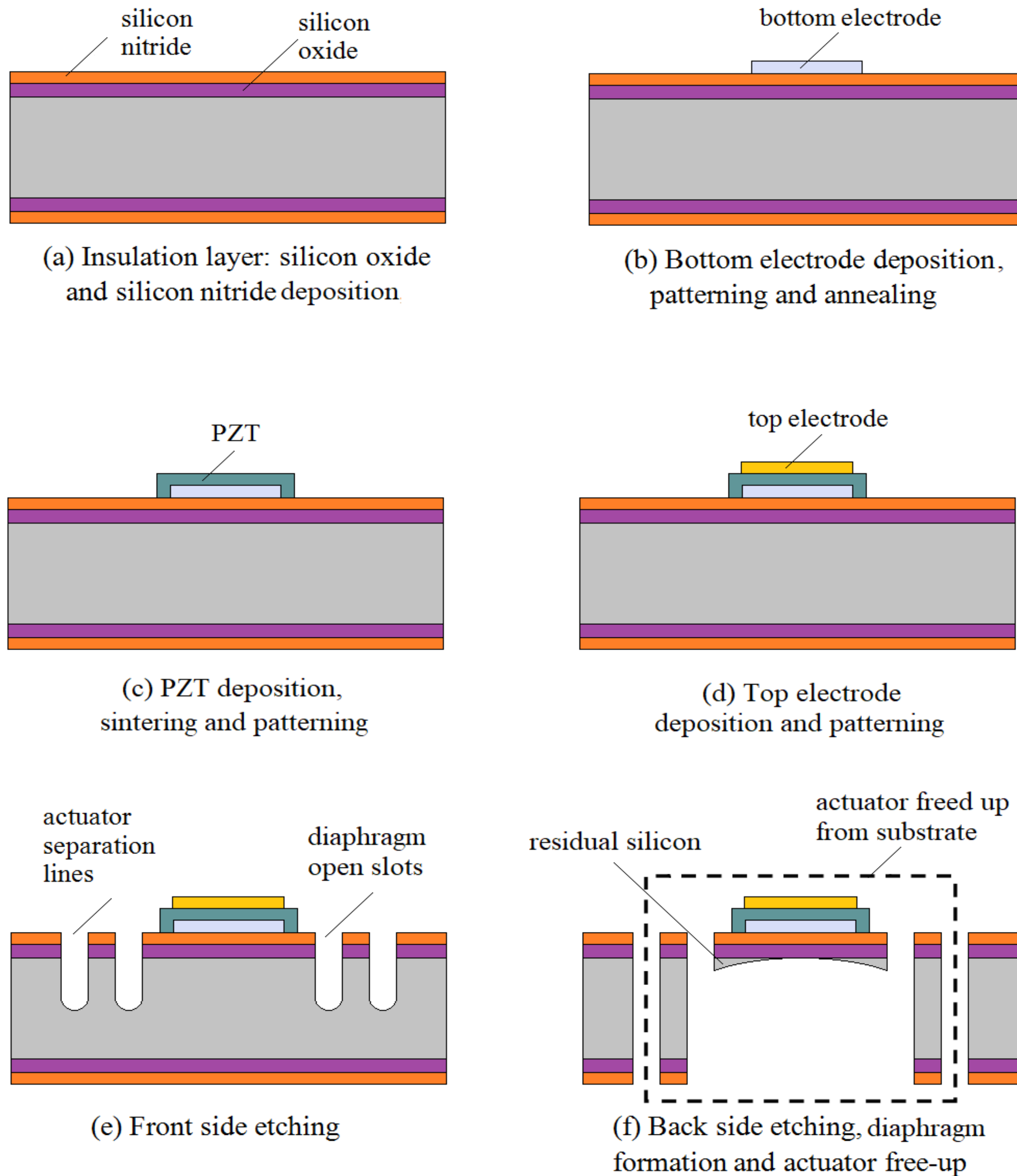

Figure 2-7: Fabrication flow of PZT micro-actuator with partially released diaphragm

2.2.2 Pre-fabrication designs

This section shows the three main design steps before fabrication of the PZT micro-actuator. They are actuator layout design, photo-mask design and alignment mark design.

2.2.2.1 The actuator layout design

The new actuator with partially released diaphragm will also be placed at the tip of a silicon probe (like the 1-G probe). We call such device "2-G probe" for the rest of the dissertation. Since multiple 2-G probes can be fabricated in a single batch (i.e., a 4" silicon substrate), proper layout designs are required to ensure yield and fabrication qualities.

The 1-G probes acquire a radial layout as shown in Figure 2-8 (a). The reason for such design is to maximize the yield [28]. However, when such layout is utilized, the probe orientations must also be along the radial directions, which is not necessarily consistent with the <1-0-0> intrinsic orientations of the silicon substrate. Furthermore, because the 1-G probes only go through DRIE once on the backside, the separation lines are not etched through. Therefore, 1-G probes require manual separation from the substrate by breaking apart along the separation lines. As a result, the edges of the 1-G probes usually show jagged finish (refer to the front side view of the actuator in Figure 1-2). Those sharp edges can cause stress concentration and break the actuator tip during operations, as well as accidentally damaging inner ear tissues during intra-cochlear surgeries.

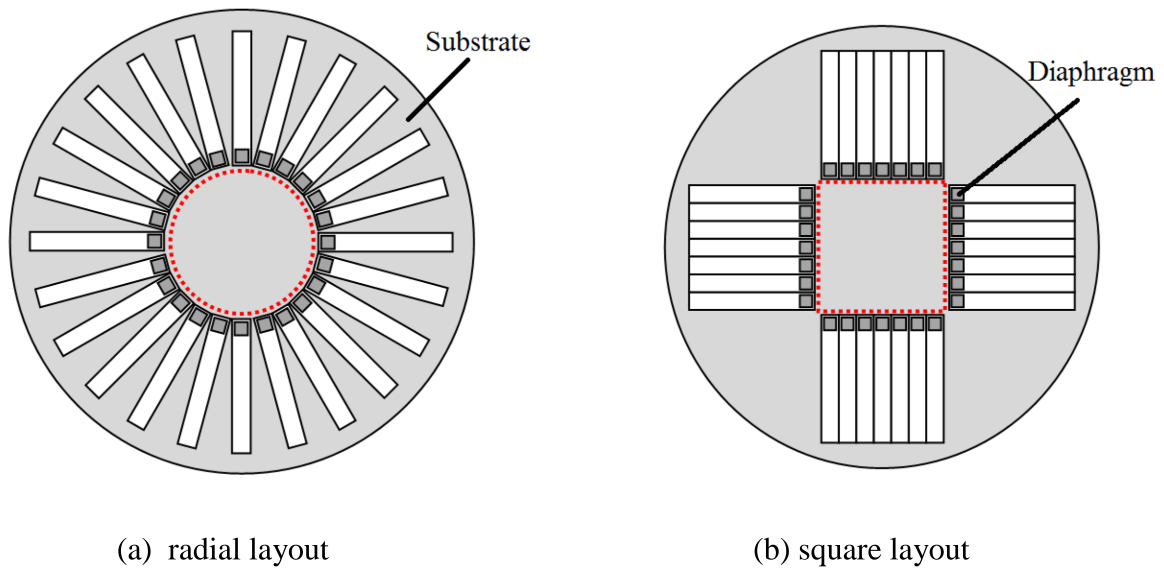

(a) radial layout (b) square layout

Figure 2-8: Actuator layout designs
(a) radial layout; (b) square layout

The 2-G probe accepts square layout shown in Figure 2-8(b) for three reasons. First, 4" wafers instead of 3" wafers are now utilized as substrates. As the surface area is enlarged, radial layout is no longer necessary to ensure the yield. Second, by placing probes in a square, the orientations now become consistent with the intrinsic <1-0-0> direction, which will significantly improve edge smoothness and reduce stress concentration. Finally, because of the double side etching using DRIE to fabricate the open slots, the probes are separated from the substrate at the same time. Thus, no hand separation is required

In the later section 2.4.2, it will be shown that the square layout is neither an ideal design as it may cause non-uniformity in DRIE. Such phenomenon and its solutions will be discussed later.

2.2.2.2 The photo-mask design

The patterning is based on lithography of six layers. Therefore, six photo-masks must be designed and fabricated first. They are alignment mark mask, bottom electrode lift-off mask, PZT etching mask, top electrode lift-off mask, front side DRIE etching mask and backside DRIE etching mask. Figure 2-9 shows those masks in the design stage. In particular, Figure 2-9(a) shows the mask designs as an overview at the tip of the probe, while Figure 2-9(b) is a blow-up view of each layer. Notice that three partially released diaphragms are placed at one single probe tip for the 2-G probe.

For dimension parameters, various factors are considered. One example is in designing the PZT mask. The PZT will be eventually patterned by wet etching, using a 10: 1 BHF solution, which may also attack the bottom electrode. Therefore, the PZT layer is designed to cover the entire bottom electrode area. Furthermore, s BHF may also attack in lateral directions by a ratio of approximately 10:1 [33], a 20 μm safe margin is left considering the fact that the PZT layer is approximately 1μm thick. Another example is in designing the soldering pads. It is known that the electrical corner frequency of the device must be high enough to effectively drive the PZT diaphragm [34]. That means the equivalent capacitance must not be too large. Since the soldering pads occupies up to 90% of the entire metal area, reducing its size may significantly lower the equivalent capacitance. After a series of tests, it is known that the soldering pads can be made into circular dots of only 400 μm in diameter while still acquiring good connectivity. This may significantly increase the electrical corner frequency.

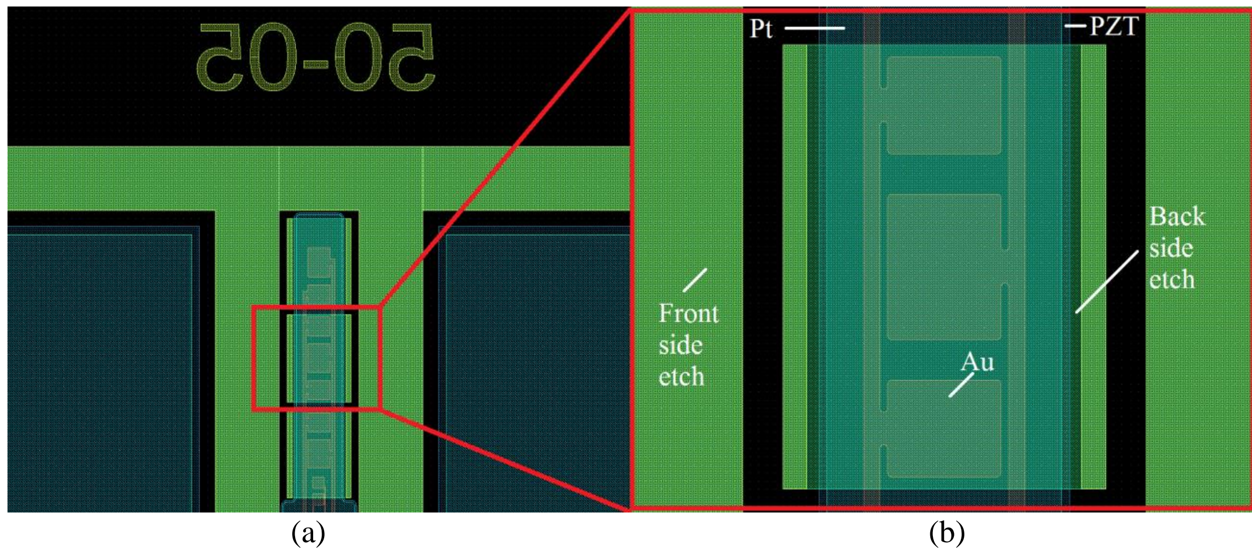

Figure 2-9: The mask design of the 2-G probe at the tip portion
(a) the overview; (b) blow-up view at one single diaphragm

2.2.2.3 The alignment mark design

Alignment marks are utilized to properly align different layer patterns to acquire desired functionalities. Since there are six layers to be patterned in the fabrication of 2-G probe, large misalignment may occur if one aligns each layer based on the previous one. A better strategy is to align all the other layers according to the very first one.

The alignment marks are created by etching the deposited silicon nitride layer, exposing the underneath silicon oxide (c.f. Figure 2-7 (a)). There are three reasons for using silicon oxide as alignment marks. First, silicon oxide is inert to most of the processing steps. Although after PZT etching, the silicon oxide will be stripped by BHF, the underneath bare silicon can still provide accurate alignment. Second, the alignment marks are printed on the wafer by shallow dry etching of the surface silicon nitride, which can be done with very high precision. Third, silicon oxide is purple colored under optical microscope, which is very easy to distinguish.

Figure 2-10 shows the alignment mark design on the left side of the substrate. There is another alignment mark in the symmetric position on the right side to align in-plane rotations. Notice that there are three patterns, course alignment mark, fine alignment mark and backside alignment mark. The course alignment mark (the largest one) guided by several arrows is very easy to allocate. After course alignment, one can better align the mask by the fine alignment mark (the small one) on the left side. (Refer to the blow-up view in the lower left of Figure 2-10.) The backside alignment mark is particularly used for alignment of the backside etching mask. (Refer to the blow-up view in the lower right of Figure 2-10.)

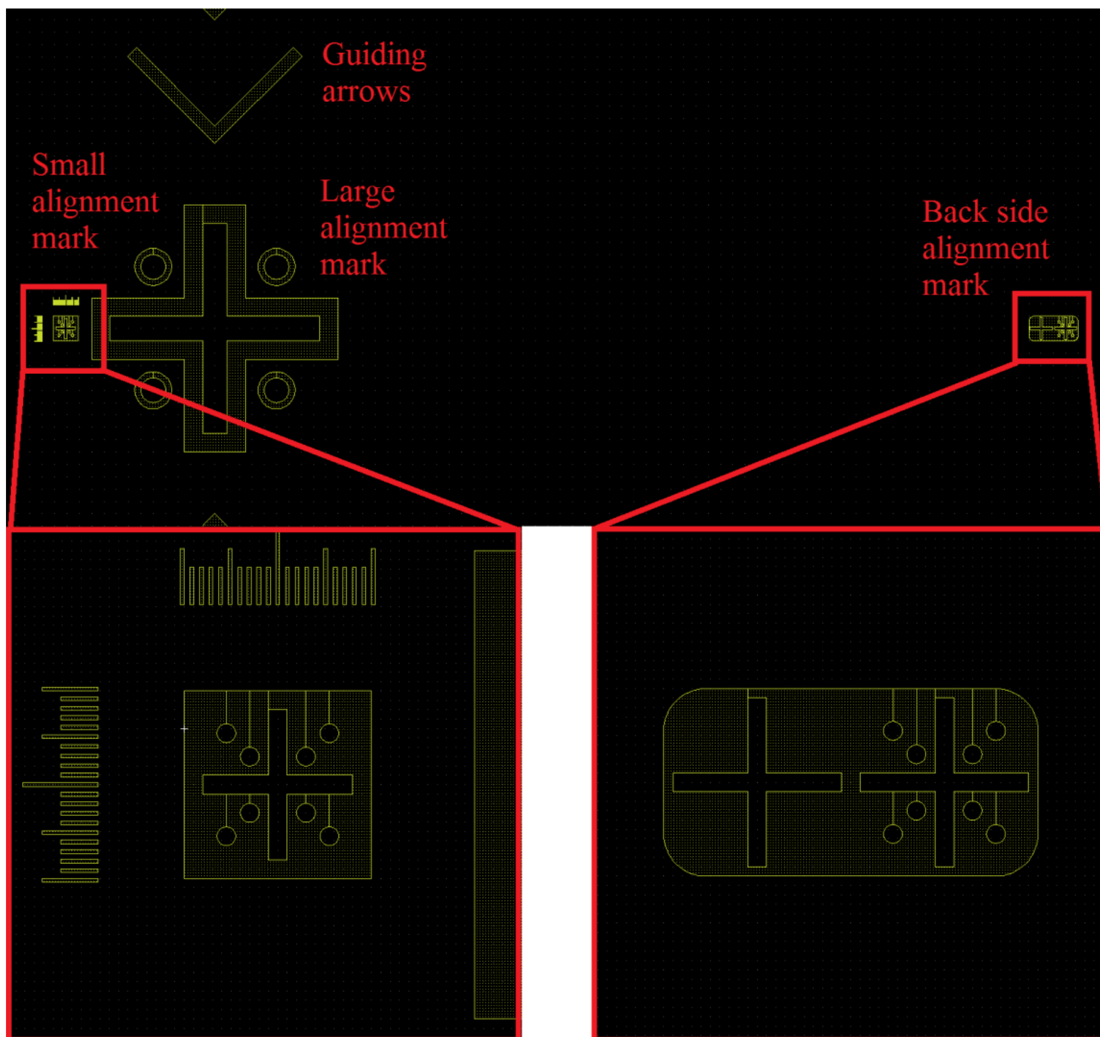

Figure 2-10: The alignment mark designs

2.2.3 Patterning of bottom electrode and elimination of “cat ears”

Chromium and gold are common deposition metals because of their ideal adhesion and accurate patterning using negative photo-resists. However, these metals cannot be applied to the bottom electrode because gold will become soft and induce large deformation in high temperature during the later PZT sintering step, which may cause the brittle PZT to crack or delaminate. Instead, titanium and platinum are utilized because of their relatively higher melting points. However, there are still challenges in patterning titanium and platinum as bottom electrodes.

One challenge is deposition temperature. The bottom electrode uses e-beam evaporation so that the metal patterns can later be created by lift-off. However, unlike chromium and gold, the temperature during platinum deposition may exceed 250°C. Such high temperature and fast heating / cooling process may introduce large strain to the silicon wafer surface, peeling off the negative photo-resist. Therefore, we must use positive photo-resist for deposition. But using positive photo-resist may introduce a new problem called “cat ear” in the later lift-off process. Namely, unlike negative photo-resist which forms an inward profile in the cross section after UV exposure and developing (shown in the upper left picture of Figure 2-11), positive photo-resist forms an outward cross section profile (shown in the upper right picture of Figure 2-11). This is problematic in the later lift-off step. For negative photo-resist, due to the inward profile, the metal is naturally separated at the patterning boundaries (shown in the lower left picture of Figure 2-11). However, for positive photo-resist, due to the outward profile, the metal will connect at the pattern boundaries instead, which makes it difficult to perform lift-off. Even if the metal layer is thin enough to be physically separated, there will be residual metal appearing at the pattern boundaries called “cat ear”.

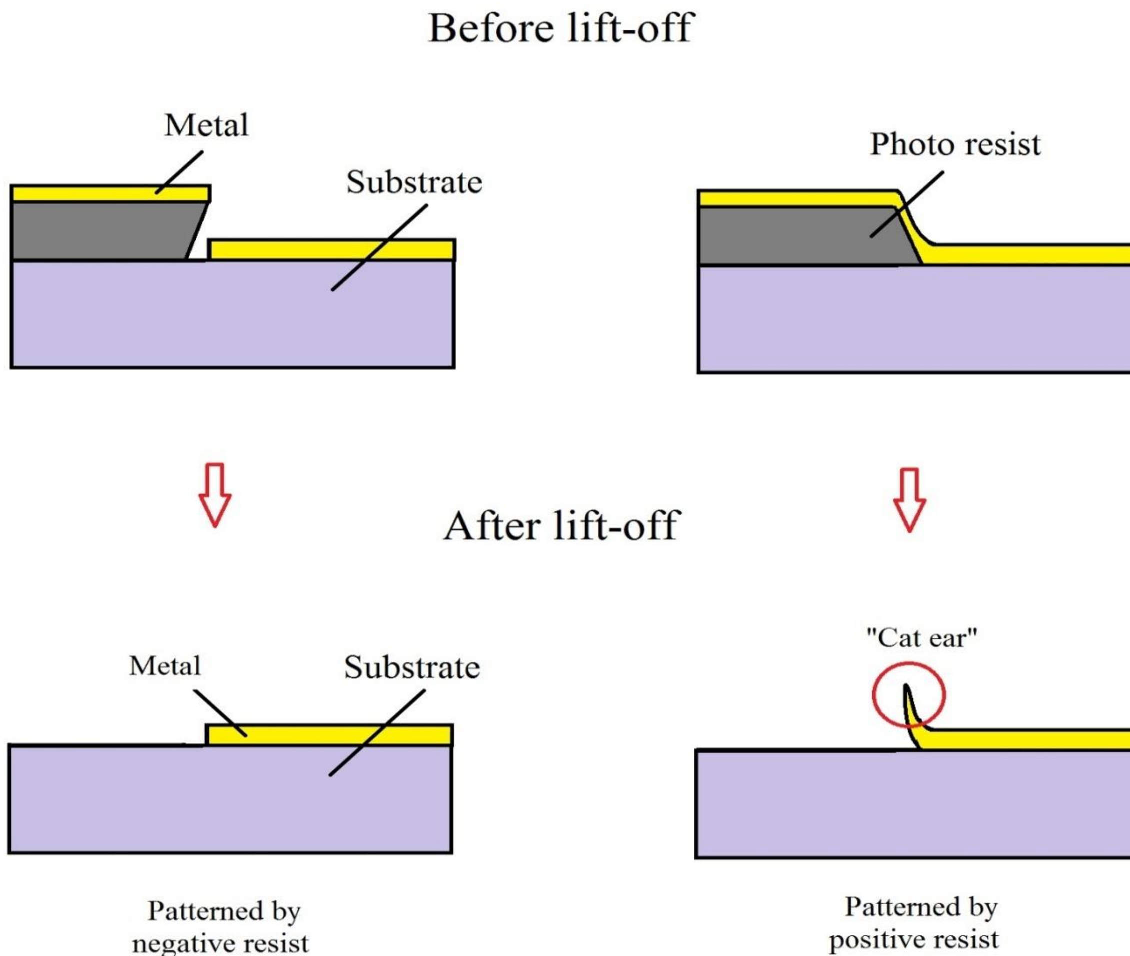

Figure 2-11: Difference in positive and negative photo-resists in patterning by lift-off

In our case, a positive photo-resist called AZ-1512 (from AZ Electronic Materials Inc.) is utilized. The top view of the patterned bottom electrode using this photo-resist is shown in Figure 2-12 (a). From the picture, one can clearly see “cat ear” at the pattern boundaries. To quantitatively specify this problem, surface profile is scanned along the path indicated in Figure 2-12(a) and the result is shown in Figure 2-12(b). Thus, the height of the “cat ear” is more than 9 μm, which is significantly larger than the thickness of the entire diaphragm. Such long “cat ear”

can easily penetrate the PZT layer and inter-connect with the top electrode, causing short circuit. Therefore, to use positive resist to pattern the bottom electrodes, the "cat ear" must be eliminated.

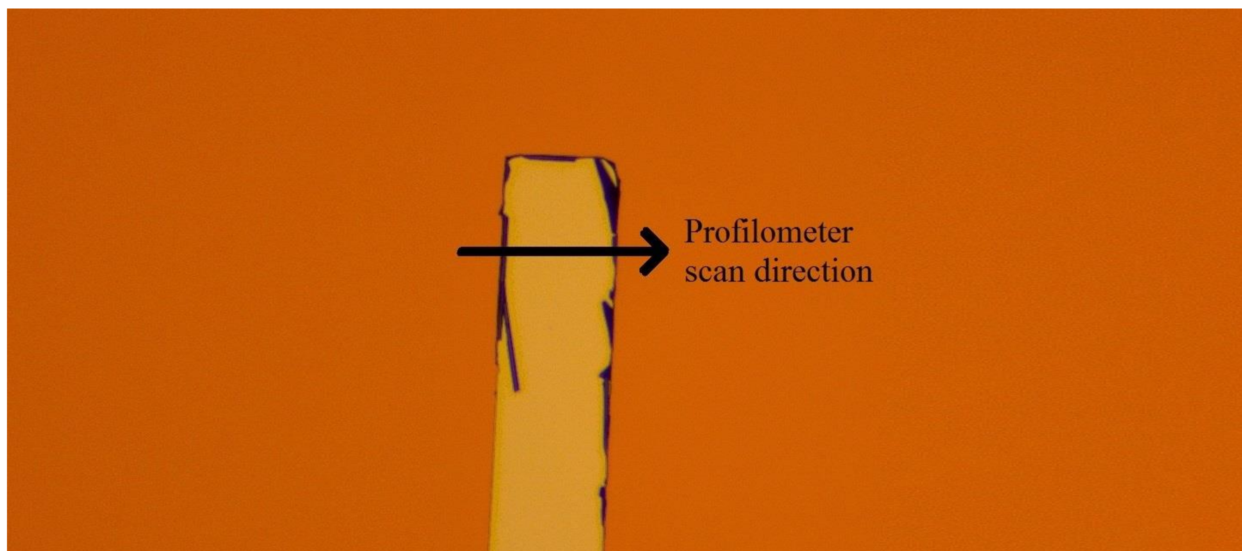

(a) the "cat ear" observed under optical microscope

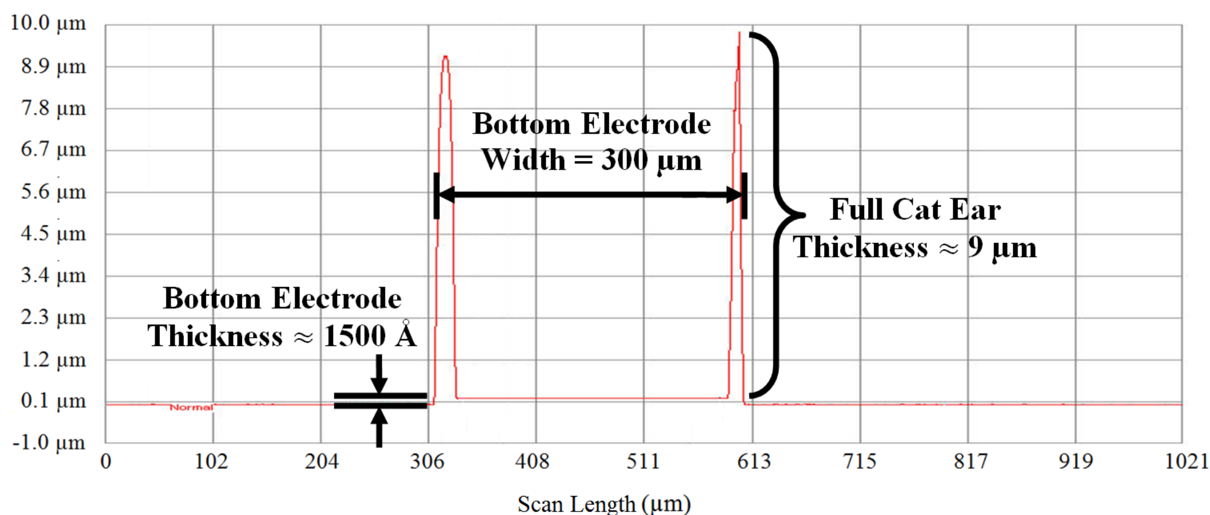

(b) profile of the metal and substrate surface before right after lift-off

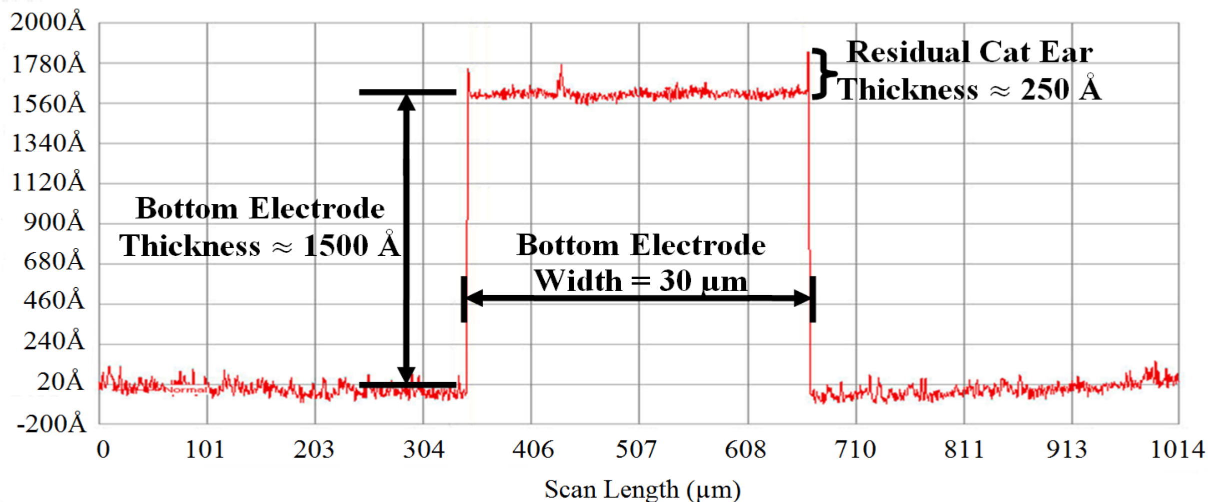

(c) profile of the metal and substrate surface after sonicating bath

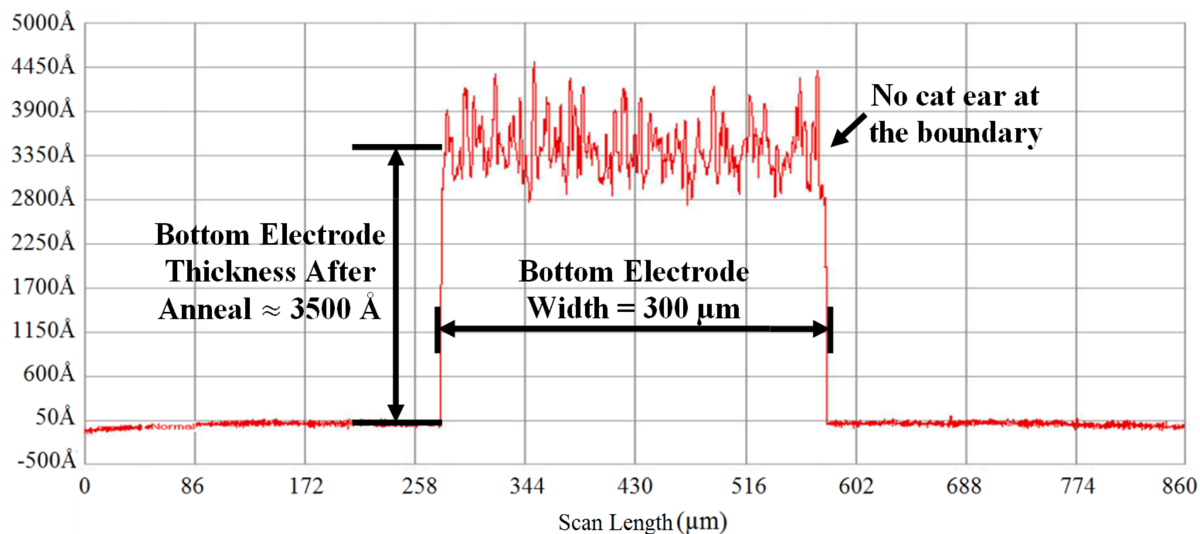

(d) profile of the metal and substrate surface after annealing

Figure 2-12: The existence and elimination of the "cat ear"

(a) "cat ear" viewed by optical microscope; (b) bottom electrode profile right after lift-off;

(c) bottom electrode profile after sonicating bath; (d) bottom electrode profile after annealing

Fortunately, the long "cat ear" at the pattern boundaries is also fragile enough to be physically broken under vigorous agitations such as sonicating bath. As one can tell from the surface profile after sonicating bath shown in Figure 2-12(c), the "cat ear" height is substantially decreased to approximately 25 nm. Furthermore, the short "cat ear" can be totally eliminated by

bottom electrode annealing. Although the primary purpose of annealing is to lease the internal stress in bottom electrodes accumulated during the e-beam deposition (see section 2.2.4), the high temperature environment also adds extra mobility to the metal that migrates and flattens the “cat ear”. Figure 2-12(d) shows that after annealing, the “cat ear” is totally eliminated.

One last problem for patterning with positive photo-resist would be precision, since it is commonly accepted that lift-off using negative photo-resist is much more accurate than positive photo-resist. In our case, because of the low viscosity of AZ-1512, the spin coated photo-resist is very thin. Therefore, the precision for the bottom electrode is within $2\ \mu\mathrm{m}$, which is acceptable.

2.2.4 Annealing of bottom electrode

The high temperature and fast heating / cooling process may not only cause negative photo-resist to delaminate but also introduce large tensile stress to the deposited electrode layer. Such internal stress will become problematic when one deposits the PZT using sol gel methods. Namely, to crystalize the PZT sol, the substrate needs to be heated up to $650\ ^{\circ}\mathrm{C}$. Under such high temperature and the intrinsic stress, the metal may deform, causing the PZT to delaminate. Therefore, according to fabrication of the 1-G probe [35], the bottom electrode needs to be annealed after the bottom electrode is deposited to release internal stress. Such metal annealing is typically performed over $750°C$. After annealing, the bottom electrode (especially the platinum) shows highly porous structure, which is crucial for successful anchoring of the PZT layer. Typically, $30 - 35\%$ porosity (i.e., area of the pores divided by the total metal area) is required for a successful PZT deposition [35]. Both too high porosity or too low porosity may cause the PZT to delaminate. A SEM photo of properly annealed bottom electrode is shown in Figure 2-13(a).

To achieve such porosity, the annealing conditions for 1-G probe is to ramp from room temperature to $800°C$ and dwell for $15 - 25$ minutes. After the dwelling process, the furnace is turned off and the substrate is cooled naturally to room temperature. This annealing recipe, however, is invalid for patterned bottom electrodes. As shown in Figure 2-13 (b), the porosity of a typical bottom electrode varies from its central to its boundary areas. If the center area is properly annealed, the metal near the pattern boundaries would be under annealed. As a result, one cannot achieve uniform and properly annealed condition.

The hypothesized reasons for the non-uniformity in bottom electrode annealing are as follows. First, given enough dwelling time, the final state of annealing would be determined by the dwelling temperature. Thus, the bottom electrodes will eventually develop porosity of the same level throughout the substrate. However, if the annealing time is inadequate, the metal annealing cannot reach a steady state. In such transient state, slight difference in metal layer thickness can produce vastly different porosities. In particular, thicker metal layers may develop lower porosity than thinner layers. As discussed in Section 2.2.3, “cat ear” exists after bottom electrode deposition and lift-off. Although sonicating bath can eliminate most of the “cat ear”, a short residue still exists at the boundary areas before annealing. Such residual metal will migrate and merge into the bottom electrode in the high temperature dwelling, causing the boundary areas to be slightly thicker. If the annealing process is terminated in transient state, those areas (i.e., the boundary areas) will be less porous than areas of thinner metal (i.e., the center areas), and thus under annealed.

Second, the patterning of bottom electrode itself also contributes to the non-uniformity. After the lift-off, the deposited metal in most of the area departs from the substrate and the underneath silicon nitride is exposed. Again, if enough time is allowed, the thermal conditions

(especially the temperature) of the whole substrate surface will eventually become the same. However, for transient states, especially in the fast cooling process right after dwelling, due to the inhomogeneous surface topology, both the thermal conditions and mechanical conditions (e.g. the stress in the bottom electrode) will be slightly different, especially at the boundary areas. Those difference in thermal and mechanical conditions will also cause non-uniformity in annealing.

Therefore, the previous recipe must be modified to accommodate for substrates with patterned electrodes. Considering the above reasons (i.e., the residual metal at the boundary due to "cat ear" and the different surface topology), one can conclude that the thermal conditions will become homogeneous if enough time is allowed. Therefore, we designed the new annealing recipe as follows.

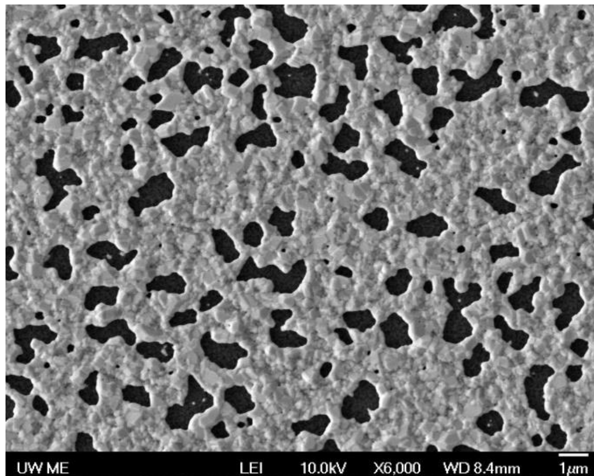

(a)

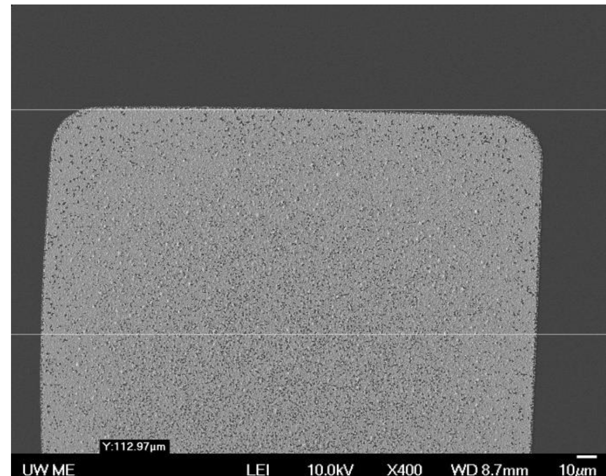

(b)

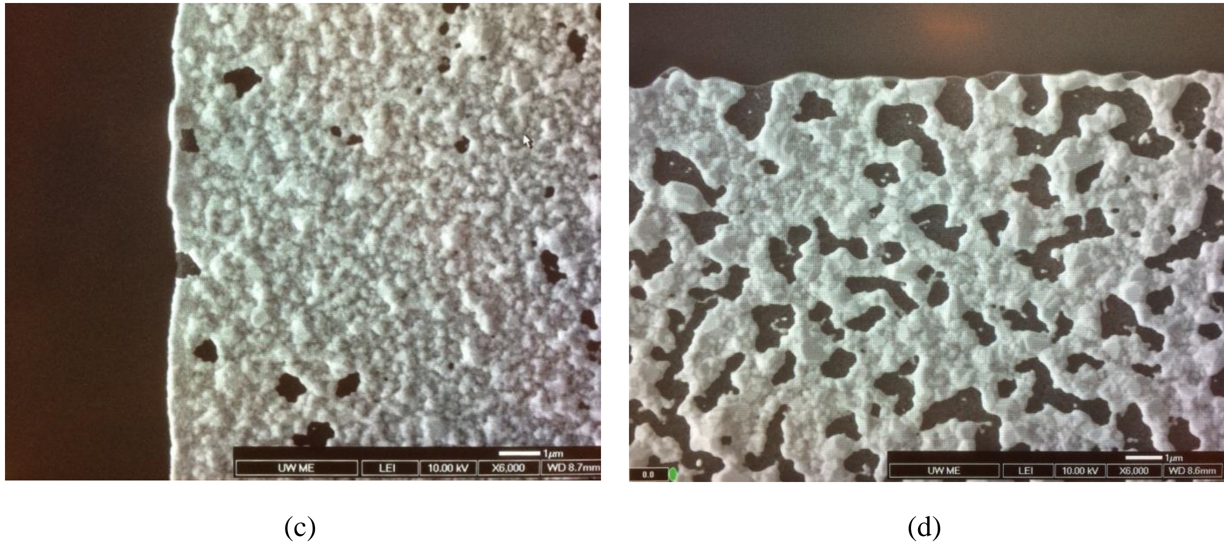

Figure 2-13: The bottom electrode annealing

(a) typical properly annealed condition; (b) SEM photo of the bottom electrode tip after annealing, using annealing recipe of the 1-G probe; (c) the “under annealed” condition near the patterning boundaries, using annealing recipe of the 1-G probe; (d) the “properly annealed” condition near the patterning boundaries, using annealing recipe of the 2-G probe

First, we set the dwelling temperature slightly lower (typically $790°C$) than the previous recipe ($800°C$) while elongating the dwelling time to 60 minutes to ensure fully annealed condition for both the center and the boundary areas. Second, instead of letting the substrate to cool down rapidly by turning off the furnace, a temperature profile is programed and feed-back controlled so that the temperature drop becomes slow and linear. The whole process lasts for 9 hours. Fig 18(d) shows the porous bottom electrode structure near the patterning boundary after the new annealing strategy is adopted. Compared with the previous annealing result in Fig 18(c), the porosity is significantly improved.

2.2.5 Patterning of PZT

The patterning of PZT includes deposition and etching. The deposition process is like that of the 1-G probe. Namely, the PZT sol gel is first made [28], and spin coated onto the substrate. The coated sol gel is then sintered at $650°C$, forming a crystalized PZT layer of approximately 1 μm. Such process is successful in producing crack-free PZT on top of the bottom electrode. However, because the new bottom electrode is patterned, part of the PZT sol will be coated onto the silicon nitride layer. Because the adhesion of PZT to silicon nitride is quite weak, the coated PZT layer will delaminate and crack, forming small shreds that spread onto the surface of bottom electrode. Figure 2-14 (a) shows a typical bottom electrode after PZT deposition, one can clearly see that the PZT on the bottom electrode area is successfully deposited, but the PZT on silicon nitride delaminates and creaks. Besides, there are several shreds spread onto the bottom electrode area. This is problematic because the shreds may hinder the later top electrode deposition or even cause open circuit if one shred happens to be at the position of wiring (c.f. Figure 2-14 (c) shows an open circuit condition as one shred is in the spot of the top electrode wiring in the lower right corner). Fortunately, those shreds can be eliminated by physical methods such as strong air flow or sonicating bath. Figure 2-14 (b) shows the results after a strong air flow treatment. The condition is much better that only a few small shreds exists on top of the surface, which will not hinder the top electrode (c.f. Figure 2-14 (d)).

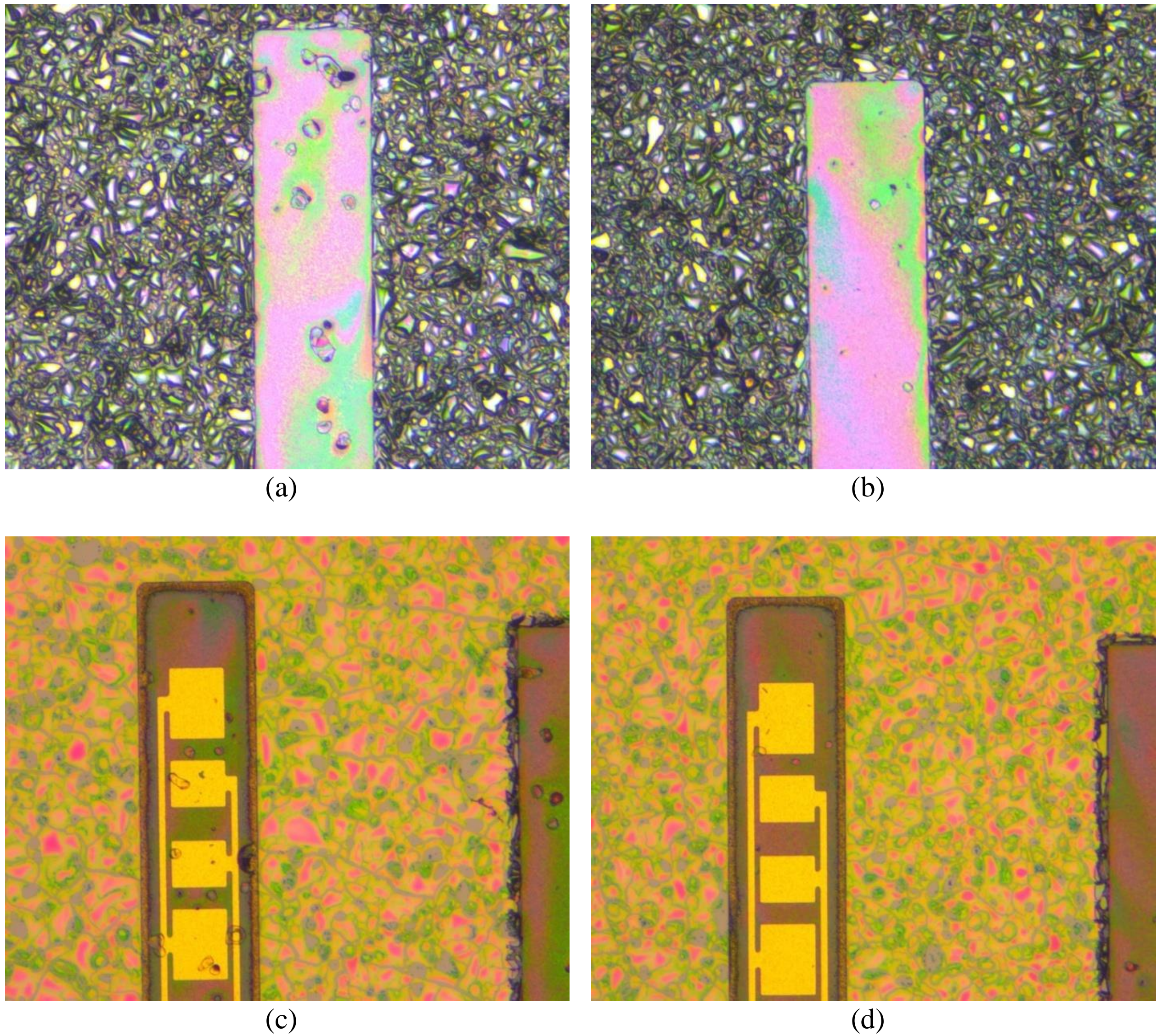

Figure 2-14: The PZT layer fabrication and PZT shreds processing
(a) actuator tip after PZT sintering, without air flow treatment;
(b) actuator tip after PZT sintering, with air flow treatment;
(c) actuator tip after top electrode deposition, without air flow treatment;
(d) actuator tip after top electrode deposition, with air flow treatment

The patterning of PZT is done by wet etching. Namely, the PZT is first patterned and protected by thick photo-resist (AZ-9260 from AZ electronic materials Inc.). The substrate is then submerged into 10: 1 BHF bath for 15 minutes and 37.5% HCl for 2 minutes to etch the

exposed PZT layer [33]. Because wet etching also attacks in lateral directions, undercut may exist at the patterning boundaries. The rate is estimated to be 10: 1. Thus, to etch the PZT layer of 1 μm thick, 10 μm of undercut is expected at the boundary. Furthermore, in order to etch all the exposed PZT, especially those remained on the silicon nitride area as small shreds (c.f. Figure 2-14 (a) and (b)), excessive etching time is required. That means the undercut will become about 20 μm. Figure 2-15 shows the microscopic photo on the edge of the patterned PZT. In particular, Figure 2-15 (a) is focused on the silicon nitride layer (the green and grey colored part), and Figure 2-15 (b) is focused on the top electrode layer (the yellow colored part). Figure 2-15 (a) clearly shows that all the PZT on silicon nitride is eliminated. The green and grey colored areas refer to silicon nitride and silicon respectively. Thus, bare silicon is exposed because the silicon oxide layer has already been etched by BHF. Here we design the safe margin for PZT to be 45 μm, which is more than twice of the expected 20 μm undercut as shown in Figure 2-15 (b).

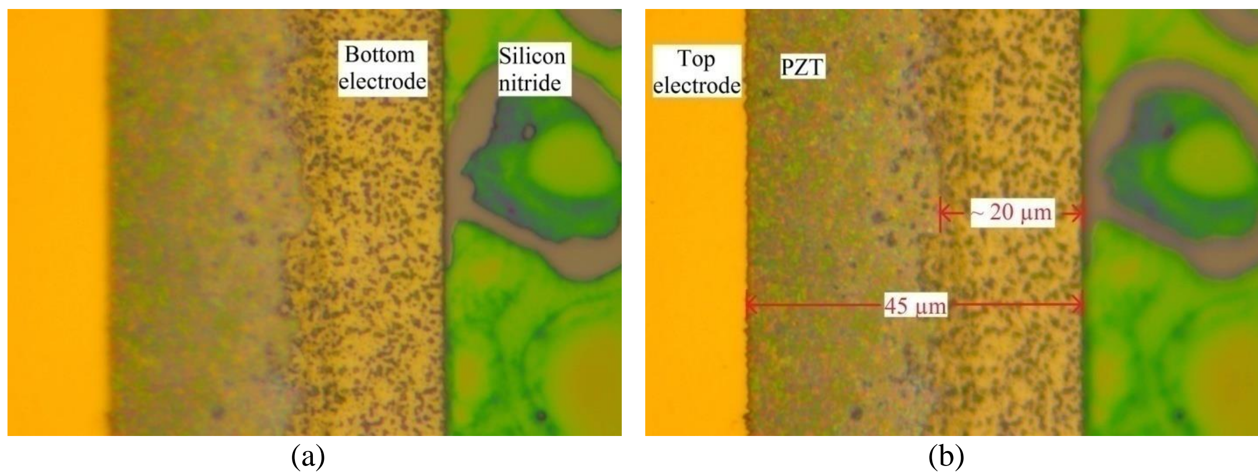

Figure 2-15. Optical microscopic photos of the PZT under cut at the patterning boundaries (a) focused on silicon nitride layer; (b) focused on top electrode layer

2.2.6 Fabrication of partially released diaphragm by double side etching

To partially release the diaphragm, deep reactive ion etching (DRIE) are applied on both sides of the substrate (c.f. Figure 2-7 (e) and (f)). Figure 2-16 (a) and (b) show the mask design of the front side and backside etching respectively, of which the shaded parts mean the areas to be etched. Figure 2-16 (c) is the overlapped view of these two mask designs.

The fabrication details are as follows. First, the front side pattern is created using photo-resist AZ-9260 to protect the PZT and the metal electrodes, exposing only the diaphragm side slots and the probe separation lines (i.e., the shaded areas in Figure 2-16(a)). After lithography, the exposed silicon nitride and silicon oxide are dry etched, followed by DRIE about 75 μm down into the silicon substrate (attacking only the shaded area). Similar processes are performed on the backside. Namely, lithography of thick (about 9 μm) positive resist AZ-9260 is applied to the backside of the substrate, exposing the whole diaphragm area and the probe separation lines (i.e., the shaded areas in Figure 2-16(b)). After the backside silicon nitride and silicon oxide is eliminated, DRIE is again applied to etch down the silicon substrate until the front side silicon oxide layer (the etch stop) is exposed, indicating the formation of a thin diaphragm. Because of the previous front side DRIE of 75 μm into the silicon substrate, both the diaphragm side slots and the probe separation lines are through etched (i.e., the deep green areas in Figure 2-16(c)), forming partially released diaphragms totally separated from the substrate.

One important factor later found to have significant influence upon the diaphragm performance is the etching uniformity. There are two aspects of the problem, residual silicon and unetched silicon layer. Both two problems are caused by the etching non-uniformity of the D-RIE equipment and is difficult to eliminate. Detailed discussions about this problem will be shown in section 2.3.5.

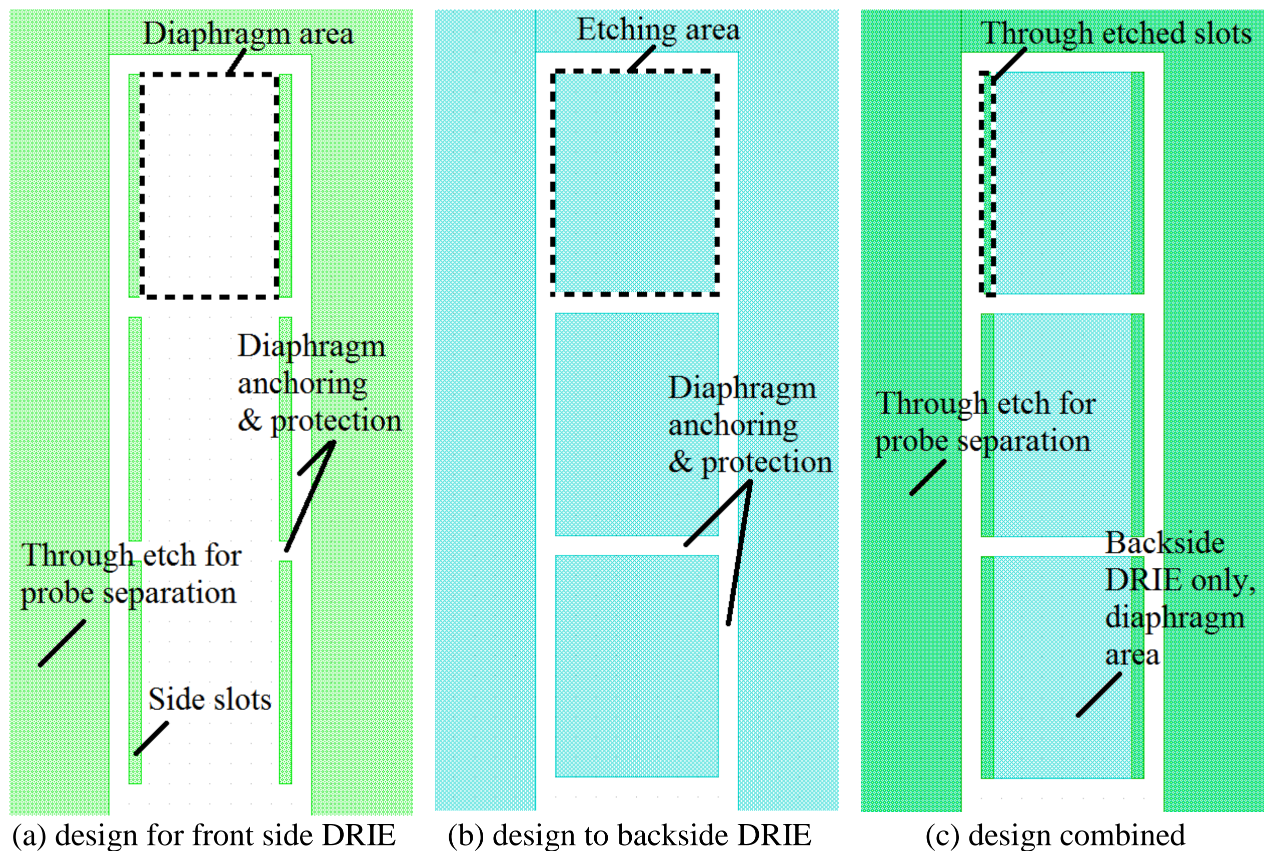

(a) design for front side DRIE (b) design to backside DRIE (c) design combined

Figure 2-16: The front side and backside etching pattern design for the 2-G probes
(a) front side etching design; (b) backside etching design; (c) overlapped configurations

2.2.7 The fabricated 2-G probe

Figure 2-17 shows the tip portion of the prototype 2-G probe, compared with a string of human hair. From the figure, it can be clearly seen that the diaphragm has been released on the two sides. The top electrodes consist of a center electrode and two outer electrodes to maximize the static gain [26]. In addition, one can possibly use the bottom and the center electrode to apply voltage as an actuator, while using the outer electrode to collect the resultant charge (as a sensor). In the characterization tests in section 2.3, voltage will only be applied to the center and the bottom electrodes for simplicity, since we currently focus on the feasibility of the 2-G probe.

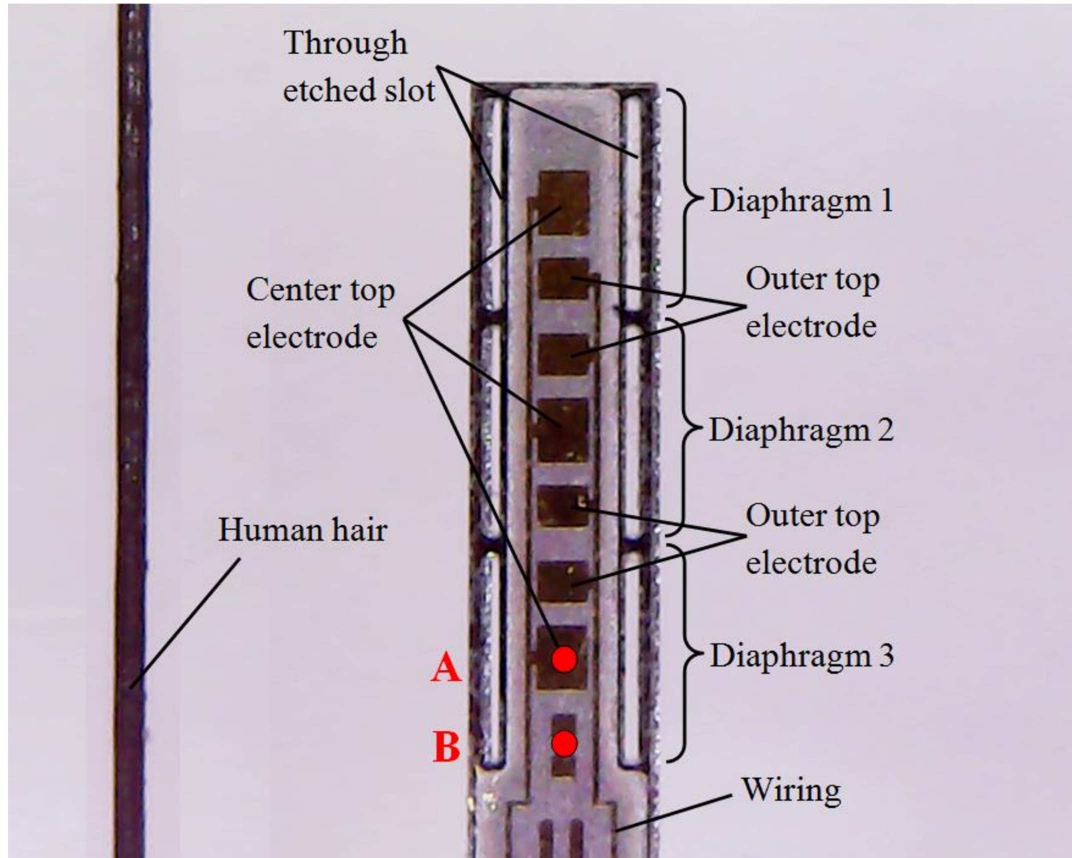

Figure 2-17: The functioning tip of the fabricated 2-G PZT micro-actuator, compared with a string of human hair

2.3 MEASUREMENTS AND DISCUSSIONS

This section investigates the feasibility of partially released diaphragm using the following methods. First, experiments are performed to determine the static gain of the 2-G probe diaphragm, by measuring its frequency response function (FRF). The experimentally acquired static gain and first natural frequency are to be compared with the finite element results. Assumptions are then made to interpret the data and explain the phenomena observed in experiments, which are then proved by either finite element simulations or by experimental tests (or by both). Finally, those parameters are input into the previous finite element model and re-evaluated. The results are again compared to the FRF data to evaluate the validity of the concept.

2.3.1 Experimental setup

The experimental setup includes boundary condition setup and equipment setup. For boundary condition setup, the 2-G probe is "fully clamped", which is realized as follows. As shown in Figure 2-18 (a), the bottom of the probe is first fixed to a slice of glass using excessive epoxy, with a portion of tip sticking out like a cantilever beam. Figure 2-18 (b) shows a blow-up view of such configuration. The glass is then secured to a heavy aluminum block by epoxy.

The experimental setup is schematically illustrated in Figure 2-19. A swept sine signal of 1 V ranging from 100 Hz to 102.4 kHz is first generated from the "source" channel of the spectrum analyzer (Stanford Research Systems, Model SR785). The signal is then magnified by a power amplifier (AVC Instrumentation, 790 Series) and split into two identical signals. One of them is sent to drive the 2-G probe while the other is fed back to the "input" channel of the spectrum analyzer for FRF calculation. When the amplified swept sine voltage is applied to the

probe, the diaphragm starts to vibrate, which is captured by a laser doppler vibrometer (LDV, Polytec OFV511 & 3001). The velocity signal from the LDV is then fed to the "output" channel of the spectrum analyzer to generate frequency response function.

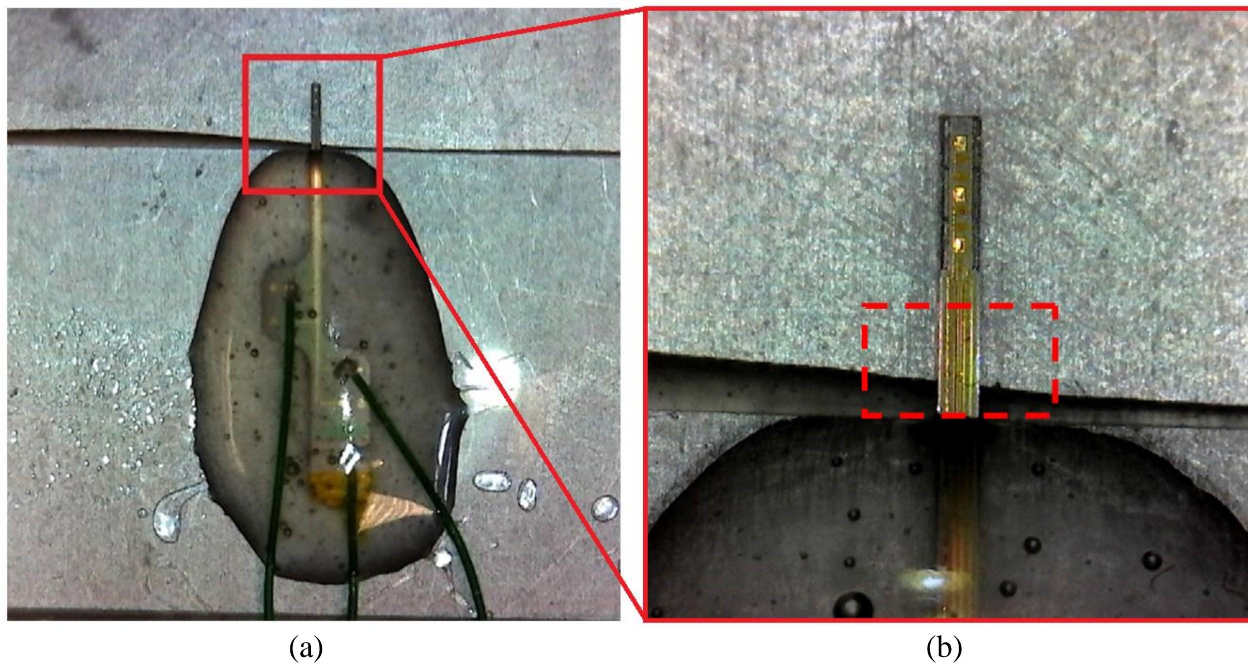

(a) (b)

Figure 2-18: Actuator fixture for frequency response function measurements
(a) overall configuration; (b) the blowup view of the actuator tip

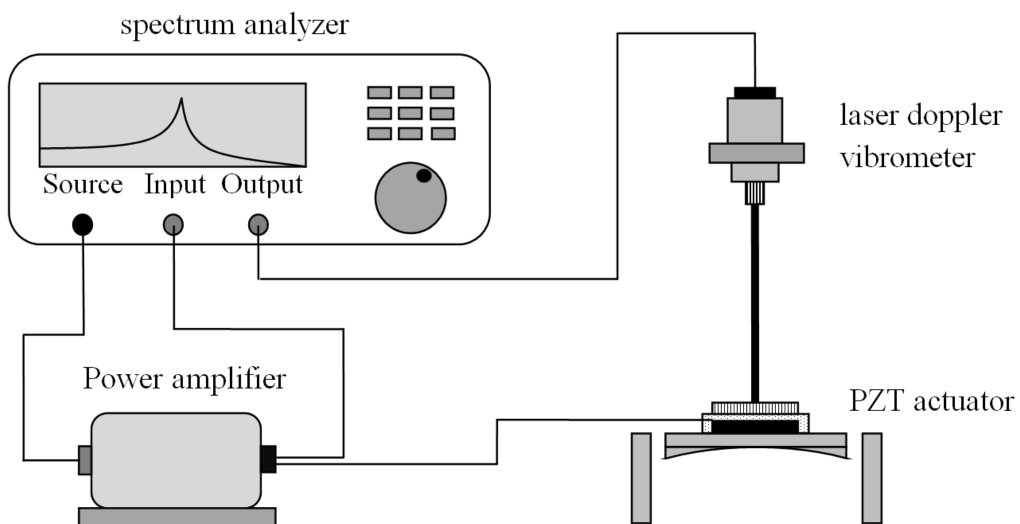

Figure 2-19: The experimental setup for frequency response function measurement

2.3.2 The frequency response function

The resultant frequency response function of the partially released diaphragm is shown in Figure 2-20. The FRF curve shows a rather flat region in lower frequencies (below 30 kHz). The static gain, read from the magnitude of the flat FRF, is 0.44 nm/V (i.e., −7.103 dB of nm/V), substantially smaller than the predicted value given by finite element in Figure 2-4 (12.62 nm/V). Furthermore, it is very odd to see a resonance peak at 60.06 kHz. Assuming same level piezoelectric constants, a much smaller static deflection is usually caused by a much stiffer diaphragm, with extremely high first natural frequency. However, Figure 2-20 shows the first natural frequency of the fabricated diaphragm is even smaller than that of the finite element model (i.e., 86.64 kHz, c.f. Figure 2-4 (d)).

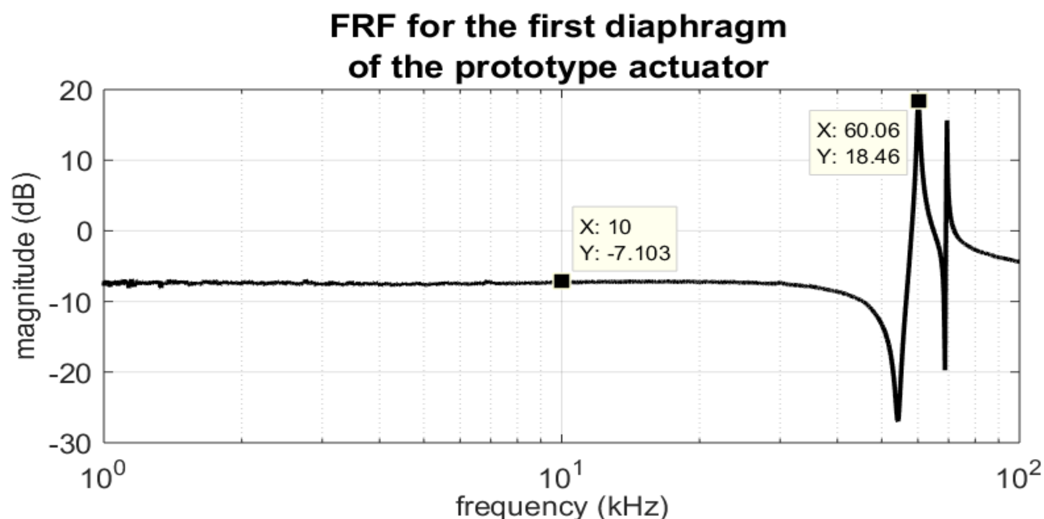

Figure 2-20: Frequency response function of the 2-G probe

2.3.3 Identification of the first natural frequency

The abnormally low first natural frequency is interpreted as follows. As shown in Figure 2-17 and Figure 2-18, the patterned gold layer serves not only as top electrodes, but also as wires

that transmit electrical signals. Since there is considerable area of gold on PZT layer in the "beam region" (refer to the box of dashed line in Figure 2-18 (b)), it is very likely that the beam mode has been activated. Since the cantilever beam is long and narrow (c.f. Figure 2-18), the first beam bending model would be much smaller than the diaphragm mode.

To prove this hypothesis, the following tests has been designed and performed. First, the FRF of another 2-G probe is measured using the same setup as in Figure 2-18 and Figure 2-19. After the FRF was measured, excessive epoxy is applied to the end of the probe cantilever as indicated by the red dashed line box shown in Figure 2-18(b). The FRF is then measured again. By comparing the natural frequencies before and after excessive epoxy is applied, one can determine the nature of the first mode.

The logic behind the above tests is as follows. If the first mode is diaphragm mode, the excessive epoxy applied to the end of the probe cantilever can barely alter the its natural frequency, since the stiffness of the diaphragm is not changed. However, if the first mode is beam bending mode, as the free length of the cantilever is shortened due to the excessive epoxy, the beam becomes much stiffer, producing a significantly higher first natural frequency. Figure 2-21 (a) and (b) shows the FRF of the 2-G probe before and after excessive epoxy is applied. The corresponding first natural frequencies are 50.07 kHz and 88.07 kHz. Obviously, the first natural frequency has been significantly increased, indicating beam bending mode as the first mode in Figure 2-20.

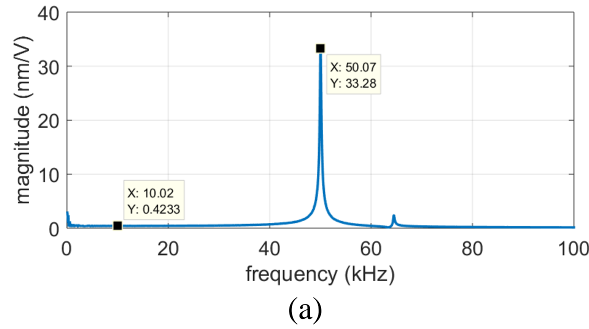

(a)

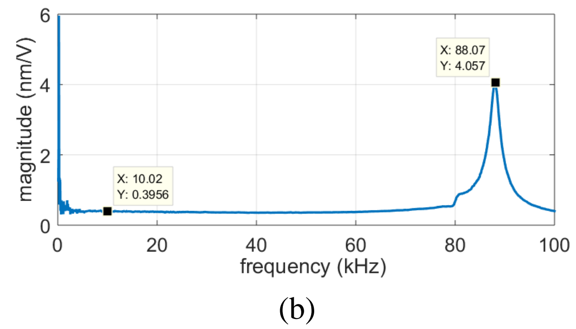

(b)

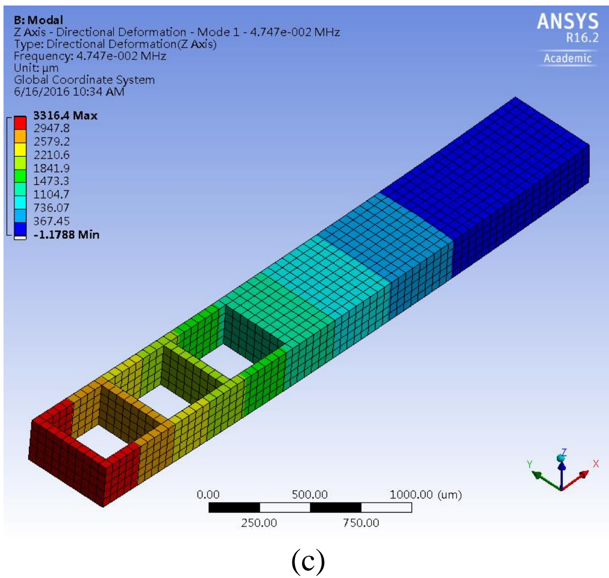

(c)

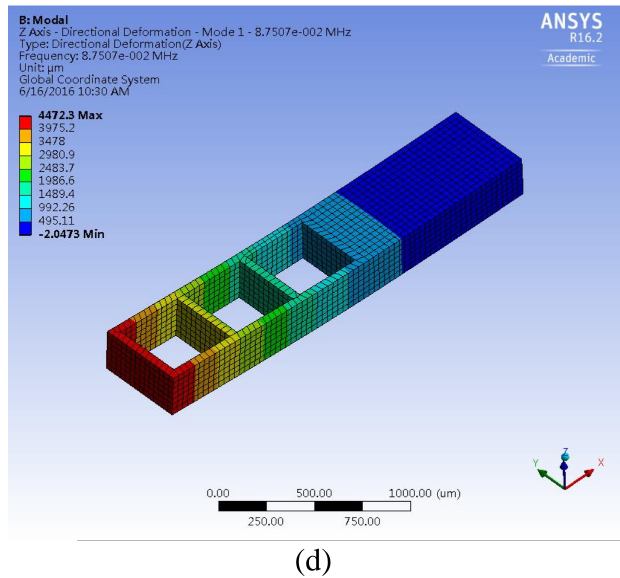

(d)

Figure 2-21: FRF and finite element modal analysis on a 2-G probe, before and after excessive epoxy is applied

(a) FRF before epoxy is applied; (b) FRF after epoxy is applied;

(c) modal analysis simulating a 2-G probe cantilever before excessive epoxy is applied;

(d) modal analysis simulating a 2-G probe cantilever after excessive epoxy is applied

The above conclusion can be further solidified quantitatively via finite element simulations. The length of the cantilever probe before and after epoxy is applied is first measured (3.5 mm and 2.5 mm) and input into the finite element models shown in Figure 2-21 (c) and (d). Notice that only the silicon beam part has been modeled since the diaphragm barely influences the beam bending mode. By assigning "fully clamped" boundary condition at the end of the

beam, modal analysis shows that the first natural frequencies before and after epoxy is applied are 47.47 kHz and 87.51 kHz respectively. This is quite close to the measured results (i.e., 50.07 kHz and 88.07 kHz), showing again the first mode is beam bending mode.

2.3.4 Identification of the low frequency FRF

Section 2.3.3 has proved that the first natural frequency of the 2-G probe corresponds to beam bending mode. Usually, this means the static gain is also dominated by beam bending mode. However, in our case, it is proved by experiments that most of the static gain comes from diaphragm mode.

As shown in Figure 2-17, two FRFs are measured by the LDV while focusing on point “A” and “B” respectively. Here, point “A” is at the center of the third diaphragm and point “B” is at the outer electrode near the cantilever structure. The logics is as follows. On one hand, point “A” is located at a residual silicon free area and is theoretically the point of maximum deflection in the diaphragm mode, while point “B” is located at an area where thick residual silicon exists, of which the diaphragm mode deflection can be ignored. On the other hand, point “A” and “B” are close enough so that one can approximately assume that they share the same amount of deflection in the beam bending mode. In other words, the deflection of point “A” is a superposition of diaphragm mode and beam bending mode, while the deflection of point “B” is mostly from the beam bending mode. If the magnitude of FRF at point “A” and “B” are similar, the first mode would be beam bending mode. If the magnitude of FRF at point “A” is much larger than point “B”, the first mode would be diaphragm mode.

The measured results of the two FRFs are shown in Figure 2-22. The static gain at point “A” is 0.41 nm/V (i.e., -7.732 dB) while the static gain at point “B” is only 0.034 nm/V (i.e.,

−29.33 dB). It is very clear that the static gain of the FRF as in Figure 2-20 still represents the deflection of the diaphragm.

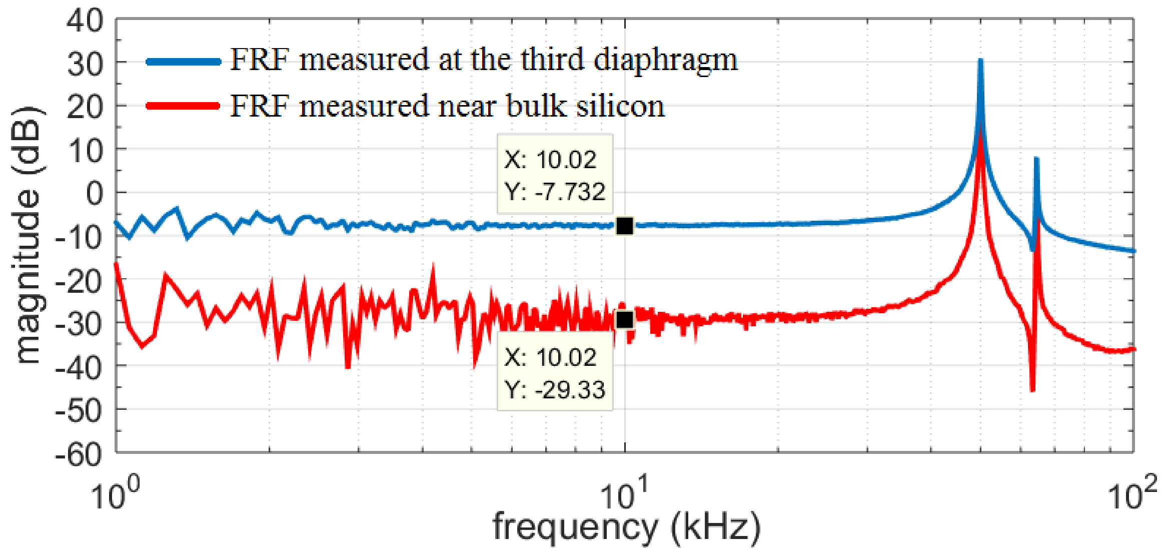

Figure 2-22. Frequency response function measured at different positions of the diaphragm

2.3.5 Interpretation of the static gain

Although the low 1st natural frequency and the source of the static gain has been identified by experiments and FE simulations, one still needs to interpret the abnormally small static gain of the 2-G probe diaphragm.

To investigate this issue, the backside cavity after fabrication is closely examined. It is found that the diaphragms are either over etched or under etched. Properly etched condition is rarely seen. Figure 2-23 (a) represents a special case that one of the diaphragms (the one lower in the picture) is properly etched. The blue and purple area at the center indicates that the wafer silicon is thoroughly etched, as the front side silicon oxide is exposed. Besides, there is a clear elliptic boundary for the exposed silicon oxide area. Outside of the ellipse, the area is grey and

black, showing the residual silicon. Measured from the picture. the residual silicon is 110 μm in lateral direction and 130 μm in longitudinal direction, much larger than what is assumed in the finite element model in Figure 2-4. Which results in a significantly stiffened diaphragm.

Furthermore, as we have just mentioned, properly etched condition is special and rarely seen among diaphragms. The probes survived from the double side etching and the releasing are most commonly seen in under etched conditions as shown in Figure 2-23 (b). With unetched silicon layer underneath the diaphragm, the stiffness is further enlarged.

The formation of the residual silicon and the unetched silicon layer is as follows. The backside etching is performed in an area of only 400 μm × 550 μm, while the etching depth is as large as 250 μm. Such small area but large depth will inevitably introduce bias in etching rates in different areas of the cavity. Typically, the etching is faster in central areas than in boundary areas since the large aspect ratio makes the etching ions more difficult to reach the boundaries. Such non-uniformity accumulates throughout the whole etching process. As a result, when silicon in the central area is eliminated, there is still considerable amount of silicon near the boundaries, forming residual silicon.

The etching is neither uniform for a single cavity nor for different cavities. This is caused by limitations of the DRIE equipment. Namely, the etching rates are slightly different throughout the reaction chamber. As a result, while some diaphragms are still covered by a layer of unetched silicon, the other diaphragms have already been etched through (c.f. the upper diaphragm of Figure 2-23(a)). Obviously, the broken diaphragms cannot be measured, and the only measurable probes are the under etched ones. Notice that we cannot measure the properly etched diaphragm in Figure 2-23(a) either because the upper diaphragm is broken, which will cause short circuit.

Although special methods can be applied to improve the etching uniformity (e.g. by redesigning the probe layout, refer to section 2.4.2), one can never eliminate the residual silicon or the unetched silicon layer because the etching non-uniformity is from the equipment, which always exists in practice, especially for such large depth and small cavity. The size of the residual silicon is clearly shown in Figure 2-23(a). To roughly estimate the average thickness of the unetched silicon layer, we refer to the manual of the DRIE machine that the etching rate against silicon is typically 4 μm. Since 2 min of DRIE is performed for each cycle at the very end of etching, it is reasonable to estimate the thickness of the unetched silicon to be $4-8$ μm.

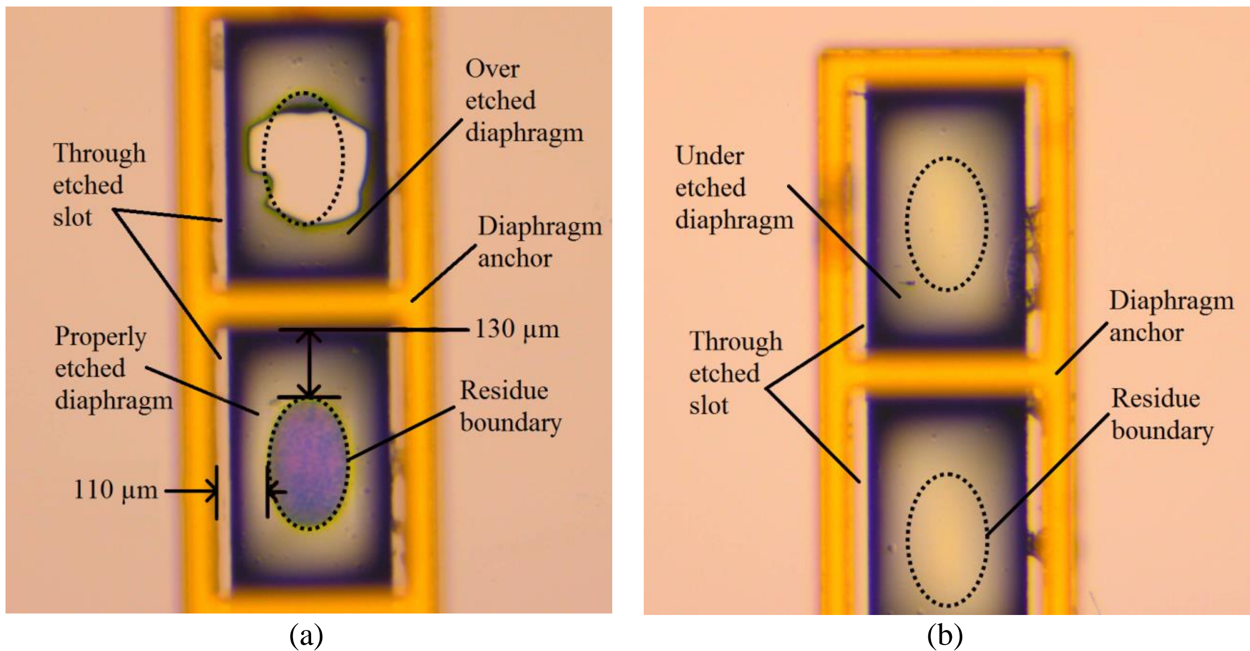

(a) (b)

Figure 2-23. Bask side view of the probe tip after DRIE, showing two diaphragms (a) one over etched and one properly etched; (b) both under etched

To quantitatively evaluate the influence of the above two factors, the partially released finite element model in Figure 2-4 is modified. As shown in Figure 2-24(a), the residual silicon accepts the same size as in Figure 2-23 (a), and the thickness of the unetched silicon layer is

assumed to be 4 μm (not shown in picture). Static analysis is simulated again using the same boundary conditions and driving conditions. As expected, the static gain drastically decreases from 12.62 nm/V to 1.31 nm/V. This is fairly close to the measured static gain of 0.44 nm/V, considering that the thickness of the unetched silicon is roughly $4-8$ μm and we have only modeled 4 μm.

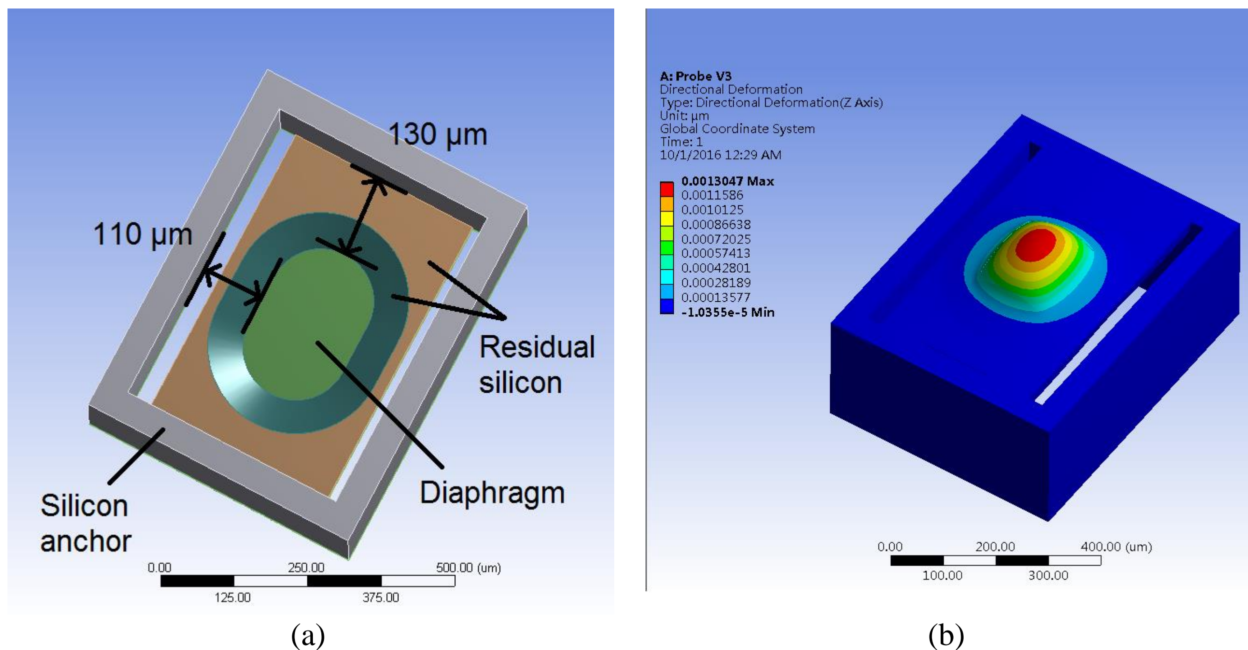

(a) (b)

Figure 2-24. Finite element model of the partially released actuator with modified residual silicon and unetched silicon layer
(a) backside view of the model; (b) the static structural analysis

2.3.6 Further discussions

From the characterization study, we can draw three conclusions. First, the unetched silicon layer and the residual silicon may significantly influence the diaphragm rigidity and lower the static gain. Therefore, before another batch of 2-G probe is fabricated, optimizations

must be done to improve the etching uniformity. Second, it has been demonstrated by multiple experimental tests that the finite element model is reliable and gives quite accurate predictions. Finally, since the predictions of the finite element model is accurate, that also means the original prediction in the design stage is also accurate. Therefore, the concept of enhancing the performance by partially releasing the diaphragm is feasible.

2.4 Parametric Study and Optimization

The experiments and discussions in section 2.3 proves that the small static gain of the 2-G probe is caused by enlarged residual silicon and unetched silicon layer. In this section, a series of parametric studies will be performed based on finite element analysis (c.f. Figure 2-24) to enhance the performance and provide guidelines for future re-designs. In particular, there are four parameters to be optimized. They are size of the diaphragm, thickness of the unetched silicon layer, width of the open slots and size of the top electrodes. Finally, based on the parametric study, an optimized design will be proposed and its performance will also be estimated by FE analysis.

2.4.1 Size of the diaphragm

As mentioned in Chapter 1, the design requirement for the 2-G PZT actuator is less than 700 μm in width. Therefore, we can slightly increase the total width. There are two major advantages. First, the bending rigidity of a partially released diaphragm will drop as the size becomes larger (while keeping the same thickness). Second, residual silicon may also be reduced since the etching becomes more uniform. Therefore, in the later parametric studies, a finite

element actuator model of 700 μm in width will be utilized. A schematic view is shown in Figure 2-30. In particular, the size of the residual silicon is modeled based on the following guidelines. The residual silicon size for a full-scale diaphragm (i.e., 800 μm by 800 μm) is 75 μm in both longitudinal and lateral directions. When the diaphragm is shrunk to 400 μm by 450 μm, the residual silicon size becomes 130 μm (longitudinal) and 110 μm (lateral). If we assume linear relation, for a 700 μm actuator, the residual silicon is roughly 120 μm (longitudinal) by 100 μm (lateral).

In addition to enlarging the overall size, the length of the diaphragm can also be specially modified. As mentioned in Chapter 1, since the diaphragm is released in lateral direction, increasing the length may also reduce the bending rigidity and enhance the static gain. This phenomenon is demonstrated by FE simulations in Figure 2-28. As the total length of the diaphragm increases from 750 μm to 1050 μm, one can clearly see the enhancement of static gain.

2.4.2 Thickness of the unetched silicon layer

The thickness of the unetched silicon layer influences the static gain by two major factors. First, it affects bending rigidity. It is obvious that a diaphragm with thicker unetched silicon layer will be more difficult to deform, and therefore has lower static gain. Second, the location of the PZT layer in the diaphragm may also influence the static gain. Because the out-of-plane deflection is induced by the in-plane strain of the PZT, the PZT layer must be placed off the neutral plane of the diaphragm to produce bending moment. (Theoretically, if the PZT layer lies exactly at the neutral plane, the diaphragm will not be able to deflect.)

To study this problem, the FE simulations are designed as follows. While keeping all the other parameters unchanged, the unetched silicon layer is gradually increased in thickness from 0.1 μm to 10 μm. The corresponding static gains are then evaluated. As shown in Figure 2-25, the static gain increases and reaches maximum of 5.9 nm/V at thickness 0.4 μm, then starts to decline. The results given by the finite element model are interpreted as follows. From 0 to 0.4 μm, as the thickness of the unetched silicon increases, the plane of the PZT layer moves farther apart from the neutral plane, which increases the bending moment. For smaller thickness, this factor dominates over the bending rigidity, and we see a sharp increase in static gain. As the thickness becomes larger than 0.4 μm, the increase in bending rigidity becomes more obvious and dominates over the effect of neutral plane, which causes the static gain to drop. From the parametric study, we come to two conclusions.

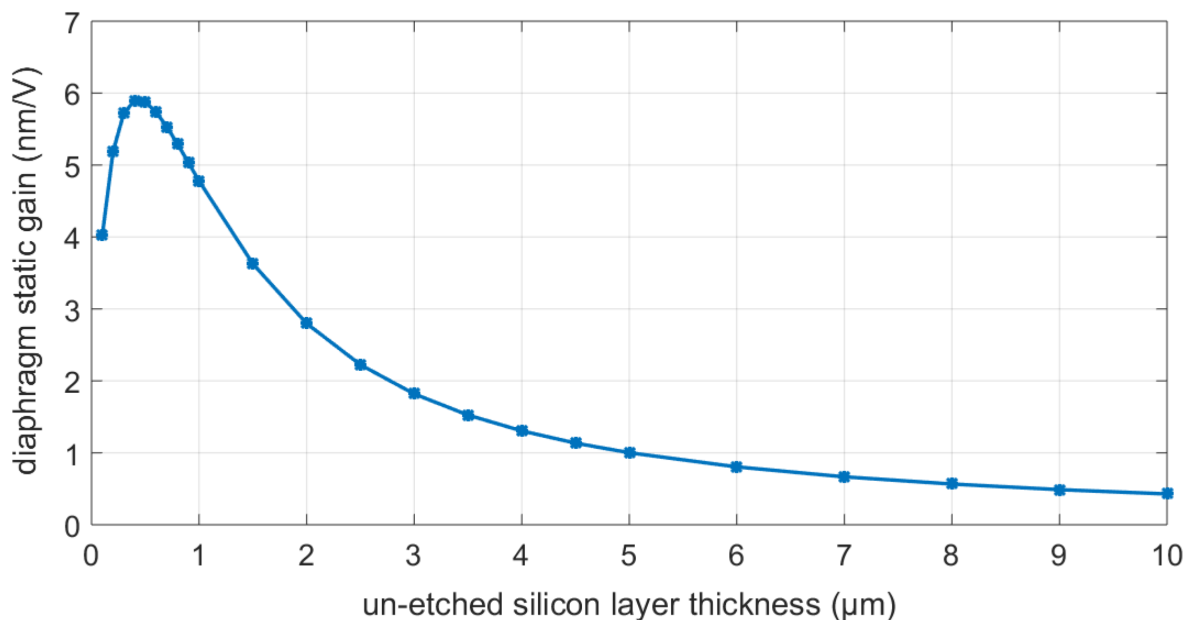

Figure 2-25. Diaphragm static gain with respect to the unetched silicon layer thickness

First, it is not necessary to totally eliminate the unetched silicon. At $0 - 0.4$ μm, thicker unetched silicon will move the neutral plane farther apart from the PZT plane, producing larger bending moment and static gain.

Second, it is shown in Figure 2-25 that the static gain is sensitive to the unetched silicon thickness in the range from 0 to 2 μm. On one hand, this explains why the probes from the same batch can have vastly different performance. (Because a slight difference in unetched silicon thickness can cause significant change in static gain.) On the other hand, it raises high requirements for uniformity in DRIE. Although the etching uniformity depends on equipment, it can still be improved if one chooses a proper layout configuration.

As previously shown in Figure 2-8, the 2-G probe utilizes a square layout so that the pattern boundaries follow the intrinsic <1-0-0> orientation of the silicon substrate. However, a comparison between 1-G probes and 2-G probes reveal that the square layout may cause the etching to become non-uniform. For previous fabrication of the 1-G probes, radial layout is utilized (c.f. Figure 2-8 (a)). Because the layout is radial symmetric, one can improve the etching uniformity by constantly rotating the substrate. Besides, since the chamber of the DRIE equipment adopts a cylindrical shape, the etching rate should be similar at locations with same radial distances from the center. As a result, the etching for the 1-G probes are much more uniform. Therefore, it is necessary to place the diaphragms radial symmetrically to ensure etching uniformity.

It turns out that the two design criteria (i.e., probe boundaries along <1-0-0> orientations and diaphragms placed radial symmetrically) can be satisfied at the same time. As shown in Figure 2-26, the probe boundaries still follow the <1-0-0> orientation, but instead of a square layout, the probes are placed slightly off each other so that the centers of diaphragms now have

same distance to the center of substrate. Such layout design may improve the etching uniformity significantly.

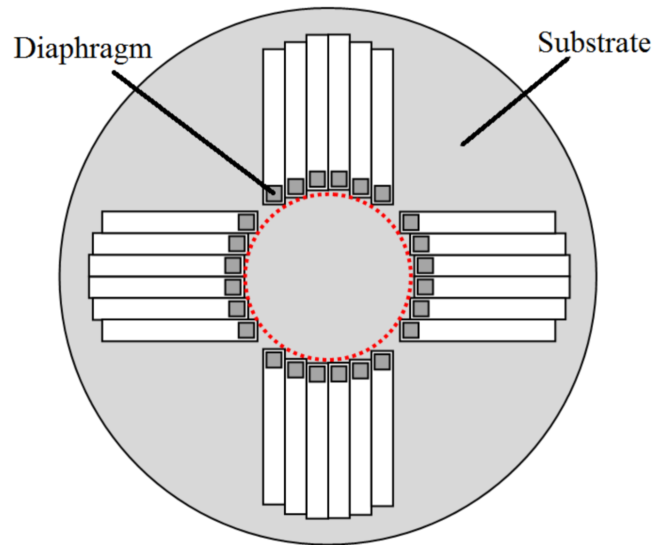

Figure 2-26. The combination of square layout and radial layout

In addition to the combined layout as shown in Figure 2-26, precise control of the backside etching can be achieved if one accepts the strategy in "Part 11" (backside DRIE) of Appendix A. Namely, the DRIE etching is combined with special taping and securing techniques, so that properly etched probes can be separately in advance, which may prevent over-etching and significantly improve the etching uniformity.

2.4.3 Width of the open slots

The fabrication of partially released diaphragm requires through etching two open slots at the sides of the diaphragm in lateral direction. The through etching will not only eliminate the

targeted silicon diaphragm, but also the residual silicon underneath it. Since the bending rigidity of diaphragm is largely determined by the size of residual silicon, the open slots may also influence the diaphragm bending rigidity by altering the residual silicon size.

Figure 2-27 depicts the configuration of the diaphragm backside, with Figure 2-27 (a) showing the bottom view and Figure 2-27 (b) showing the cross-sectional view. The diaphragm can be divided into three areas. Area “A” represents the central diaphragm area, which is free from residual silicon. The width of area “A” depends on the total width of the actuator. Area “B” represents the inclined residual silicon area. The thickness of the residual silicon in this area is assumed to linearly increase from 0.5 µm to 20 µm. The width of area “B” is 60 µm. Area “C” represents the flat residual silicon area. As discussed before, although the thickness of actual residual silicon will continue to increase, 20 µm of silicon is stiff enough to be considered as fully anchored. Figure 2-27(b) also shows the above three areas as a cross sectional view. The through etched open slot starts from the very right side in area “C”. The through etching will remain in area “C” if the slot width is less than 50 µm. For larger widths, the through etching may enter area “B” or area “A”.

When the width of the open slots is changed, there are two competing factors that affects the overall static gain. On one hand, as more residual silicon is removed, the bending rigidity is decreased, producing larger static gain. On the other hand, wider open slots also mean narrower diaphragm, and therefore narrower top electrodes. Since the out-of-plane deflection is caused by the in-plane strain of PZT when electric voltage is applied, reducing the electrode area may cause smaller actuation force, producing smaller static gain.

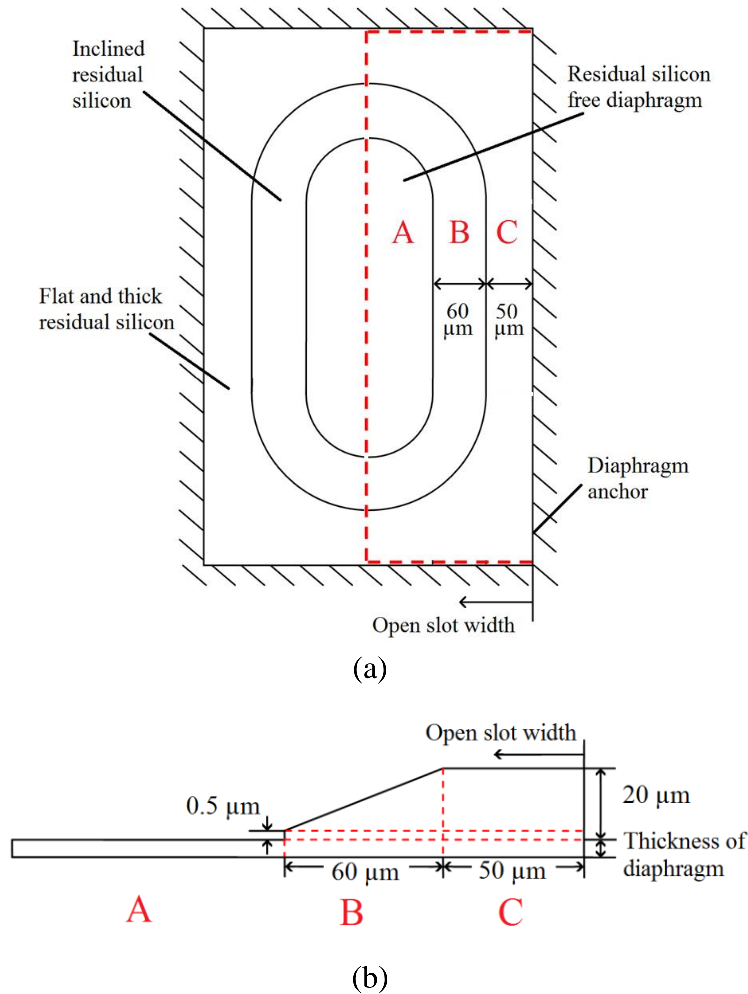

Figure 2-27. The schematic illustration of the backside diaphragm with residual silicon (a) bottom view; (b) cross sectional view.

We again refer to finite element simulations to do parametric analysis. As shown in Figure 2-28, the width of the diaphragm is set to be 700 µm. For each diaphragm length, the open slots width is gradually increased (so as the top electrode). The detailed interpretations are as follows.

For narrow open slots, the etching is within region “C” (c.f. Figure 2-27(b)). Since region “C” is very rigid, the diaphragm can be considered as fully clamped. Therefore, the slight increase in static gain is from the bending rigidity reduction due to a narrower diaphragm. When

the etching reaches region “B”, the thickness of the residual silicon also decreases, which significantly decreases the bending rigidity. Therefore, we see a clear increase in static gain from 50 µm to 70 µm. However, as discussed above, the electrode size is a competing factor. When the open slots are narrow, the electrode is relatively large, and its effect is not shown. However, as we continue to increase the width of the open slots, the electrode becomes narrow and the corresponding actuation declines significantly. As one can see in the figure, the two competing factors balances at open slot width of 70 µm to 80 µm, producing relatively steady static gain. Then the electrode size effect dominates, and the static gain is reduced. However, this trend does not persist. As the open slot width enters the region of 100 µm to 110 µm, the residual silicon thickness becomes so small that further etching may significantly change the bending rigidity. Therefore, we see a sharp increase in static gain. Notice that the overall maximum static gain is reached at 110 µm, for which the residual silicon is eliminated. After 110 µm, the rigidity changes become minor, and the static gain decreases again due to the size reduction of the electrodes.

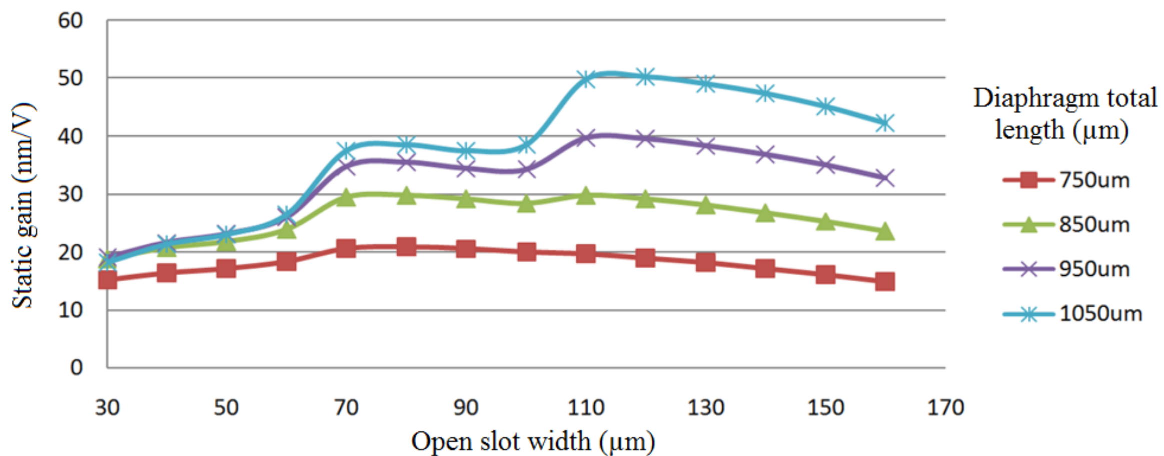

Figure 2-28: Parametric study of the diaphragm static gain with respect to diaphragm total length and open slot width

2.4.4 Size of the top electrodes

Previous literature about the fully anchored actuator studies the relationship between the electrode size and the diaphragm static gain [27]. The concept can also be applied in our case. Thus, the electrode size can be optimized to improve the driving efficiency and maximize the static gain.

In our case, the diaphragm is partially released, therefore electrode with larger width will simply produce more out-of-plane deflection. However, in the length direction, the diaphragm behavior follows the theory described by [27]. Namely, the static gain first increases as the electrode is enlarged. However, as the electrode enters the residual silicon area, because the bending effect happens at the boundaries of the diaphragm but residual silicon barely deforms, the static gain may decrease.

Figure 2-29 shows the static gain of the diaphragm for different electrode lengths with each line representing a specific diaphragm size. The width of the open slot is assumed to be 100 μm. For each curve, the static gain first increases and reaches its maximum depending on different diaphragm sizes. Then the static gain drops due to the residual silicon. The simulation results agree with our theory. Maximum static gains are obtained at 360 μm, 400 μm, 460 μm and 520 μm, for diaphragms of 750 μm, 850 μm, 950 μm and 1050 μm in length respectively.

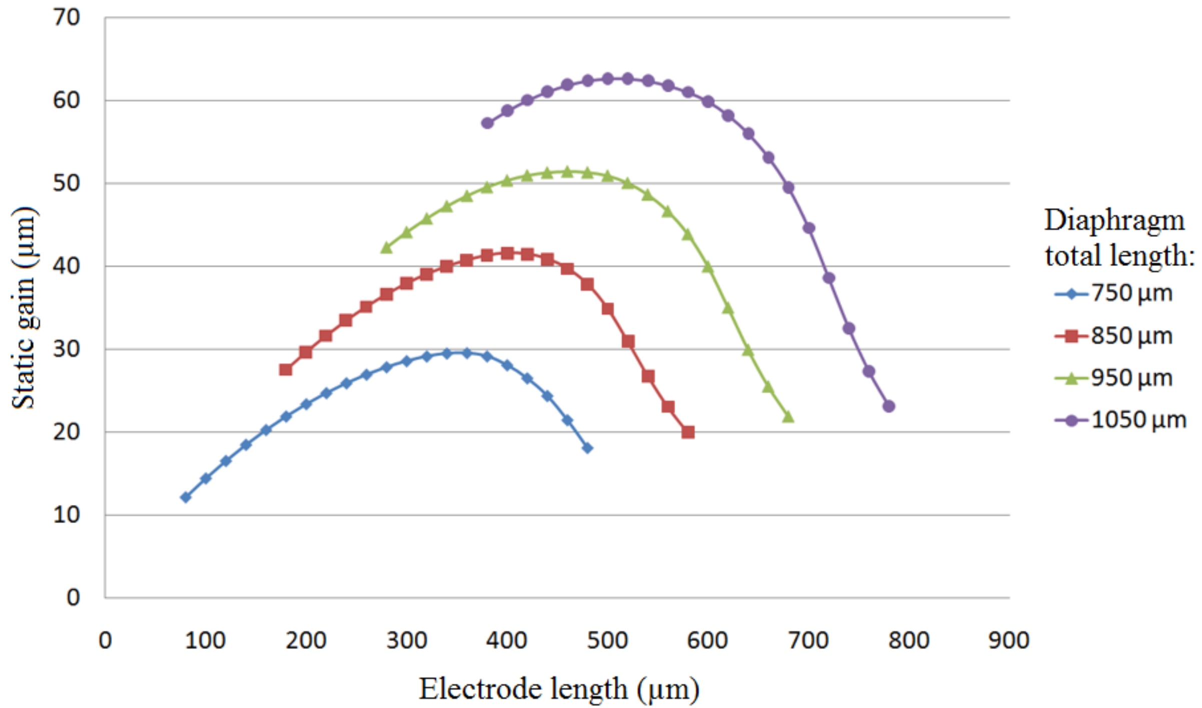

Figure 2-29: Parametric study of the static gain with respect to the length of electrode

2.4.5 The optimized model

An optimized model is proposed in Figure 2-30 with following parameters. The width of the actuator is 700 µm and the dimensions of the open slot is 750 µm by 80 µm (c.f. Figure 2-30(a)), for which the residual silicon on two sides is mostly eliminated (c.f. Figure 2-30(b)). For the electrode, the maximum allowed width is utilized, and the length is chosen to be 360 µm. Assuming one can obtain ideally etched condition so that the unetched silicon is exactly 0.4 µm, the static gain is estimated to be 29.96 nm/V, which is significantly improved compared with the fabricated 2-G probe (refer to section 2.3.2), and is even larger than the full size model (18.22 nm/V, refer to Figure 2-1). Modal analysis is also performed for the optimized model. The first natural frequency is 39.25 kHz, which shows large enough bandwidth.

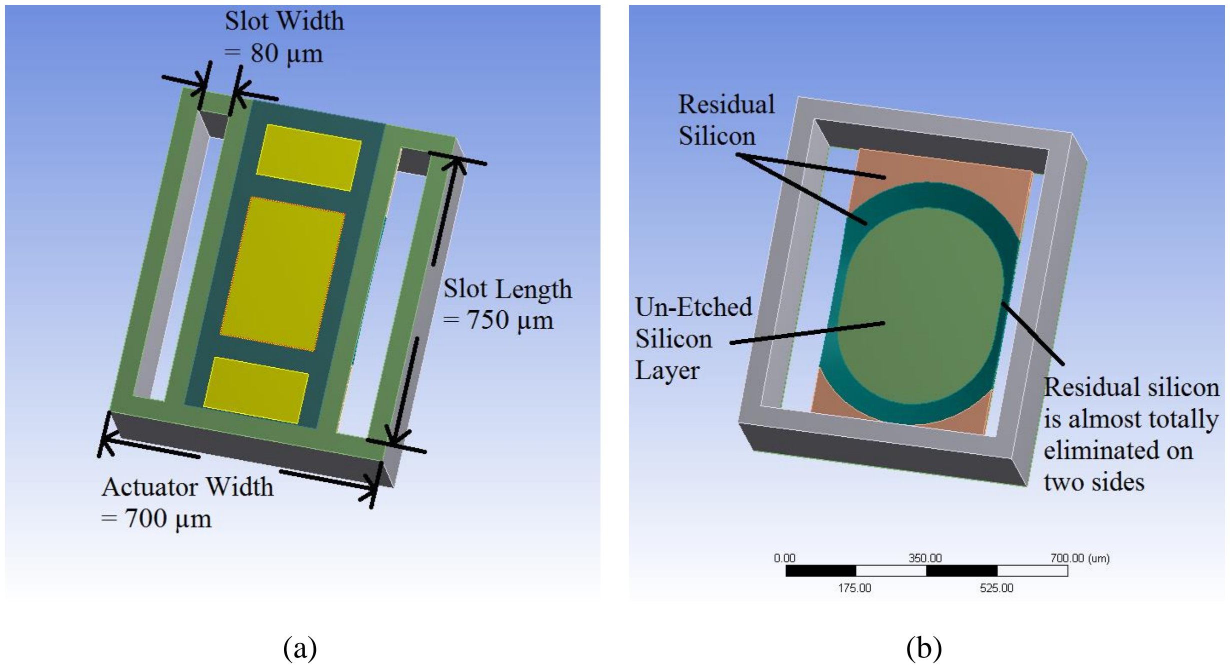

(a) (b)

Figure 2-30: The optimized model of partially released diaphragm actuator
(a) the front side view; (b) the backside view

Chapter 3. STUDY OF RELIABILITY

To determine reliability, long-term behavior and failure mechanism of the intra-cochlear PZT micro-actuator, a series of in vitro long-term tests are performed based on the 1-G probe model. There are three reasons of not using the newly developed 2nd generation. First, from structural point of view, the fully anchored structure of 1-G probe is much simpler compared with the partially released structure of the 2nd generation. Such simplicity is desirable in the initial reliability study. Second, in order to test the 2-G probes in fluid environment, an encapsulation layer must be coated to prevent short circuit. This adds unnecessary complications and uncertainties to the reliability tests, while the encapsulation problem has already been solved for the 1-G probe (by using a layer of parylene).

This chapter shows details of the reliability study on the fully anchored diaphragms of the 1-G probes. In particular, we have tested mechanical and electrical behaviors in both air and artificial perilymph [29]. The in-air tests show reliable behavior, while sample probes driven in artificial perilymph fails after a certain amount of time. The failure mechanism is then researched based on the mechanical FRF and electrical impedance information, and we conclude by a demonstration test that the malfunction of the PZT diaphragm is caused by electrical short circuit triggered by failure of the parylene encapsulation layer. Finally, potential solutions to improve the encapsulation are proposed. It is also pointed out that the parameter of impedance can serve as an indicator for integrity of probes service in vivo conditions.

3.1 SETUP OF RELIABILITY TESTS

The two major categories of data to be extracted from the reliability tests are mechanical FRF and electrical impedance. Therefore, the setup of reliability tests can be divided into three main parts, i.e., the sample setup, the experimental setup and electrical model setup. They are shown in details as follows.

3.1.1 Sample setup

The sample setup for in-air tests is straightforward. We adopt similar sample setup as in Figure 2-18 that the end of the 1-G probe is fixed by epoxy to create a cantilever structure. The setup in artificial perilymph is more challenging. As discussed above, the probe must be properly encapsulated to avoid short circuit. Besides, there are two additional problems existing for long-term tests. On one hand, artificial perilymph, mostly consists of water, may evaporate and be contaminated during the long testing period. Therefore, the sample must be sealed. On the other hand, in order for the LDV measurements to gain desirable accuracy, the sealing must have minimal interference with the laser beam.

The adopted sample setup design is shown in Figure 3-1 (a). Namely, a glass bottom petri dish is utilized to seal the probe and the artificial perilymph. The probe is first glued to the cap by epoxy with the diaphragm side facing the thin glass on the cap. The petri dish is then closed and permanently sealed by epoxy. Two small holes are especially drilled in advance. One hole is located at the side of the cap for the wires to route through. It is then sealed with epoxy. The other hole is located at the top of the cap for artificial perilymph to fill in. Because one needs to collect the artificial perilymph later after reliability tests (for the lead leaching tests), the top

drilled hole is temporarily sealed by tape. By adopting the above sample setup, one can effectively avoid evaporation and contamination. Furthermore, since the glass on the cap is only 0.16 – 0.19 nm thick, its interference with the laser beam is negligible.

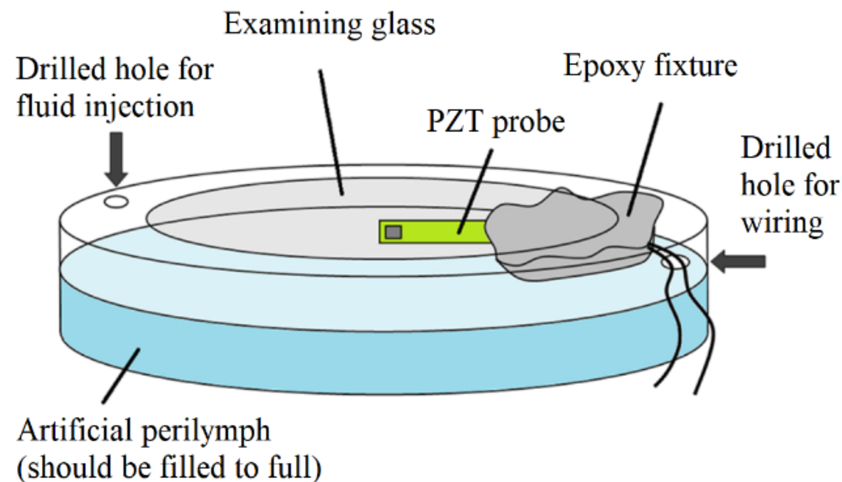

Figure 3-1: Sample setup for reliability tests in artificial perilymph

3.1.2 Experimental setup

The experimental setup measures both FRF and electrical impedance. The setup for mechanical FRF measurements is similar as in Figure 2-19, except that the sample is now replaced by the sealed peri dish described in the above section. Again, the driving voltage is 1 V across the PZT diaphragm and the driving frequency is kept at 10 kHz for the long-term driving. To obtain FRF of the diaphragm, the input signal is temporarily changed to a swept sine signal from 100 Hz to 102.4 kHz. Again, the static gain is extracted from each FRF, which shows the mechanical integrity of the PZT diaphragm. After each measurement, the driving frequency is quickly changed back to 10 kHz. The impedance is monitored at the same time. Namely, the

wires of the testing sample are quickly connected to an impedance analyzer to obtain its electrical impedance. Especially, the impedance magnitude and phase angle are measured as a function of input frequencies. Information such as the parallel resistance of the PZT diaphragm is then extracted from an electrical model described below in section 3.1.3. Those derived parameters determine the electrical integrity of the PZT diaphragm.

3.1.3 Electrical model setup

In order to interpret the impedance of the diaphragm during reliability tests. The following electrical model is established. As shown in Figure 3-2 (a), the diaphragm is modeled as a capacitor (C_p) and a resistor (R_p) in parallel, while the wirings are modeled as a small resistor (R_s) and a parasitic inductor (L_s) in series. Here we specifically include the resistor R_p because the PZT material is not ideal insulator. In fact, the value of R_p largely determines the electrical integrity of the diaphragm. In case of electrical failure such as short circuit, the value of R_p will drop significantly.

The impedance of the electrical model is calculated as follows. First, by classical circuit theory, the impedance of the capacitor C_p is 1 / $j\omega C_p$, where ω is the driving frequency. In our case, we also consider the effect of heredity by introducing a factor α. Then the impedance of the diaphragm becomes 1 / $j\omega^\alpha C_p$. The concept of heredity also applies to the inductor L_s. By assuming the corresponding factor of heredity to be β, the impedance of the inductor is $j\omega^\beta L_s$. Finally, the overall impedance of the electrical model is,

$$Z = \frac{R_p}{1 + j\omega^\alpha C_p R_p} + R_s + j\omega^\beta L_s \quad \text{Eqn. 1}$$

There are in total six parameters in the above expression (i.e., C_p, R_p, R_s, L_s, α and β). Those parameters are assumed to be constant and may be extracted from the measured impedance. The following of this section shows how to extract those parameters by referring to an example.

A typical impedance magnitude curve as a function of frequency is shown in Figure 3-2 (b) (impedance curve of actuator driving in air). First off, the curve clearly shows a corner frequency located between 10^7 to 10^8 rad/s. For frequencies much smaller than the corner frequency, the impedance magnitude is dominated by the capacitor, showing a descending straight line. By the electrical model, the slope of the descending line is -20α dB/decade. Therefore, one can first extract the value of α by measuring the slope of the impedance magnitude curve in the low frequency region. Similar techniques can be applied to determine the value of β. Namely, for frequencies much larger than the corner frequency, the inductor becomes dominant, showing an ascending straight line of slope $+20\beta$ dB/decade. Thus, one may extract the value of β by measuring the slope of the impedance magnitude curve in the high frequency region.

The values of C_p and R_p can be determined in the following way. From Eqn. 1, the impedance magnitude in low frequency region is,

$$|Z| = \frac{R_p}{\sqrt{1 + (\omega^\alpha C_p R_p)^2}} \quad \text{Eqn. 2}$$

And the impedance angle θ satisfies,

$$\tan(-\theta) = \omega^\alpha C_p R_p \quad \text{Eqn. 3}$$

By substituting Eqn. 3 into Eqn. 2, one may obtain the value of R_p as,

$$R_p = |Z|\sqrt{1 + \tan^2\theta} \quad \text{Eqn. 4}$$

Once α and R_p are determined, the value of C_p can be easily extracted by using either Eqn. 2 or Eqn. 3.

The cutoff frequency of the low pass filter $Z_p = R_p/(1 + j\omega^{\alpha} C_p R_p)$ is located below the descending region (not shown in Figure 3-2(b)). Therefore, one can ignore the constant "1" in the denominator when evaluating near the corner frequency (i.e., at $10^7 - 10^8$ rad/s), and write impedance as,

$$Z = R_s + j\left(\omega^{\beta} L_s - \frac{1}{\omega^{\alpha} C_p}\right) \quad \text{Eqn. 5}$$

By circuit theory, the phase angle reaches zero at corner frequency. Thus, one can obtain the value of corner frequency ω_c by referring to the phase diagram, and then extract the value of L_s by solving,

$$\omega_c^{\beta} L_s - \frac{1}{\omega_c^{\alpha} C_p} = 0 \quad \text{Eqn. 6}$$

Moreover, the value of R_s is simply the impedance magnitude at the corner frequency,

$$R_s = |Z|_{min} = |Z(\omega_c)| \quad \text{Eqn. 7}$$

which can be easily extracted.

By the above electrical model and parameter extraction techniques, electrical parameters are obtained as, $\alpha = 0.995$, $\beta = 1.043$, $R_p = 66.8$ MΩ, $C_p = 4.93$ nF, $R_s = 7.4$ Ω and $L_s = 0.161$ μH respectively. Using those parameters, the impedance Z of the diaphragm is re-built by Eqn. 1 and plotted in red dashed line in Figure 3-2 (b). The fitting curve agrees extremely well with the measured data (i.e., the blue solid line).

We notice that the electrical model, especially the heredity factors (i.e., α and β) is not realistic. Thus, the true equivalent circuit for the actuator must be different from our electrical model. However, this model can still be applied for four reasons. First, the purpose of this

electrical model is not to interpret the equivalent circuit of the PZT micro-actuator, but to curve fit the measurement data and extract information for integrity monitoring. Second, although the model cannot be realized in practice, it is proved above that the curve fits well with the measurement data. Third, the level of R_p shows steady behavior during each stage, but acute drop during transitions between stages, which can effectively predict the integrity of the actuator. Fourth, compared with a more realistic model, the electrical model with heredity factors must be simpler. That means the algorithm is easier to establish and the resulting program is faster to execute, which is essential for real time monitoring.

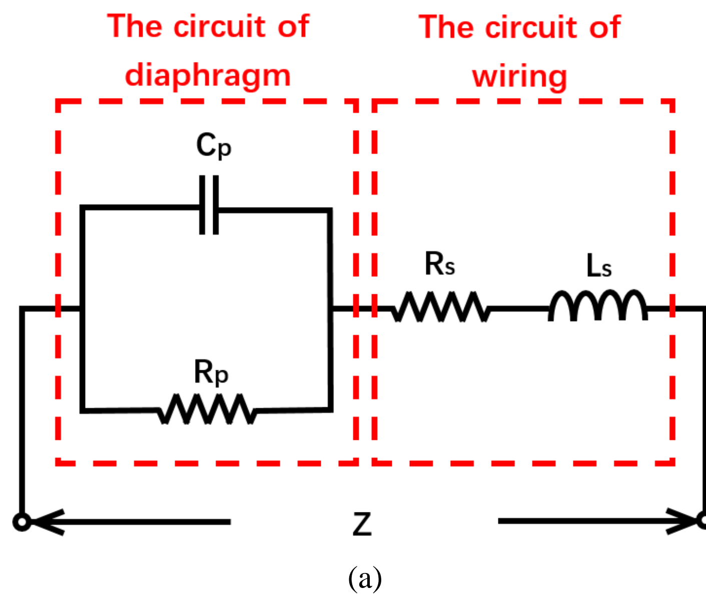

(a)

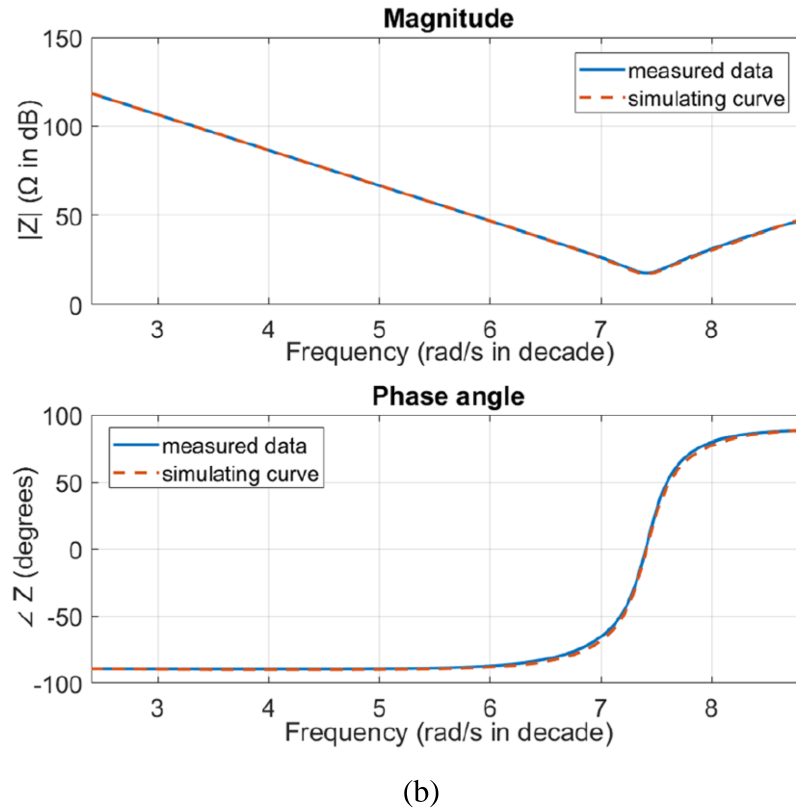

(b)

Figure 3-2. The electrical model for reliability test
(a) the electrical circuit for curve fitting;
(b) typical impedance data and fitting curve for diaphragm measured in air

3.2 IN-AIR RELIABILITY TESTS

Among all the long-term tests, the in-air reliability tests are performed first for two reasons. First, the in-air tests pre-eliminate the possibility of short circuit, since air is non-conductive. In other words, if the actuator malfunctions during the test, it is caused by mechanical reasons such as diaphragm fatigue or electrode delamination. Second, the service life in air also provides a reference. For example, in the later tests, if a diaphragm also fails mechanically in artificial perilymph after approximately same amount of time, then we can conclude that artificial perilymph environment plays a minor role in determining the service life.

The static gain as a function of time is shown in Figure 3-3 (a). After 848 hours (i.e., 35 days 8 hours), there is no sign of deterioration for the static gain of the diaphragm driven in air, indicating no structural failure happened during the driving period. There are three portions for the static gain curve in blue, red and green colors respectively, acquiring slightly different static gain at approximately 4.1 nm/V, 4.25 nm/V and 4.5 nm/V. This is because those curves correspond to different driving frequencies at 3 kHz, 16 kHz and 40 kHz respectively. The reason for switching to higher driving frequencies is to expedite the deterioration process. Figure 3-3 (b) shows a complete FRF during the driving process. The three frequencies of 3 kHz, 16 kHz and 40 kHz are all below the natural frequency at 60.49 kHz, obtaining similar static gain as in Figure 3-3 (a). In summary, the diaphragm has experienced 7.32×10^{10} cycles, which still shows reliable mechanical behavior. Therefore, structural failure such as diaphragm fatigue is not likely to happen.

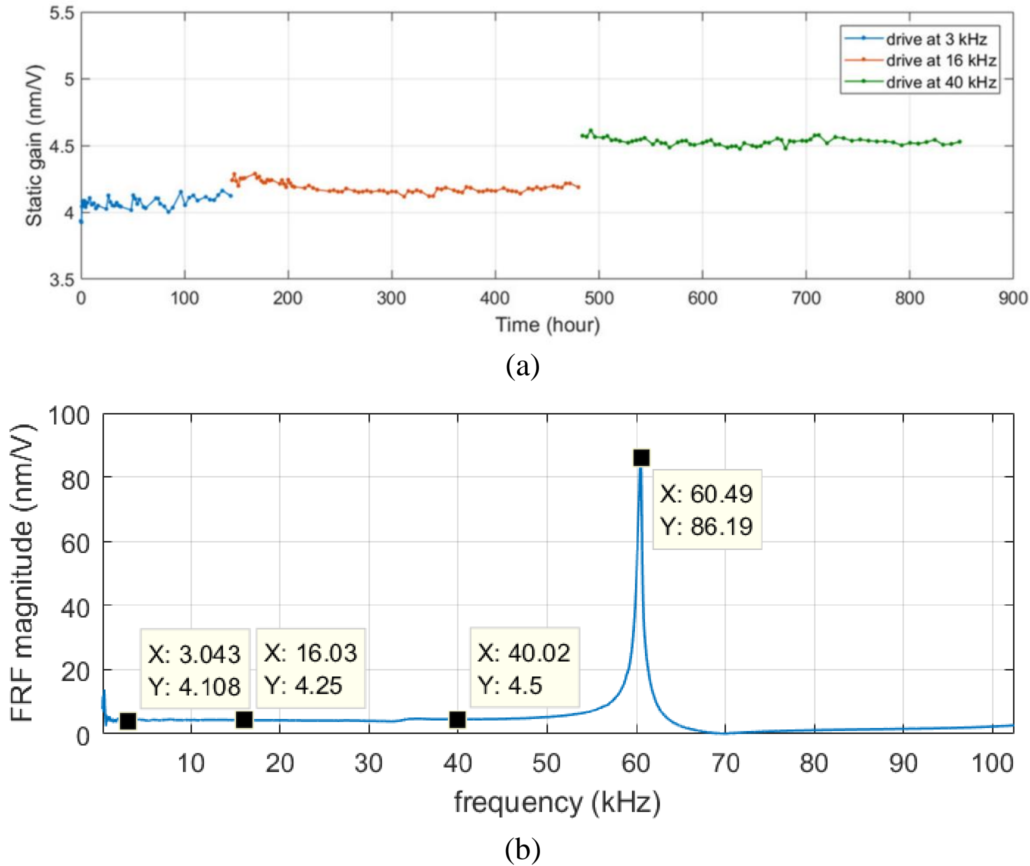

Figure 3-3: The mechanical behavior of the diaphragm driving in air
(a) the static gain as a function of time; (b) a typical frequency response function

In addition to the FRF measurement, the electrical impedance is also monitored. A typical impedance magnitude curve is previously shown in Figure 3-2 (b). The corresponding parameters are extracted using the electric model in section 3.1.3. Table 3-1 lists the parameters of C_p, R_p and α extracted before and after the reliability test. One can see that there is no significant change for those parameters, indicating stable electrical behavior. Furthermore, the parallel resistance R_p is in the order of MΩ, with almost no heredity (i.e., $\alpha \approx 1$). Therefore, the diaphragm is also electrically stable when driven in air.

Table 3-1. Extracted electrical parameters before and after reliability test in air

	C_p (nF)	R_p (MΩ)	α
Before test	4.93	66.81	0.995
After test	4.94	66.59	0.995

3.3 Soaking Test in Artificial Perilymph

The in-air test descried in section 3.2 exclusively investigates the possibility of structural failure, while short circuit is ignored. In this section, the possibility of short circuit will be researched in detail, while structural failure is eliminated by a simple soaking test. Namely, the diaphragm is submerged in artificial perilymph without voltage input. By doing this, the structural integrity of the diaphragm is ensured since it is not moving throughout the test. For consistency with the later long-term driving tests in artificial perilymph, we utilize the same sample setup as in Figure 3-1. The total time for the soaking test is 1365 hours (i.e., 56 days 21 hours).

Again, two sets of data are collected, i.e., static gain and electrical impedance. For static gain measurement, two curves are generated by measuring either the center top / bottom electrode pair or the outer top / bottom electrode pair. The results as a function of time is shown in Figure 3-4. Initially, the static gain quickly rises and is saturated around 100 – 150 hours, and then remains roughly a constant for the rest of the test. The curve fluctuations after 150 hours are caused by laser point drifts and focus point adjustments, because one must monitor the impedance at the same time. This is evidenced by the green static gain curve in Figure 3-7. Thus, when the laser dot and the focus is kept unchanged, the fluctuations in the static gain become rather small.

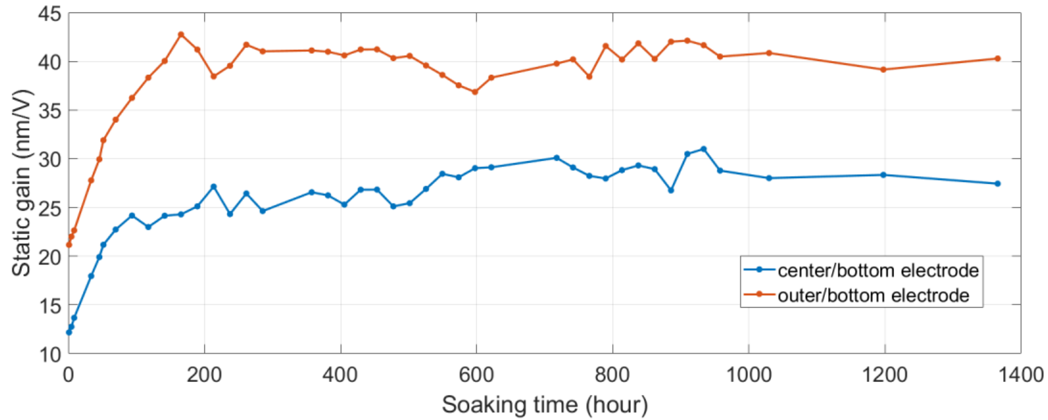

Figure 3-4: The static gain as a function of time for the PZT diaphragm soaked in artificial perilymph without driving

The static gain curve shows no sign of deterioration after 1365 hours soaking in artificial perilymph. However, the electrical impedance behaves rather differently. Figure 3-5 shows the extracted parameters of parallel resistance R_p (in solid lines) and heredity coefficient α (in dashed lines), while measuring either the center top / bottom electrode pair (in blue color) or the outer top / bottom electrode pair (in red color). Both the R_p and the α curves are clearly not constant throughout the soaking test. Instead, the values of R_p cascades into three stages. For each stage, the R_p level is relatively steady, until it reaches the end of stage and experiences an acute drop. Same phenomena exist for the heredity coefficient α as well, at approximately the same time. For the rest of this section, we will focus on explaining these three stages by interpreting data of the center top / bottom electrode pair (i.e., the blue colored curves), since the outer top / bottom electrode pair shows similar behaviors.

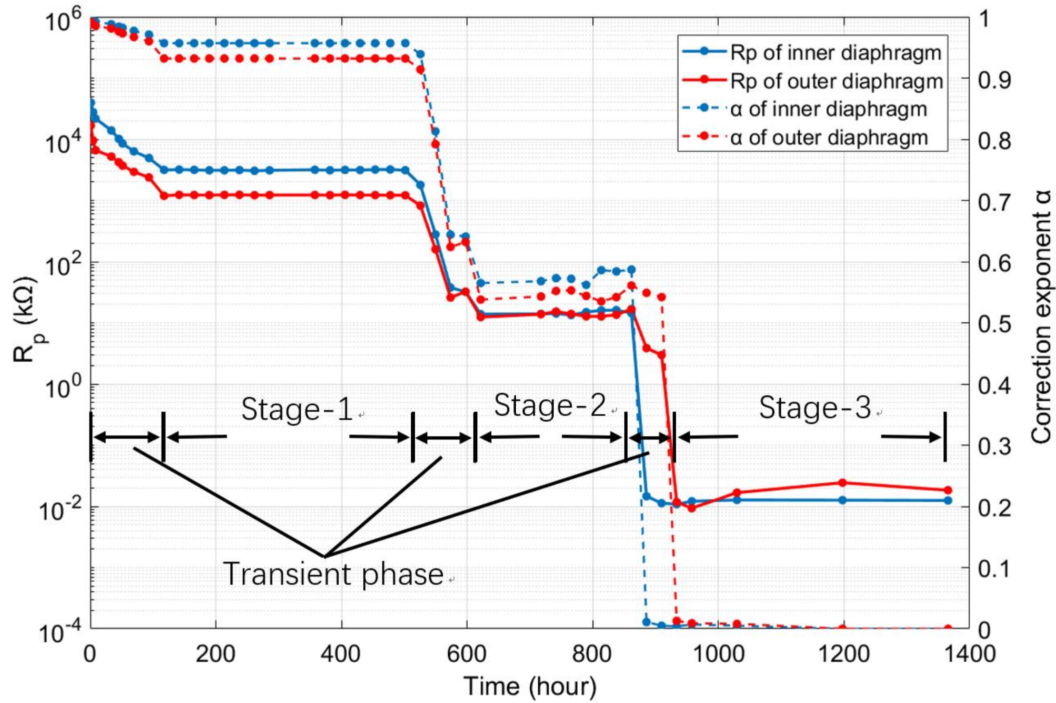

Figure 3-5: The parallel resistance R_p (solid lines) and the heredity coefficient α (dashed lines) of the PZT diaphragm as a function of time, measured by either center top / bottom electrode pair (in blue color) or outer top / bottom electrode pair (in red color)

3.3.1 Stage-1: Effective encapsulation

This stage refers to the time period until $500 - 550$ hours. For the first $100 - 150$ hours, the values of R_p drop from 39.6 MΩ to 3.16 MΩ. This phenomenon has been explained in previous literature by Chuan Luo [25]. Namely, the PZT layer is highly porous, and the submerge into conductive fluid such as artificial perilymph may significantly increase the equivalent dielectric constant of PZT, which in term reduces the parallel resistance R_p. Thus, despite the significant drop in R_p, the encapsulation by parylene is effective, since R_p is still in the MΩ level, showing very little conductivity. This can be further demonstrated by referring to the heredity coefficient α. The level of α only slightly drops from 0.994 to 0.957 (i.e., a 3.7% drop), indicating that the nature of the PZT diaphragm has not been changed throughout stage-1.

3.3.2 Stage-2: Encapsulation failure

After stage-1, the R_p level experiences an acute drop from 3.16 MΩ to 14.99 kΩ in 120 hours (thus, $500 - 620$ hours in Figure 3-5). At the same time, the heredity coefficient α also drops from 0.957 to 0.834 (i.e., a drop of 12.9%). Then both the R_p and the α level are stabilized for another $200 - 250$ hours.

For the failure mechanism in stage-2, we hypothesize that the parylene encapsulation layer is compromised, resulting in direct contact between the metal electrodes and the surrounding artificial perilymph. On one hand, such direct contact may short the circuit and change the nature of the PZT diaphragm, causing substantial drop to R_p and α. On the other hand, the electrical close loop created via the failure of parylene must go through the path of perilymph fluid near the diaphragm, resulting in a much lower but still considerably large level of R_p (at 14.99 kΩ).

To support the above hypothesis, we have designed a demonstration test as follows. A 1-G probe without parylene coating is submerged in the artificial perilymph. (We refer to this probe as "bare probe" for the rest of the dissertation.) The impedance of the bare probe is measured over time， and the parallel resistance R_p is extracted. Figure 3-6 shows the impedance information of such bare probe. In particular, Figure 3-6 (a) shows three impedance magnitude curves. The red curve represents the bare probe after R_p is stabilized. The blue and green curves represent the probe in soaking test during stage-1 and stage-2 respectively, which are also measured after R_p is stabilized. We see that diaphragm in stage-2 shows similar behavior to the bare probe, while their slopes are much less negative compared with that of the diaphragm at stage-1. Since the slope is proportional to the heredity coefficient α, the above phenomenon

indicates that the diaphragms of the probe at stage-2 in the soaking test and the bare probe in artificial perilymph have similar configurations.

Figure 3-6 (b) shows the parallel resistance R_p of the bare probe as a function of time. Namely, the value of R_p is 57.94 MΩ in air. When the bare probe is submerged in artificial perilymph, R_p immediately drops to 401.4 kΩ, followed by a relatively slow and steady decline until it finally stabilizes at 25 kΩ. Obviously, the sudden drop from 57.94 MΩ to 401.4 kΩ is due to the short circuit via perilymph, and the steady decline from 401.4 kΩ to 25 kΩ is likely caused by the gradual infiltration of artificial perilymph into the PZT pores [25]. The stabilized R_p of the bare probe (i.e., 25 kΩ) is similar to that of the soaking test (shown by a red dashed line in Figure 3-6 (b)). Both the impedance curve slope at low frequencies and the extracted R_p level validate our hypothesis that the drop of R_p is cause by the failure of the parylene encapsulation.

Finally, the failure of parylene encapsulation and the drop of R_p will not contradict with the steady behavior of the FRF (c.f. Figure 3-4). FRF is generated from the out-of-plane deflection of the PZT diaphragm, which is from the piezoelectric effect. A smaller R_p simply means a larger current is now required to sustain the voltage between the two electrodes.

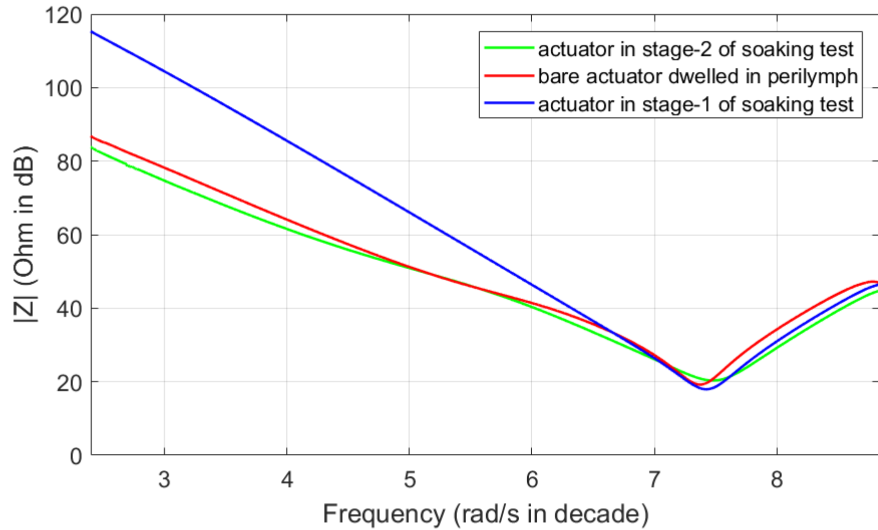

(a)

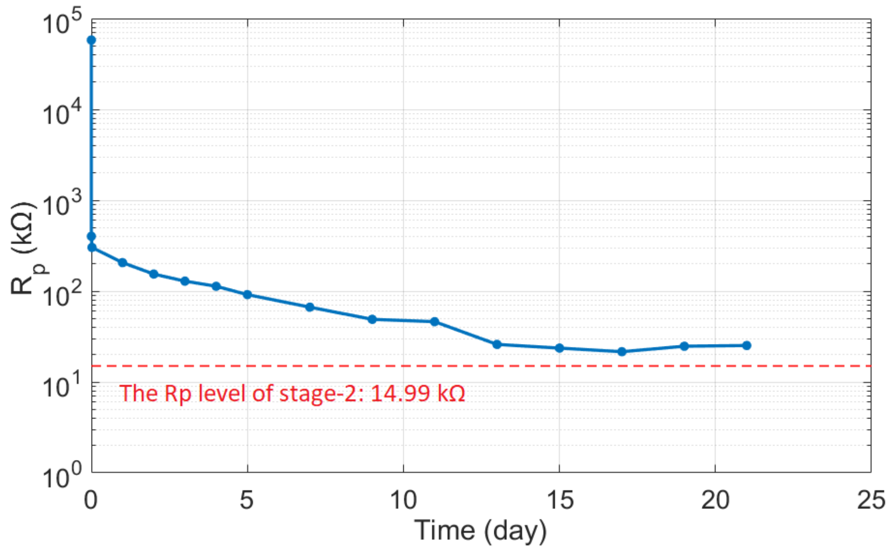

(b)

Figure 3-6: Impedance magnitude and extracted parallel resistance R_p of a bare actuator soaked in artificial perilymph, compared with the actuator diaphragm in stage-2 of the soaking test (a) the impedance magnitude; (b) the extracted parallel resistance R_p

3.3.3 Stage-3: Massive electrical leakage

After approximately 860 hours, the impedance and the value of R_p experiences another major drop from the previous kΩ level to $10 - 15\ \Omega$. The low level of R_p implies significant

current leakage into the surrounding artificial perilymph, which also means a much larger power consumption is required to sustain the FRF level in Figure 3-4. The microscopic mechanism in this stage is currently unknown.

From the soaking test, we can draw following conclusions. First, the parylene encapsulation initially provides good insulation. Second, the parylene encapsulation will be compromised after submerging in artificial perilymph for certain amount of time. Third, the electrical failure is not necessarily shown in the mechanical behavior of FRF. Fourth, the integrity of encapsulation can be monitored by referring to the extracted R_p level, which may serve as an ideal indicator of integrity in vivo conditions.

3.4 Long-term Driving Test in Artificial Perilymph

After the individual studies of possible structural failure by in-air tests and possible electrical failure by soaking tests, their combined effect is also researched by a series of complete long-term driving tests. Namely, the diaphragm and the experimental setup follow the configuration described in section 3.1.1 and 3.1.2. For the driving condition, a voltage of 1 V at 10 kHz is applied between the center top / bottom electrode pair.

For the long-term driving test in artificial perilymph, we choose to perform two complete sets of tests on two similar probes, both of which are coated with parylene. We called them probe-1 and probe-2 for the rest of this section. The reasons for using two probes (and doing two tests) are as follows. First, the FRF curves fluctuate for the previous soaking tests (c.f. Figure 3-4). It is hypothesized that the fluctuation mainly comes from frequent switching between the FRF and the impedance measurements. To prove this hypothesis, only the FRF data will be measured for probe-1, so that no switching is required. Moreover, it is also shown in the soaking

test that the impedance information is crucial in analyzing the failure mechanism. Therefore, for the test of probe-2, we choose to measure the same set of data as in the soaking test, i.e., both mechanical FRF and electrical impedance when driving either the center top / bottom electrode pair or the outer top / bottom electrode pair. Second, since two similar probes are tested under the same driving conditions, the repeatability of the reliability tests can be checked.

The mechanical FRF as a function of time is shown in Figure 3-7. The green curve represents the FRF of probe-1. As no switching is taken place during the whole test, the fluctuation is clearly attenuated. The FRF first rises to 40 nm/V in 70 hours and is stabilized for 800 hours. The FRF behavior up to this point is fairly similar to that of the soaking test. However, after 800 hours, the static gain experiences an acute drop to 15 nm/V for the next 200 hours. The FRF finally drops to 1 nm/V when the long-term driving test is ended at 1000 hours. Since such drastic drop in static gain is not seen in the previous in-air test or soaking test, it is most likely that a structural failure occurs during the driving process.

The long-term driving test on probe-2 is then performed, and the FRF results are also shown in Figure 3-7. The blue curve is the FRF using center top / bottom electrode pair and the red curve is the FRF using outer top / bottom electrode pair. For the blue curve using center top / bottom electrode pair, similar behavior is observed as probe-1. Namely, the FRF rises to 65 – 75 nm/V for the first 200 hours and is stabilized for another 600 hours. Then we see a sudden drop from 75 nm/V to 50 nm/V at 800 hours, which finally drops to 5 nm/V around 960 hours. Since the blue curve is obtained using the same driving and measuring configurations as probe-1, the long-term driving test is repeatable. However, the sudden drop in the static gain is not seen for the red curve when the outer top / bottom electrode pair is measured. The FRF rises to 16 – 23 nm/V for the first 70 hours and is stabilized until the end of the test (i.e., 960 hours).

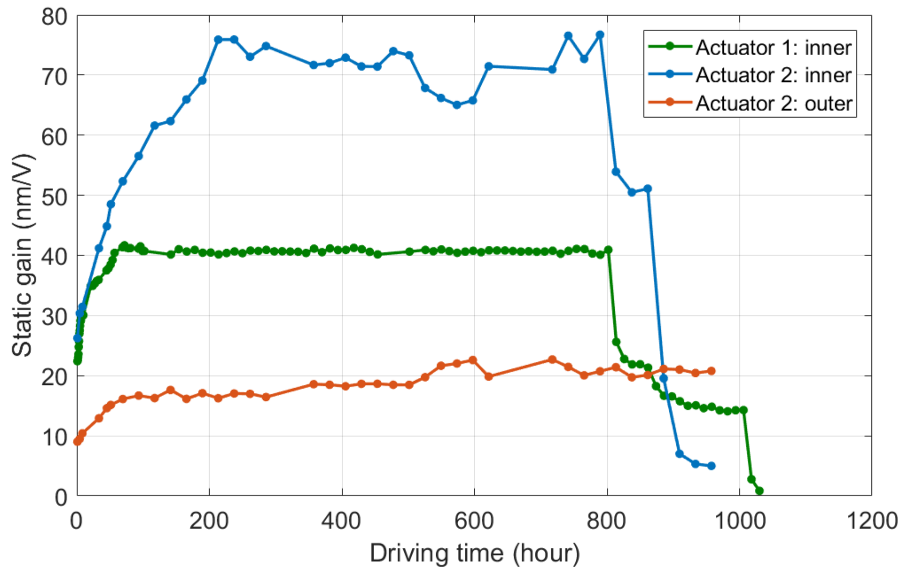

Figure 3-7: The static gain as a function of time for the PZT diaphragm driven in artificial perilymph by a 1V voltage at 10 kHz

For the electrical behavior, the parallel resistance R_p is again extracted as a function of time for probe-2 and shown in Figure 3-8. The blue and the red curves are R_p levels by measuring the center top / bottom electrode pair or the outer top / bottom electrode pair respectively. The red curve (measuring the outer top / bottom electrode pair) shows similar behavior as in the soaking test (c.f. Figure 3-5). Namely, the first 500 hours corresponds to stage-1, for which the R_p level is in the MΩ range, indicating a well encapsulated diaphragm. After 500 hours, a major drop in R_p appears until it stabilizes again in kΩ range. As discussed in the previous section of the soaking test, this significant drop in R_p level results from the failure of the parylene encapsulation layer. Since the long-term driving test in artificial perilymph is terminated at 960 hours, the R_p level does not evolve to stage-3. The blue curve (measuring the center top / bottom electrode pair) also shows similar behavior for the first 760 hours. Namely,

the stage-1 of effective parylene encapsulation happens in 0 – 500 hours and the stage-2 of encapsulation failure happens in 620 − 760 hours. However, unlike the outer electrode, the center electrode evolves into stage-3 much earlier at 800 hours, while the R_p level drops to 10 – 15 Ω. One thing worth noticing is that the drop in R_p is accompanied with the structural failure shown by the blue FRF curve in Figure 3-7.

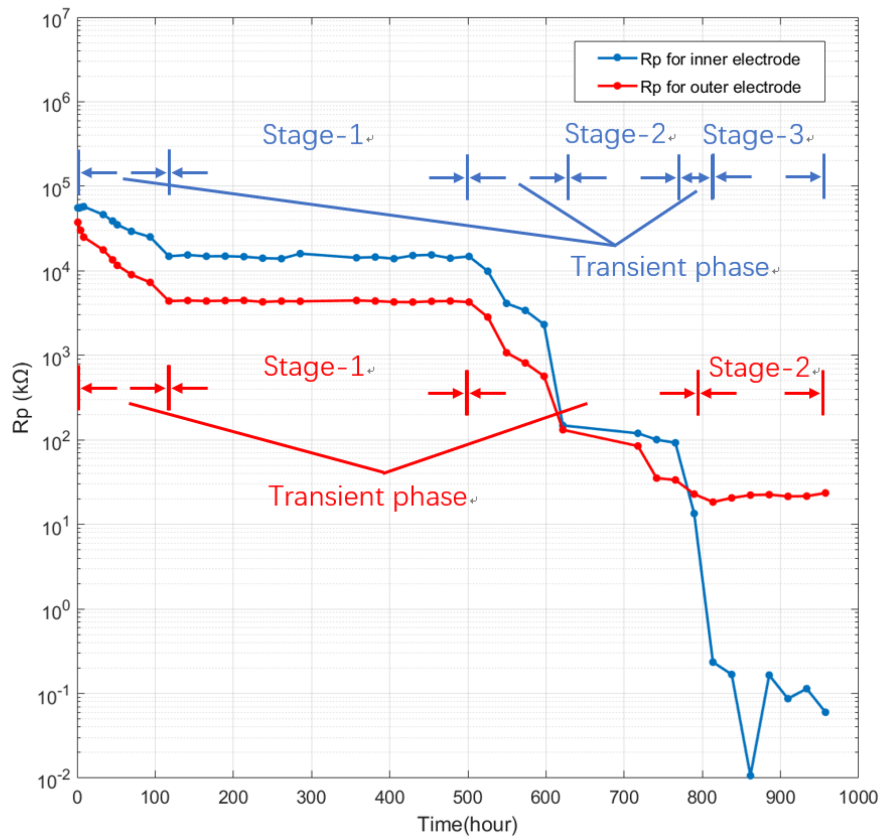

Figure 3-8: The parallel resistance R_p (solid lines) of the PZT diaphragm as a function of time, measured by either center top / bottom electrode pair (in blue color) or outer top / bottom electrode pair (in red color)

3.5 THE FAILURE MODEL

In order to interpret the above phenomena and the failure mechanism, a failure model is established as follows.

The PZT diaphragm fabricated by sol gel methods are highly porous [25] in nature. Since the paylene coating is conformal, it will cover all the exposed areas including the interior of the open pores. Such configuration is schematically shown in Figure 3-9 (a). When a diaphragm of such configuration is submerged in artificial perilymph, the pores will be gradually filled by the surrounding fluid, causing parallel resistance R_p to drop, but the encapsulation is still functional since no metal is in direct contact with the fluid at this stage.

At around 500 hours, the diaphragms in both soaking test and long-term driving tests enter stage-2. For this stage, the parylene coating may be infiltrated at either the top electrodes or the bottom electrode. An electrical pathway is then created, connecting the two electrodes via the conductive fluid (artificial perilymph), causing the R_p level to drop significantly. A schematic view of a diaphragm in stage-2 is shown in Figure 3-9 (b). Such failure model well explains the drop of R_p in both the soaking test (c.f. Figure 3-5) and the long-term driving tests (c.f. Figure 3-8). Furthermore, it is very likely that the metal electrode at stage-2 is still bonded to the PZT layer, since the mechanical behavior of FRF implies that the electrodes can still drive the diaphragm effectively.

For stage-3, we see stable FRF levels for the diaphragm in the soaking test (c.f. both curves in Figure 3-4), and for probe-2 in the long-term driving test driven by top outer / bottom electrode pair (c.f. the red curve in Figure 3-7). However, we also observe an acute drop in the FRF level in the long-term driving test for probe-1 and probe-2 when driving the top inner / bottom electrode pair (c.f. the green and blue curves in Figure 3-7). The above phenomena can

be interpreted by the following failure model. As shown in Figure 3-9 (c), because both the top electrode metals and the PZT are hydrophilic, artificial perilymph has a natural tendency to infiltrate into the interface between those two layers. In such conditions, if the PZT layer is continuous driven (by adding an AC voltage), the top electrode above it may partially delaminate, reducing the driving efficiency significantly. Therefore, we see a major drop in FRF for diaphragms continuously driven and measured at the same pair of electrodes (i.e., the green and blue curves in Figure 3-7), while such drop is not seen for diaphragms free from electrical loadings (i.e., both curves in Figure 3-4). It is worth noticing that for probe-2 in the long-term driving test, only the PZT under the center top electrode is driven continuously. Therefore, the outer top electrode may still be bonded to PZT. That explains why the major drop in FRF is not observed for probe-2 when one measures the outer top / bottom electrode pair (c.f. the red curve in Figure 3-7).

Although the above failure model is theoretically valid and can explain the phenomena seen in the long-term driving tests, it is extremely difficult to obtain microscopic evidences. This is because the sample setup described above (c.f. Figure 3-1) is permanent, and the failure mechanism is too sensitive to the metrology methods. For example, even if one would compromise the long-term driving test by breaking the seal of the petri dish, a cross section sample must first be fabricated for proper observations using metrology equipment such as SEM. It is very likely that the step of breaking the seal and cutting the diaphragm may introduce large uncertainty to the observed results. In particular, it is impossible to tell if the failure is caused by previous long-term driving tests or by the processing steps.

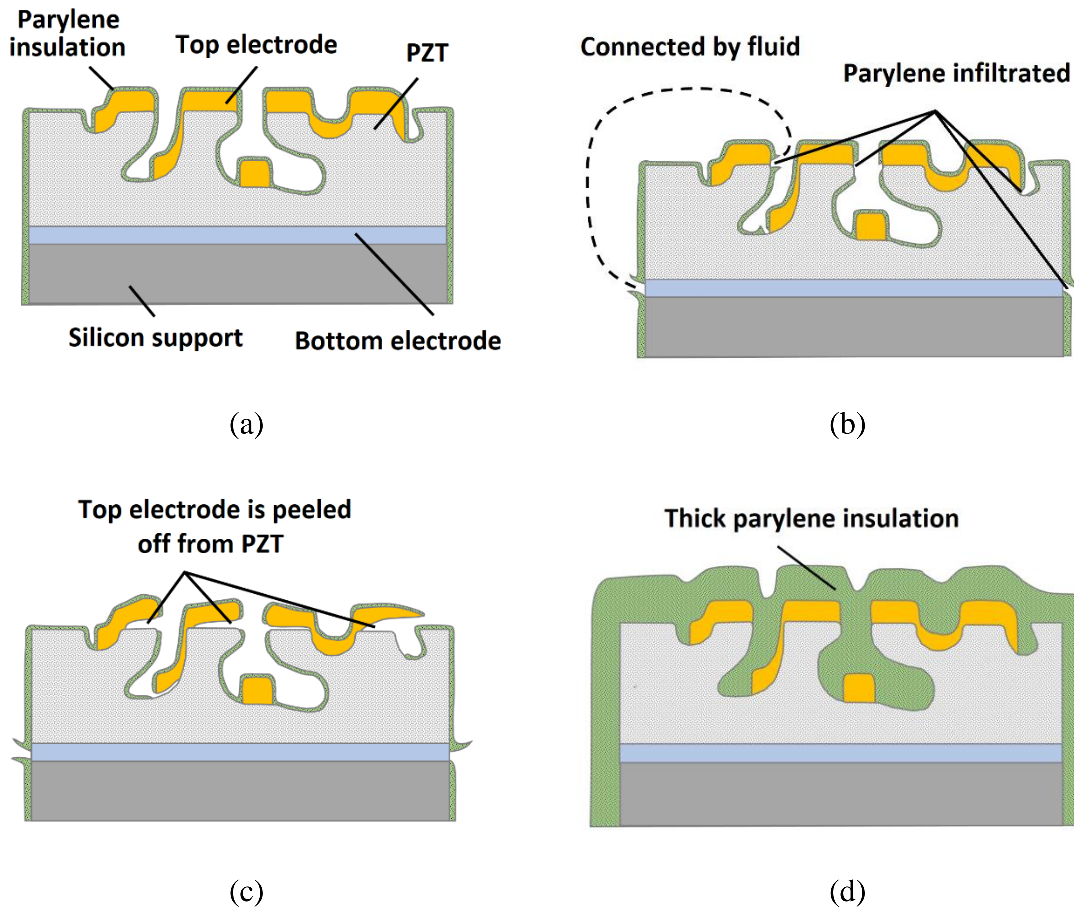

Figure 3-9: Proposed failure mechanism of the PZT diaphragm
(a) at stage-1, well incapsulated; (b) at stage-2, encapsulation failure; (c) at stage-3, top electrode delamination; (d) improved encapsulation strategy by coating a much thicker parylene layer

3.6 Potential Improvements

In artificial perilymph environment, the 1-G probe diaphragm typically fails after 500 hours of driving (or simply soaking). Thus, when the diaphragm evolves to stage-2, although the mechanical FRF does not attenuate, because of the encapsulation failure, there is large current leakage. Therefore, in order to prolong the service life, the encapsulation layer must be redesigned. There are two potential solutions.

The first solution is to deposit a much thicker parylene layer to reduce fluid infiltration. The modified parylene layer can be as thick as that of the PZT (i.e., about 1000 nm, compared with previous thickness of only 25 nm). The reason of adopting much thicker encapsulation is to improve adhesion. Namely, the conformal deposition of parylene may fully occupy the pores in the PZT layer, as shown in Figure 3-9 (d), providing effective anchoring. Although thicker parylene may increase the overall stiffness of the diaphragm, the magnitude of FRF should not see significant drop, since the Young's modulus of parylene is approximately 2 orders of magnitude smaller than that of PZT.

The second solution is to use composite packaging techniques to acquire better robustness and adhesion. One packaging strategy is provided by [36]. Namely, Xie et al. have demonstrated that by pre-depositing a thin layer of Al_2O_3 (e.g. 20 nm) before the coating of parylene may significantly improve the long-term encapsulation of a medical device. Such packaging can also be applied to the intra-cochlear micro-actuator. For this approach, adhesion problem may still exist between Al_2O_3 and parylene. Therefore, surface treatments such as adding surfactants must be performed prior to the parylene coating step.

Chapter 4. STUDY OF LEAD SAFETY

The PZT micro-actuator is designed to vibrate for a long time in human inner ear. Although PZT is a stable metal oxide and a layer of encapsulation exists between the PZT and the surrounding fluid, there is still a theoretical concern of lead leaching. There are two approaches to the lead safety issue.

The first approach is to replace PZT with a lead-free piezoelectric material. Especially, PVDF, a bio-compatible polymer, is discussed in detail and simulated by FE analysis. The results show that none of the replacing material acquires satisfactory mechanical and piezo-electrical properties at the same time.

The second approach is to encapsulate PZT to prevent lead from leaching into the surrounding fluid. For this approach, 1-G probes encapsulated by parylene are driven till complete failure, then the level of lead leaching is measured. Especially, since the encapsulation may fail (at stage-2, refer to Chapter 3) after certain amount of time, the lead leaching after encapsulation failure is investigated in detail. Finally, potential improvements are proposed for better encapsulation of the lead contents.

4.1 ALTERNATIVE PIEZOELECTRIC MATERIALS

For intra-cochlear micro-actuator application, the piezoelectric material of the diaphragm must satisfy two conditions. First, the material should acquire large piezoelectric constants to effectively deform the diaphragm. Second, the material must be stiff to ensure enough bandwidth (i.e., 20 kHz). Common piezoelectric materials include zinc oxide (ZnO), aluminum nitride (AlN) and polyvinylidene fluoride (PVDF). The former two, like PZT, are ceramics, which acquire

large stiffness. However, their piezoelectric coefficients are much smaller compared with PZT. For example, d_{33} for bulk PZT-4 is 289 pC/N [31], while d_{33} is only 11.67 pC/N for ZnO [37] (4.04% of PZT-4) and 5.53 pC/N for AlN [38] (1.91% of PZT-4). Therefore, the diaphragm deformation would be too small if those materials were to be utilized. PVDF is a special biocompatible piezoelectric polymer. Although the piezoelectric constants are still much smaller than PZT (typically 10 – 30 pC/N), being a polymer, a PVDF thin film would be much easier to deform compared with a PZT thin film of the same dimensions. However, such material has two major drawbacks. First, the processing the PVDF involves annealing and mechanical stretching to transfer from α-phase to β-phase, which is not compatible with our current fabrication recipe. Second, due to the small stiffness, the bandwidth of the diaphragm may drop as well. To quantitatively study the feasibility of PVDF diaphragms in intra-cochlear micro-actuator application, FE models are established and simulated as follows.

4.1.1 Double-layer beam model

One easy model to quantitatively compare PVDF against PZT is a cantilever beam model shown in Figure 4-1 (a). The beam is 700 μm in width and 1000 μm in length, clamped at one end. In order to create a bending moment, two layers of piezoelectric material (either PVDF or PZT) are sandwiched by three layers of gold electrodes. The cross section is shown in Figure 4-1 (b). The thicknesses are 10 μm for piezoelectric layers and 0.5 μm for gold electrodes. Both piezoelectric layers are poled in the same direction (i.e., the positive z-direction shown in the figure). When driving the piezoelectric beam, the middle electrode is grounded while the top and the bottom electrodes are applied out of phase voltages (1 V in magnitude). This will cause one piezoelectric layer to extend and the other to contract, inducing a bending moment.

The material properties for PVDF is based on a commercialized product from Precision Acoustics Ltd. [39], which is listed in Table 4-1. For material properties of PZT, we choose to use bulk PZT-4 based on [40]. The finite element shows that for a PVDF double-layer beam, the static gain is 0.060 μm/V and the natural frequency is 8.83 kHz, while for a PZT double-layer beam, the static gain is 0.884 μm/V and the natural frequency is 11.28 kHz. Thus, the static gain would become only 6.79% if PZT were replaced by PVDF. Such significant drop in static gain is rooted from the much smaller piezoelectric constants of PVDF compared with PZT. The natural frequency would become 78.28% as well. The drop in natural frequency is not that significant because the metal electrodes are the same for the two models, which compensates for the stiffness drop. Besides, PVDF does have lower density compared with PZT, which conversely increases the 1st natural frequency. The double-layer beam model implies that the small piezoelectric constants of PVDF may significantly reduce the static gain.

Table 4-1. Material properties of PVDF

Material property description		Value
Density		1780 kg/m^3
Young's modulus		8.3 GPa
Poisson's ratio		0.18
Dielectric constant (relative)		11
Piezoelectric constants	d_{31}	22 pC/N
	d_{32}	3 pC/N
	d_{33}	-30 pC/N

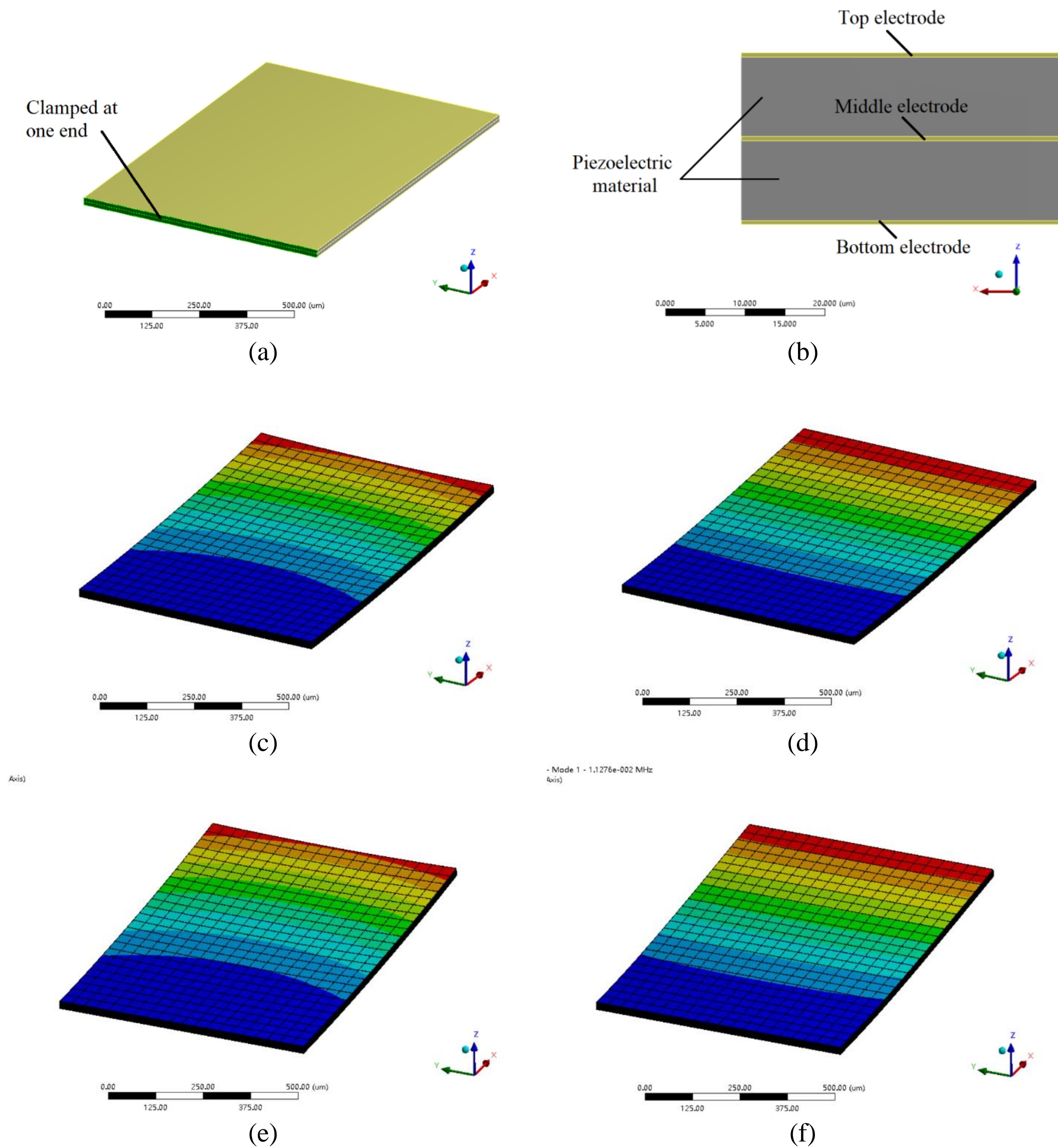

Figure 4-1: FE model of a piezoelectric cantilever beam adopting a double layer structure (a) boundary condition: clamped at one end; (b) cross sectional view; (c) static analysis of a PVDF beam, static gain = 0.060 μm/V; (d) modal analysis of a PVDF beam, 1st natural frequency = 8.83 kHz; (e) static analysis of a PZT beam, static gain = 0.884 μm/V; (f) modal analysis of a PZT beam, 1st natural frequency = 11.28 kHz

4.1.2 Fully anchored diaphragm model

The PVDF and PZT diaphragms are also compared in the special application of PZT micro-actuator. An overview of the model is shown in Figure 4-2 (a) and the cross-sectional view of the diaphragm is shown in Figure 4-2 (b). The FE model is very similar to the full-size fully anchored model in Figure 2-1 except for three differences. First, the total width and length are adjusted to 700 μm (1000 μm for the full-size model). Second, the residual silicon is not modeled for simplicity. Third, piezoelectric properties of bulk material are utilized for easy comparison (refer to detailed parameters in section 4.1.1). For the boundary condition, one end of the actuator is fully clamped (c.f. Figure 4-2 (a)). The bottom electrode is grounded while an out-of-phase voltage of 1V is applied to the center top and the outer top electrodes. Figure 4-2 (c) and (d) shows the deformed diaphragm of PDVF and PZT in static analysis. The static gains are 0.0108 μm/V for PVDF and 0.647 μm/V for PZT. Again, we only see 1.62% of static gain if PZT were to be replaced by PVDF. The results further prove that PVDF is not a feasible option for the piezoelectric material in micro-actuator applications.

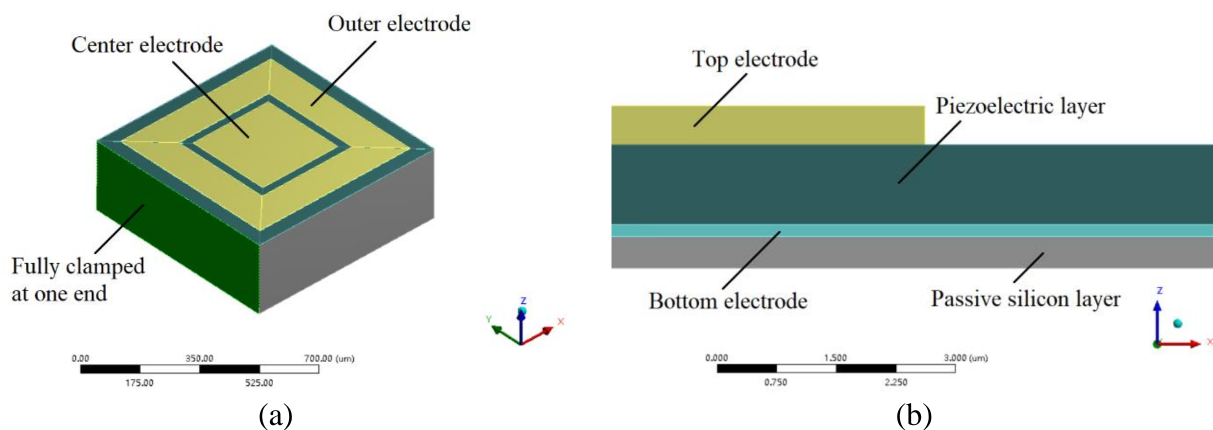

(a) (b)

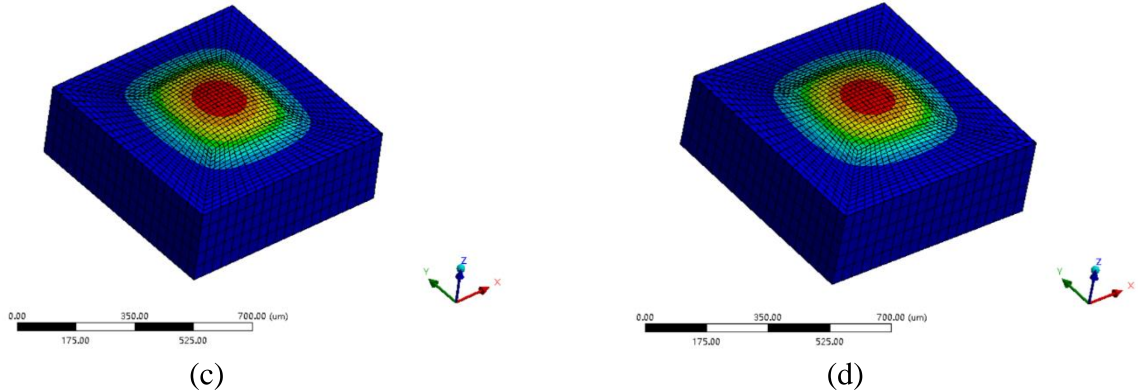

(c) (d)

Figure 4-2: FE model of a piezoelectric micro-actuator adopting fully anchored structure (a) boundary condition: clamped at one end; (b) cross sectional view; (c) static analysis of a PVDF micro-actuator, static gain = 0.0105 μm/V; (d) static analysis of a PZT micro-actuator, static gain = 0.647 μm/V

4.1.3 Tube model

In addition to the double-layer beam model and the fully anchored diaphragm model, other design models are also explored. This section shows one of these design models, the tube model. As shown in Figure 4-3 (a), the piezoelectric thin film is rolled to form a tiny tube. Electrodes are pre-attached to the piezoelectric material on both sides and rolled at the same time forming center electrodes inside the tube and outer electrodes outside of the tube (c.f. Figure 4-3 (b)). The thicknesses of the piezoelectric layer and the electrode layer are 10 μm and 0.5 μm respectively. In particular, four pairs of electrodes exist in a single tube, evenly distributed so that their angular positions are $0°, 90°, 180°, 270°$ respectively (marked in Figure 4-3 (a)). In the poling process, the center electrodes are grounded and same level voltage is applied to the outer electrodes so that the piezoelectric materials are all poled in radial directions. In the driving process. The center electrodes are still grounded, while we applied out of phase voltages to the

$[0°, 180°]$ and the $[90°, 270°]$ electrodes. This will cause the tube to extend in one direction (i.e., the x or y direction shown in Figure 4-3 (a)) while contract in the other direction.

Such actuating mechanism has one advantage that the tube is able to create acoustic waves in all directions (while the beam model and the diaphragm model can only generate acoustic waves perpendicular to the plane of diaphragm). Again, in the finite element analysis, the material properties of PVDF and PZT follow Table 4-1 and the bulk PZT-4 respectively. The static gains are 5.48 nm/V for PVDF tube (c.f. Figure 4-3 (c)) and 82.41 nm/V for PZT tube (c.f. Figure 4-3 (d)). Again, the static gain would become only 6.65% if PZT were replaced by PVDF, even smaller than the previous two models. The 1st natural frequencies are 31.15 kHz for the PVDF tube (c.f. Figure 4-3 (e)) and 47.50 kHz for the PZT tube (c.f. Figure 4-3 (f)). Compared with beams and diaphragms the previous sections, a tube structure acquires much larger bandwidth. One may also notice from the mode shape shown in Figure 4-3 (d) and (f) that the deformation of the tube is along the $[-45°, 135°]$ line. This is reasonable since there is no electrodes in that direction, which makes the tube easier to deform.

In summary, the tube design model can generate acoustic waves in all directions, and usually has large bandwidth. However, because the tube structure is very stiff, its static gain is even smaller than the double layer beam model and the fully anchored diaphragm model. Therefore, we can neither utilize such design.

The other designs adopt different actuating mechanisms, but altogether show two general rules. First, for the same design, the static gain would drop significantly if PZT were replaced by PVDF. Second, under the size (less than 700 μm in width) and bandwidth (over 20 kHz) constraints, the static gain of the design using PVDF would become too small to be feasible for intra-cochlear micro-actuator applications.

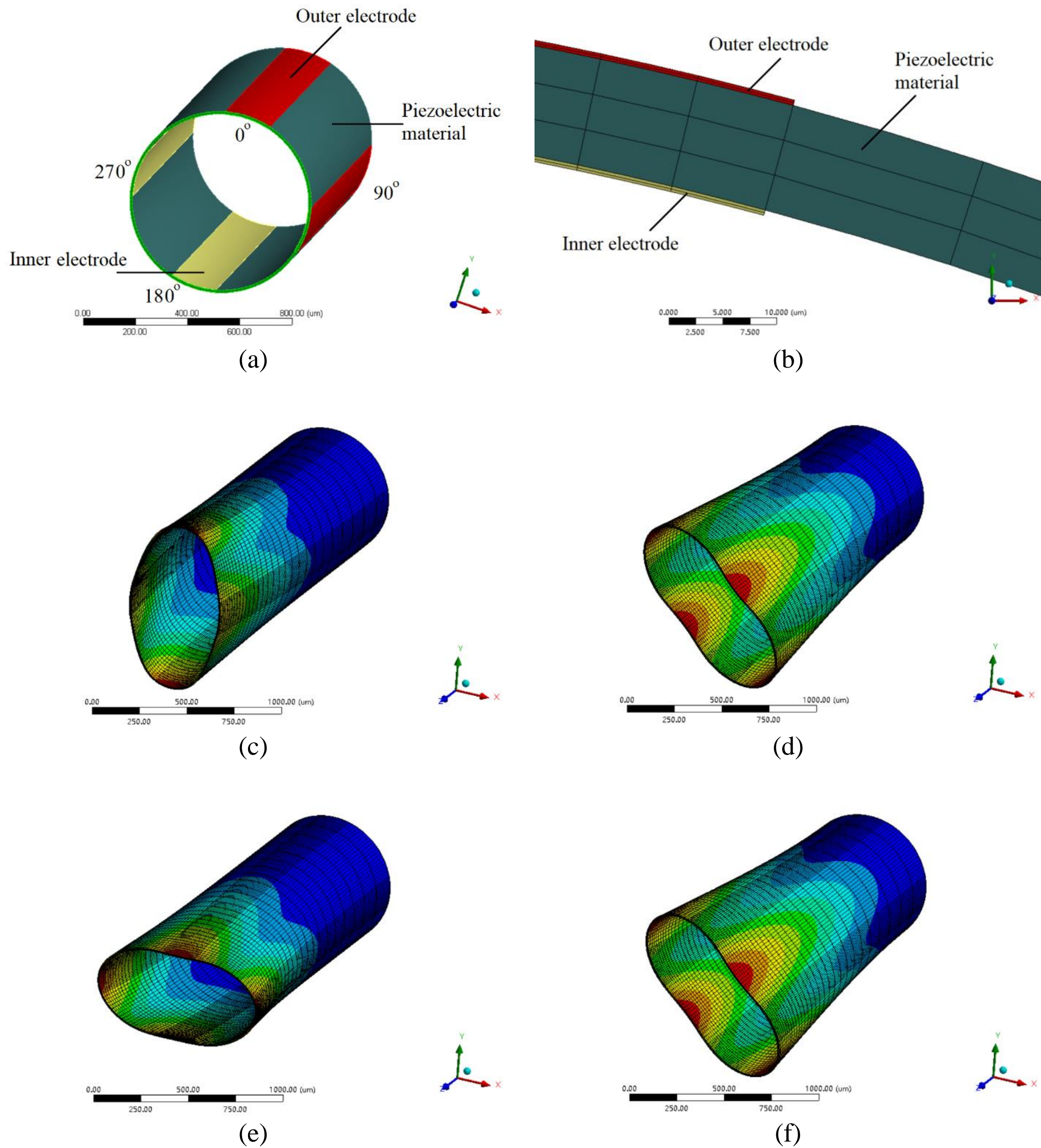

Figure 4-3: FE model of a piezoelectric actuator adopting tube structure
(a) boundary condition: clamped at one end; (b) cross sectional view; (c) static analysis of PVDF tube model, static gain = 5.48 nm/V; (d) modal analysis of PVDF tube model, 1st natural frequency = 31.15 kHz; (e) static analysis of PZT tube model, static gain = 82.41 nm/V; (f) modal analysis of PZT tube model, 1st natural frequency = 47.50 kHz

4.2 STUDY OF LEAD LEACHING

In addition to finding an alternative piezoelectric material, the other approach to solve the lead issue is to seal the PZT from leaching into the surrounding fluid. The lead content is measured by the following methods.

Before each long-term test, part of the artificial perilymph to be filled into the glass bottom petri dish (c.f. Figure 3-1) is reserved and a total volume of 4.5 mL is collected as compare group (referred to as “compare sample” for the rest of the dissertation). After the long-term test, the artificial perilymph in the petri dish is collected through the temporarily taped hole (c.f. Figure 3-1). 4.5 mL of the collected fluid sample is then mixed with 0.5 mL concentrated nitric acid. (The mixed sample is referred to as “test sample” for the rest of the dissertation.) The overall concentration of lead, including both lead ion and stripped residual lead solids, is then measured via inductive coupled plasma mass spectrometry (ICP-MS) based on EPA 6020a Rev.1 2007.

Assume m_c and m_t to be the measured mass of the lead content in compare sample and test sample respectively. Then the lead leached during the driving process is $(m_t - m_c)$. An important factor evaluating the lead leaching is the equivalent lead concentration in human cochlea, which is given by,

$$\text{Equivalent Lead Concentration} = \frac{m_t - m_c}{V_{sample}} \cdot \frac{V_{petri_dish}}{V_{perilymph}} \quad \text{Eqn. 8}$$

Where $V_{sample} = 4.5$ mL, $V_{petri_dish} = 25$ mL, and $V_{perilymph} = 0.16$ mL are the volumes of the sample fluid, the glass bottom petri dish, and the perilymph of human inner ear, respectively. The formula is interpreted as follows. First, the lead concentration in the sample fluid is given by $(m_t - m_c)\ /\ V_{sample}$. Assume the lead contents are evenly distributed. (This is a reasonable

assumption because the stripped lead solids, if there are any, have already been dissolved by the nitric acid.) Then the total amount of lead leached is $(m_t - m_c) \cdot V_{petri_dish} / V_{sample}$. If we consider the worst scenario in which all the lead contents are dissolved into the small volume of perilymph in human cochlea, the total amount of lead leached is then divided by $V_{perilymph}$ to obtain the equivalent lead concentration in Eqn. 8.

Table 4-2 lists the results of lead leaching tests. There are totally three sets of data from three reliability tests (i.e., one soaking test and two long-term driving tests). The first two columns are the corresponding m_c and m_t values. We see that the mass of the lead content is in nano-gram level. Since the process of making artificial perilymph does not involve lead, the m_c level can be approximately considered as the "minimal lead" level. From the first and the third row of Table 4-2, we see that the lead content mass generally becomes 4-5 times the "minimal lead" level, after exposure to the PZT actuator for a long time.

The third column is the equivalent lead concentration in human cochlea, which is calculated using Eqn. 8. In the worst scenario, the equivalent lead level would reach 50.78 ng/mL. This lead level can be interpreted as following. First, the lead advisory level in blood published by the center of disease control is under 100 ng/mL, while the calculated level of 50.78 ng/mL is well below that level. Second, the calculated level assumes the worst scenario that all lead contents leached from the PZT actuator are dissolved and confined in the small volume of perilymph in human inner ear. Third, the parylene encapsulation can also prevent the lead from leaching. However, as discussed in Chapter 3, such encapsulation is infiltrated after about 500 hours. Since the long-term tests generally are performed over 1000 hours, the artificial perilymph is in direct contact with PZT for over 500 hours. Such direct contact may have increased the leached lead significantly. Therefore, we reach the following conclusion: The

lead leaching of the PZT inctra-cochlear micro-actuator is acceptably slow, even after the encapsulation layer is failed.

Table 4-2. Results of the lead leaching tests

Sample description	Lead content mass in compare sample: m_c (ng)	Lead content mass in test sample: m_t (ng)	Equivalent lead concentration in human cochlea (ng/mL)
Sample in soaking test	0.360	1.823	50.78
Sample in long-term driving test of probe-1	0.968	1.305	11.72
Sample in long-term driving test of probe-2	0.360	1.395	35.94

Theoretically, one can further lower the lead leaching level by designing proper encapsulation. This topic has already been covered in Section 3.6. Namely, the lead leaching level may be further decreased if a thicker parylene layer is utilized or an additional layer of Al_2O_3 is deposited.

Finally, one may notice from Table 4-2 that the level of m_c for the long-term driving test sample of probe-1 (i.e., the 2nd row) is abnormally large (0.968 ng). The reason for such large m_c is unknown. The 4.5 mL compare sample is collected from the batch of artificial perilymph right before it is filled into the glass bottom petri dish (for the long-term driving test of probe-1). Therefore, one is not able to do a double-check test. Besides, since the artificial perilymph samples are byproducts of the long-term tests, it is not possible to test the lead contents at middle stages without compromising the long-term tests. First, the long-term tests utilize sealed environment to prevent contamination, which may be compromised if fluid is drawn during the long-term test. Second, the petri dish is filled by fluid so as to exclude air bubbles near the

examining glass (c.f. Figure 3-1). Extracting fluid may also introduce air bubbles that drifts the laser beam of LDV, causing error in FRF measurements. Therefore, the lead leaching test results in Table 4-2 are preliminary.

Chapter 5. CONCLUSIONS AND FUTURE WORKS

5.1 CONCLUSIONS

This dissertation is focused on the characterizations and improvements of a PZT intra-cochlear micro-actuator. Three major problems have been addressed. They are the size reduction of the micro-actuator, the reliability in a long-term service, and the issue of lead safety.

The study of size reduction can be concluded as follows:

1. A proportional size reduction while keeping the fully anchored diaphragm may cause the static gain to drop significantly. However, finite element analysis shows that by partially releasing the diaphragm (i.e., by through etching two open slots in the lateral direction), the static gain can be significantly enhanced for the same level bandwidth. Although by adopting the partially released diaphragm, the generated acoustic pressure may drop by 50%, the bandwidth may increase accordingly due to a reduction of added mass effect.
2. The fabrication of the PZT micro-actuator with partially released diaphragm is not a trivial task. One needs alignments and fabrications of six layers in order to create the partially released diaphragm. Especially, five major challenges are overcome. They are the patterning of bottom electrode, the elimination of cat-ear, the annealing of bottom electrode, and patterning of PZT by wet etching, and the through etching by double-side DRIE.
3. The characterization study of the partially released micro-actuators shows a much smaller static gain than the finite element prediction, while the first natural frequency is abnormally low. This is because the static gain results from the diaphragm deflection while the first natural frequency results from cantilever bending vibration. Therefore, precise control of the

unetched silicon layer thickness and elimination of the residual silicon are crucial in producing partially released diaphragms of desired performance.

The study of reliability can be concluded as follows:

1. By adopting the sealing design based on a glass bottom petri dish, the problems of evaporation and contamination are overcome.
2. Two failure mechanisms are identified, i.e., the electrical failure and the structural failure. Electrical failure usually occurs before structural failure, and is caused by infiltration of artificial perilymph into the parylene encapsulation layer. The infiltrated pathway then forms electrical bridges connecting the bottom and the top electrodes, causing short circuits. Structural failure is usually induced by delamination of the top electrode. Such delamination process may be accelerated by the continuous vibration of the diaphragm.
3. The parallel resistance R_p is an ideal indicator to monitor diaphragm integrity in vivo conditions such as the human inner ear. Namely one only needs to measure the impedance, and extract R_p using the electrical model. Then the first significant drop in the R_p level usually corresponds to the failure of encapsulation.

The study of lead leaching can be concluded as follows:

1. Study on alternative lead-free piezoelectric material shows that PZT is still the only viable candidate for intra-cochlear micro-actuators. Other materials either have too small piezo-electric constants or too small Young's modulus (or both) to be feasible.
2. The equivalent lead concentrations in human inner ear are calculated after driving 1-G probes in artificial perilymph to complete failure. The results suggest a concentration of

51ng/mL in the worst-case scenario, while the lead advisory level in blood published by the Center of Disease Control is not to exceed 100 ng/mL. Such concentration is trivial considering the fact that PZT is in direct contact with artificial perilymph for more than half of the driving period.

5.2 Future Works

The future works following the lines of the PZT intra-cochlear micro-actuator can be divided into four steps.

Step-1 is improvements based on the current configurations. For size reduction, new prototypes of 2-G probes with geometrical parameters given by parametric studies in section 2.4 need to be developed. If one requires further enhancements in static gain, methods to precisely control the thickness of the unetched silicon layer and the size of the residual silicon need to be developed. For reliability and lead leaching control, a more reliable encapsulation strategy must be developed either by adopting a thicker parylene layer or by composite packaging using a secondary layer such as Al_2O_3.

Step-2 is a series of characterizations. Namely, in order to validate the geometric parameters and the encapsulation strategy, the fabricated 2-G probes and the encapsulated 1-G probes described in Step-1 need to be tested. In particular, for the 2-G probes, the static gain and bandwidth are to be evaluated by measuring the frequency response function. For the encapsulated 1-G probes, a series of long-term tests and lead leaching tests are to be carried.

Step-3 is the study of reliability and lead leaching of a partially released diaphragm. Once the concepts are proved in Step-2, the encapsulation strategy can be applied to the new 2-G

probes. Then a series of long-term tests and lead leaching tests can be performed on a 2-G probe model following similar procedures as in the 1-G probes.

Step-4 is new designs and characterizations. Currently, we have performed short term tests both in vitro and in vivo (i.e., the animal tests [30]), as well as long-term tests in vitro. For all these tests, the actuator is placed at the tip of a silicon cantilever probe for easy operations. However, such design is not compatible for long-term tests in vivo (based on a guinea pig model). From the experience of previous tests in vitro, the device is expected to be in the body of the animal for more than 30 days. For such long time, the long silicon cantilever may intervene in the animal movements, or even cause damage to its inner ear. Therefore, for long-term tests in vivo, the silicon cantilever probe part must be eliminated. This may introduce new challenges in terms of fabrications, encapsulations and characterizations. For example, one needs to design a reliable fixture mechanism to properly anchor the new actuator to the bones in the ear canal. Another example would be the compatibility problem. Namely, the wiring should be re-designed for the new actuator to cooperate with the shortened electrode array during electrical and acoustic stimulations.

BIBLIOGRAPHY

[1] Gantz, Bruce J and Turner, Christopher and Gfeller, Kate E and Lowder, Mary W, "Preservation of hearing in cochlear implant surgery: advantages of combined electrical and acoustical speech processing," *The Laryngoscope,* vol. 115, no. 5, pp. 796--802, 2005.

[2] Wilson, Blake S and Lawson, Dewey T and M{\"u}ller, Joachim M and Tyler, Richard S and Kiefer, Jan, "Cochlear implants: some likely next steps," *Annual Review of Biomedical Engineering,* vol. 5, no. 1, pp. 207--249, 2003.

[3] Dorman, Michael F and Gifford, Rene H, "Combining acoustic and electric stimulation in the service of speech recognition," *International journal of audiology,* vol. 49, no. 12, pp. 912--919, 2010.

[4] Kong, Ying-Yee and Stickney, Ginger S and Zeng, Fan-Gang, "Speech and melody recognition in binaurally combined acoustic and electric hearing," *The Journal of the Acoustical Society of America,* vol. 117, no. 3, pp. 1351--1361, 2005.

[5] Dorman, Michael F and Gifford, Rene H and Spahr, Anthony J and McKarns, Sharon A, "The benefits of combining acoustic and electric stimulation for the recognition of speech, voice and melodies," *Audiology and Neurotology,* vol. 13, no. 2, pp. 105--112, 2008.

[6] Luo, Xin and Fu, Qian-Jie and Galvin III, John J, "Cochlear implants special issue article: Vocal emotion recognition by normal-hearing listeners and cochlear implant users," *Trends in amplification,* vol. 11, no. 4, pp. 301--315, 2007.

[7] Turner, Christopher W and Gantz, Bruce J and Vidal, Corina and Behrens, Amy and Henry, Belinda A, "Speech recognition in noise for cochlear implant listeners: benefits of residual acoustic hearing," *The Journal of the Acoustical Society of America,* vol. 115, no. 4, pp. 1729--1735, 2004.

[8] Koch, M and Evans, AGR and Brunnschweiler, A, "The dynamic micropump driven with a screen printed PZT actuator," *Journal of Micromechanics and Microengineering,* vol. 8, no. 2, p. 119, 1998.

[9] Shibata, Takayuki and Unno, Kazuya and Makino, Eiji and Shimada, Shiro, "Fabrication and characterization of diamond AFM probe integrated with PZT thin film sensor and actuator," *Sensors and Actuators A: Physical,* vol. 114, no. 2-3, pp. 398--405, 2004.

[10] Miyahara, Y and Deschler, M and Fujii, T and Watanabe, S and Bleuler, H, "Non-contact atomic force microscope with a PZT cantilever used for deflection sensing, direct oscillation and feedback actuation," *Applied surface science,* vol. 188, no. 3-4, pp. 450--455, 2002.

[11] Miyahara, Y and Fujii, T and Watanabe, S and Tonoli, Andrea and Carabelli, S and Yamada, H and Bleuler, H, "Lead zirconate titanate cantilever for noncontact atomic force microscopy," *Applied surface science,* vol. 140, no. 3-4, pp. 428--431, 1999.

[12] Wang, Zhihong and Zhu, Weiguang and Yao, Xi, "d31 Type inplane bending multilayer piezoelectric microactuators—a design concept and its applications," *Sensors and Actuators A: Physical,* vol. 101, no. 3, pp. 262--268, 2002.

[13] Jing, Yang and Luo, Jianbin and Yi, Xiaoxing and Gu, Xin, "Design and evaluation of PZT thin-film micro-actuator for hard disk drives," *ensors and Actuators A: Physical,* vol. 116,

no. 2, pp. 329--335, 2004.

[14] Morita, Takeshi and Kurosawa, Minoru Kuribayashi and Higuchi, Toshiro, "A cylindrical shaped micro ultrasonic motor utilizing PZT thin film (1.4 mm in diameter and 5.0 mm long stator transducer)," *Sensors and Actuators A: Physical,* vol. 83, no. 1-3, pp. 225--230, 2000.

[15] Morita, Takeshi and Kurosawa, Minoru and Higuchi, Toshiro, "An ultrasonic micromotor using a bending cylindrical transducer based on PZT thin film," *Sensors and Actuators A: Physical,* vol. 50, no. 1-2, pp. 75--80, 1995.

[16] Xu, Ting and Wang, Zhihong and Miao, Jianmin and Yu, Ling and Li, Chang Ming, "Micro-machined piezoelectric membrane-based immunosensor array," *Biosensors and Bioelectronics,* vol. 24, no. 4, pp. 638--643, 2008.

[17] Nicu, Liviu and Guirardel, Matthieu and Chambosse, Fr{\'e}d{\'e}ric and Rougerie, Pierre and Hinh, Sary and Trevisiol, Emmanuelle and Francois, Jean-Marie and Majoral, Jean-Pierre and Caminade, Anne-Marie and Cattan, Eric and others, "Resonating piezoelectric membranes for microelectromechanically based bioassay: detection of streptavidin--gold nanoparticles interaction with biotinylated DNA," *Sensors and Actuators B: chemical,* vol. 110, no. 1, pp. 125--136, 2005.

[18] Kawashima, Takahiro and Yamada, Yuhei and Matsuzawa, Yuuta and Nagai, Moeto and Shibata, Takayuki and Masuzawa, Toru and Kimura, Tsuyoshi and Kishida, Akio, "Development of Cell Culture Microdevice Integrated with Piezoelectric Thin Film Actuator for On-Chip Regulation of Cell Functions," *Japanese Journal of Applied Physics,* vol. 51, no. 10R, p. 107201, 2012.

[19] Kim, Eun Sok and Muller, Richard S, "IC-processed piezoelectric microphone," *IEEE electron device letters,* vol. 8, no. 10, pp. 467--468, 1987.

[20] Kim, ES and Kim, JR and Muller, RS, "Improved IC-compatible piezoelectric microphone and CMOS process," *Solid-State Sensors and Actuators, 1991. Digest of Technical Papers, TRANSDUCERS'91., 1991 International Conference on,* pp. 270--273, 1991.

[21] Lee, Woon Seob and Lee, Seung S, "Piezoelectric microphone built on circular diaphragm," *Sensors and Actuators A: Physical,* vol. 144, no. 2, pp. 367--373, 2008.

[22] Williams, Matthew D and Griffin, Benjamin A and Reagan, Tiffany N and Underbrink, James R and Sheplak, Mark, "An AlN MEMS piezoelectric microphone for aeroacoustic applications," *Journal of Microelectromechanical Systems,* vol. 21, no. 2, pp. 270--283, 2012.

[23] Defay, E and Millon, Cyril and Malhaire, Ch and Barbier, D, "PZT thin films integration for the realisation of a high sensitivity pressure microsensor based on a vibrating membrane," *Sensors and Actuators A: Physical,* vol. 99, no. 1-2, pp. 64--67, 2002.

[24] Olfatnia, M and Xu, T and Miao, JM and Ong, LS and Jing, XM and Norford, L, "Piezoelectric circular microdiaphragm based pressure sensors," *Sensors and Actuators A: Physical,* vol. 163, no. 1, pp. 32--36}, 2010.

[25] Luo, Chuan and Cao, GZ and Shen, IY, "Development of a lead-zirconate-titanate (PZT) thin-film microactuator probe for intracochlear applications," *Sensors and Actuators A: Physical,* vol. 201, pp. 1--9, 2013.

[26] Luo, Chuan and Cao, GZ and Shen, IY, "Enhancing displacement of lead--zirconate--

titanate (PZT) thin-film membrane microactuators via a dual electrode design," *Sensors and Actuators A: Physical,* vol. 173, no. 1, pp. 190--196, 2012.

[27] Lee, Cheng-Chun and Guo, Qing and Cao, GZ and Shen, IY, "Effect of electrode size and silicon residue on piezoelectric thin-film membrane actuators," *Sensors and Actuators A: Physical,* vol. 147, no. 1, pp. 279--285, 2008.

[28] Luo, Chuan, "PZT Thin Film Micro Probe Device with Dual Top Electrodes," *University of Washington,* 2013.

[29] Nuttall, Alfred L and LaRouere, Michael J and Lawrence, Merle, "Acute perilymphatic perfusion of the guinea pig cochlea," *Hearing Research,* vol. 6, pp. 207 - 221, 1982.

[30] Luo, Chuan and Omelchenko, Irina and Manson, Robert and Robbins, Carol and Oesterle, Elizabeth C and Cao, Guo Zhong and Shen, IY and Hume, Clifford R, "Direct Intracochlear Acoustic Stimulation Using a PZT Microactuator," *Trends in hearing,* vol. 19, no. 2331216515616942, 2015.

[31] "Piezoelectric material of PZT-4," eFunda, [Online]. Available: http://www.efunda.com/materials/piezo/material_data/matdata_output.cfm?Material_ID=PZT-4. [Accessed 28 8 2018].

[32] Guo, Qing and Cao, GZ and Shen, IY, "Measurements of piezoelectric coefficient d33 of lead zirconate titanate thin films using a mini force hammer," *Journal of Vibration and Acoustics,* vol. 135, no. 1, p. 011003, 2013.

[33] Wang, L-P and Wolf, R and Zhou, Q and Trolier-McKinstry, S and Davis, RJ, "et-etch patterning of lead zirconate titanate (PZT) thick films for microelectromechanical systems (MEMS) applications," *MRS Online Proceedings Library Archive,* vol. 657, 2000.

[34] Wu, Chia-Che and Lee, Cheng-Chun and Cao, GZ and Shen, IY, "Effects of corner frequency on bandwidth and resonance amplitude in designing PZT thin-film actuators," *Sensors and Actuators A: Physical,* vol. 125, no. 2, pp. 178--185, 2006.

[35] Guo, Qing, "Development of Thin-Film Based Microdevices and Process Enhancement for Making the Same," *University of Washington,* 2012.

[36] Xie, Xianzong and Rieth, Loren and Caldwell, Ryan and Diwekar, Mohit and Tathireddy, Prashant and Sharma, Rohit and Solzbacher, Florian, "Long-Term Bilayer Encapsulation Performance of Atomic Layer Deposited Al2O3 and Parylene C for Biomedical Implantable Devices," *IEEE Transactions on Biomedical Engineering,* vol. 60, no. 10, pp. 2943-2951, 2013.

[37] "Piezoelectric material of Zinc Oxide," eFunda, [Online]. Available: http://www.efunda.com/materials/piezo/material_data/matdata_output.cfm?Material_ID=ZnO. [Accessed 28 8 2018].

[38] H. Landolt and R. Börnstein, "Aluminum nitride (AlN) piezoelectric constants," SpringerLink, [Online]. Available: https://link.springer.com/chapter/10.1007/10551045_47. [Accessed 28 8 2018].

[39] "Piezo-Electric PVdF," Precision Acoustics Ltd., [Online]. Available: https://www.acoustics.co.uk/product/pvdf/. [Accessed 28 8 2018].

[40] "Piezoelectric material of PZT-4," eFunda, [Online]. Available: http://www.efunda.com/materials/piezo/material_data/matdata_output.cfm?Material_ID=PZT-4. [Accessed 28 8 2018].

[41] Nuttall, Alfred L and LaRouere, Michael J and Lawrence, Merle, "Acute perilymphatic perfusion of the guinea pig cochlea," *Hearing research,* vol. 6, no. 2, pp. 207--221, 1982.

[42] Lee, Cheng-Chun and Cao, GZ and Shen, IY, "Effects of residual stresses on lead--zirconate--titanate (PZT) thin-film membrane microactuators," *Sensors and Actuators A: Physical,* vol. 159, no. 1, pp. 88--95, 2010.

[43] Guo, Qing and Cao, GZ and Shen, IY, "Measurements of piezoelectric coefficient d33 of lead zirconate titanate thin films using a mini force hammer," *Journal of Vibration and Acoustics,* vol. 135, no. 1, p. 011003, 2013.

[44] L. Chang, Foundations of MEMS, Person Prentice Hall, 2006.

[45] Olzick, Adam, "Deposition, characterization, and fabrication of a zinc oxide piezoelectric thin film microspeaker using dc reactive sputtering," 2012.

[46] Vijaya, MS, Piezoelectric materials and devices: Applications in engineering and medical sciences, CRC Press, 2012.

[47] Esterly, Daniel Mason, "Manufacturing of Poly (vinylidene fluoride) and Evaluation of its Mechanical Properties," *Virginia Tech,* 2002.

APPENDIX A

FABRICATION RECIPE OF THE 2G-PROBE

1. Substrate Preparation

(1) Use 4" silicon wafer with <1-0-0> orientation.

(2) Polished on both sides to thickness ≈ 250 μm.

(3) 5000 Å of silicon oxide grown by wet thermal oxidation.

(4) 2000 Å of silicon nitride deposited by low pressure LPCVD (tensile stress ≈ 250 MPa).

**The above preparations can be done by outside manufacturers.*

(5) Number wafers by diamond pen.

(a) The thinned wafers are fragile. Handle carefully.

(b) Process better be done in clean room

2. Alignment Mark

**The first step is to imprint alignment marks on each silicon wafer by etching the surface silicon nitride, exposing the purple colored silicon oxide. Silicon oxide is purple colored, which is easy to recognize, and is also inert to most of the chemical solutions and treatments in the following fabrication steps.*

(1) Wafer clean: Standard RCA clean (without BOE dip) is preferred, but EKC830 clean is also acceptable.

(2) **[HMDS oven]** HMDS adhesion layer application: run the standard recipe.

**HMDS acts as a primer for better adhesion of the photo-resist to the substrate.*

(3) Pattern by lithography:

(a) **[Spin-1 or 2]**:

(i) Resist: AZ-1512

Time (s)	Target (rpm)	Ramp (rpm/s)
3	500	250
45	4000	2000

(ii) Soft bake: 110°C for 60s, contact bake with vacuum.

**Result in thin photo-resist layer.*

(b) Exposure:

(i) By the "Alignment Mark" mask

(ii) **[ABM aligner]** Time = 4s.

**ABM aligner is recommended because it is easier to align the major and minor flats of the wafers for the very first layer. No need to use the aligner at this stage.*

(iii)Develop: AZ340:DI = 1:4 for 40 s.

(iv)**[Nikon microscope]** Exam pattern quality under green light.

(4) **[Vision RIE]** Etch alignment marks.

(a) By "MFF: Silicon Nitride Etch" recipe.

(b) Time = 5 min.

(c) Take out and exam by bare eyes: should be purple.

EKC830 clean.

3. Backside Pre-etching

**It is found that the backside etching is non-uniform partially because the dry etching rates of silicon oxide differs between cavities. Namely, when the underneath silicon is already partially etched in some areas, silicon oxide still exists in some other areas. This step is to use BOE to etch all the exposed silicon oxide on the backside, so that the final DRIE step will have the same starting point.*

(1) Wafer clean: Standard RCA clean (without BOE dip) is preferred, but EKC830 clean is also acceptable.

(2) **[HMDS oven]** HMDS adhesion layer application: run the standard recipe.

(3) Pattern by lithography:

(a) **[Spin-1 or 2]**:

(i) Resist: AZ-9260

Time (s)	Target (rpm)	Ramp (rpm/s)
5	500	250
45	3000	1000

(ii) Soft bake: 110°C for 80s, contact bake with vacuum.

**Result in medium thick photo-resist layer.*

(b) Exposure:

(i) By the “Backside DRIE” mask

(ii) **[EVG Aligner]** Time = 45s.

**EVG aligner is recommended because it can more accurately align to the alignment marks on the other side.*

(iii)Develop: AZ400k:DI = 1:4 for 3min 30s.

(iv)**[Nikon microscope]** Exam pattern quality under green light.

**Make sure no residual photo-resist left in open areas.*

(4) **[Vision RIE]** Etch exposed silicon nitride.

(a) By “MFF: Silicon Nitride Etch” recipe.

(b) Time = 5 min.

(c) Take out and exam by bare eyes: should be purple.

(5) **[BOE bath]** for 5 min

**BOE usually takes less than 5 min to etch all the underneath silicon oxide. We do slight over etching to make sure all the silicon oxide exposed is get etched. BOE is highly selective to etching silicon oxides and inert to silicon. Therefore, such slight over etching will not become a problem.*

(a) Take two small Teflon containers (T-1 & T-2) and one large glass container (G-1).

(b) Put small volume of 10:1 BOE to T-1. Half fill T-2 and G-1 with DI water.

(c) Dwell in 10:1 BOE (i.e., T-1) for 5 min.

(d) Dwell in T-2 for 5 min with agitation by hand.

(e) Dwell in G-1 till the end of etching.

(6) EKC830 clean.

4. Bottom electrode deposition and patterning

**The whole bottom electrode deposition, patterning and annealing step is the trickiest step and can directly affect the quality of PZT. Do it carefully!*

(1) Wafer clean: RCA clean. Make sure to clean thoroughly.

At least 15 min of SC-1 and more than 5 min of SC-2 is recommended.

(2) **[HMDS oven]** HMDS adhesion layer application: run the standard recipe.

(3) Pattern by lithography:

(a) **[Spin-1 or 2]**:

(i) Resist: AZ-1512

Time (s)	Target (rpm)	Ramp (rpm/s)
3	500	250
45	4000	2000

(ii) Soft bake: 110ºC for 60s, contact bake with vacuum.

(b) Exposure:

(i) By the "Ti & Pt positive" mask

(ii) **[EVG aligner]** Time = 5s.

**Both ABM aligner and EVG aligner can do front side exposure. But EVG aligner usually have better alignment quality.*

**Due to large exposing area, slightly longer exposure time is applied to make sure all the exposed resist will dissolve in developer.*

**If using ABM aligner, the exposure time = 4.4s.*

(iii)Develop: AZ340:DI = 1:4 for 60 s with agitation.

** Longer developing time and agitation are to make sure resist is totally dissolved.*

(iv)**[Nikon microscope]** Exam pattern quality under green light.

** Make sure no residual resist in open area. Resist residue will burn in the annealing step!*

(4) Ti & Pt deposition:

**DO NOT hard bake! Hard bake will deform the resist pattern and smoothen the sharp edges of teh photo-resist, causing the lift-off harder to perform.*

(a) **[Kapton tape]** Tape the major alignment mark areas.

**So that metal will not deposited onto the alignment mark areas.*

(b) **[EVAP- 1]** Ti & Pt deposition:

(i) N_2 gun blow right before substrate loading.

(ii) 500 Å of Ti @ 1 Å /s.

(iii)1000 Å of Pt @ 3 Å/s.

** Due to the high temperature in Pt deposition, large tensile stress will develop after the fast cooling. Therefore, thick Ti layer is required for better adhesion.*

** Slow deposition rate will help Ti to become more compact and adhesive.*

** Pt deposition releases bright light. Use protecting glasses near EVAP when looking into the chamber.*

** When doing Pt deposition, be careful of the e-beam position. Make sure e-beam hits on the metal.*

(5) Lift-off by acetone:

** It is recommended to put the whole cassette into the big plastic tank filled with acetone. Keep the cassette vertical so that the metal shreds can come off under the effect of gravity.*

(a) Peel the kapton tape off.

(b) Acetone dwell:

(i) Submerge substrates into acetone.

(ii) Should see metal shreds come off quickly right after submerging.

(iii) Better dwell for overnight.

(c) "Cat ear" treatment and clean:

(i) (Next day) Take 2 small glass containers (G-1 and G-2) and 1 big container (G-3).

(ii) Fill ~1/5 of the small G-1 with acetone.

(iii) Fill ~1/5 of the small G-2 with IPA.

(iv) Fill ~1/3 of the large G-3 with DI water.

(v) Do sonicating bath on wafer samples <u>one by one</u>:

-1- Rinse off metal shreds with DI water gun.

-2- Acetone bath for 1 minute.

-3- IPA bath for 1 minute.

-4- DI water bath for 1 minute.

(vi) Cascade and spin dry.

(6) Quality check: **[Nikon microscope]** check metal patterning.

** Here we use positive resist for lift-off instead of negative resist. Because negative resist will leave residue after developing, making the metal layer easy to come off. Furthermore, the resist is not easy to dissolve in acetone. As a result, the lift-off will become very slow and annealing will fail because of the residue resist on the wafer.*

** Due to doing lift-off by positive resist, long "cat ear" may exist along the pattern boundaries. These "cat ear" can grow as large as 9 µm, which can be seen by bare eyes.*

Fortunately, "cat ear" can be physically broken by sonicating bath, leaving much smaller "cat ear" residue, which can be flattened by the later annealing.

5. Bottom electrode annealing

(1) Cut testing wafer into four quarter pieces. Take one piece out of clean room for each trial.

**Can cut further into smaller pieces if necessary.*

(2) **[Box furnace]** Anneal:

(a) Use air nozzle to blow off any shreds on the testing sample.

(b) Place the quarter sample on the glass boat. Insert the boat into the furnace, with the boat end about 1 cm from the furnace chamber end.

(c) Anneal by the following recipe:

Target (^oC)	Time (hr : min)	Comments
150	0:10	Raise and stabilize at 150°C. This step is to make sure all the annealing start from 150°C.
150	0:20	
$\mathbf{T_{dwell}}$ = 790 ?	1:00	Relatively slow and steady ramp up.
$\mathbf{T_{dwell}}$ = 790 ?	1:00	Dwell for 1 hr to fully relax Ti and Pt.
200	9:00	Extremely slow ramp down. DO NOT turn off the furnace at this step. Slow ramping rate should be kept
25	0:10	Power shut down and naturally cools down.
25	OFF	
Total time = 11 hr 40 min		

**The box furnace starts from current temperature by default, which introduces an uncertainty to the recipe, especially when the box furnace is still hot (such as 100 ^{o}C compared with normally 25 ^{o}C at room temperature). The first two steps are to ensures the box furnace always starts from 150 ^{o}C.*

** It is recommended to change only the dwell temperature if any adjustment is required (i.e., T_{dwell}). Long time dwell and extremely long time ramp down is essential for successful annealing.*

** For the whole annealing process:*

a) Substrate starts with large tensile stress due to the high deposition temperature and rapid cool down in Pt deposition.

b) When ramp up to about 250c, the tensile stress in Pt deposition is almost released.

c) As temperature continues to climb up, compressive stress develops. But the compressive stress is not able to accumulate due to the high mobility of the metal atoms and the slow ramp up rate. Because the metal layer is confined by wafer boundary, as a result, metal layers grow in Z-direction, causing the thickness to increase. i.e., the slow growing of the metal layer cancels out the compressive stress developed by metal expansion.

d) After 60 min of dwell at target temperature, all metal stress is expected to be released.

e) As temperature ramps down, tensile stress develops again. Metal will experience multiple times of: elastic deformation => plastic deformation & Pt open-up & tensile stress releasing. As metal cools down and mobility decreases, the above process becomes slower and slower. i.e., <u>An extremely slow and steady ramp down rate is crucial to produce a smooth and evenly annealed Pt layer.</u>

f) Furnace door can be opened under 200c, and substrate can be taken out under 100c. Use thermal proof gloves, the cassette may still be hot!

(3) [SEM] Exam annealing results by “LouisLiu: Semiconductor Conductive” recipe.
The porosity should be similar to the following picture. (under 5000x)

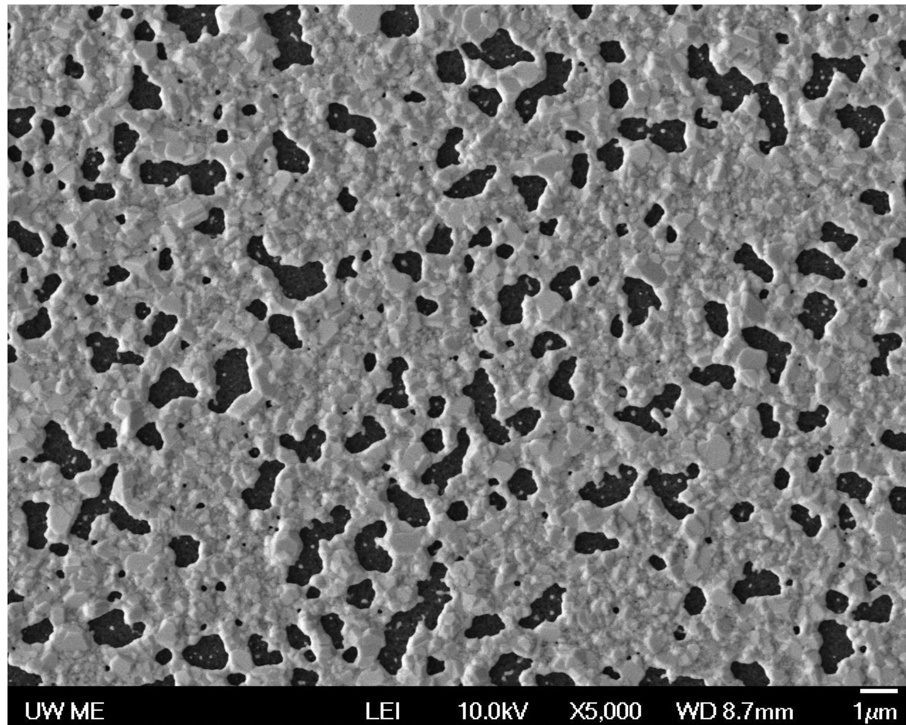

Typical situations of failure are shown by the following three pictures.

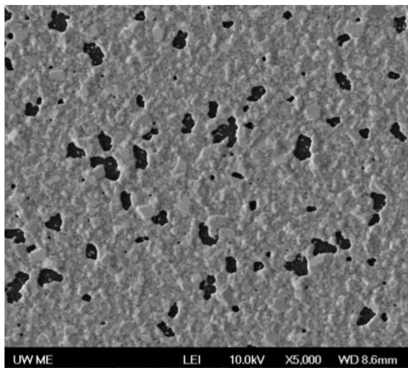

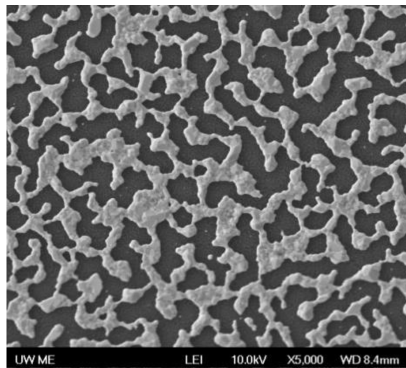

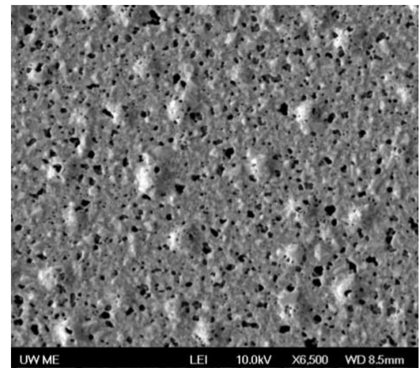

(a)Under Anneal (b)Over Anneal (c)"Bubble"

(a) Under Annealing is usually because the temperature is too low.

(b) Over Annealing is usually because the temperature is too high.

(c) "Bubble" is usually because the dwell time is too short.

If using the recommended recipe, this is not likely to happen.

(4) If annealing result is not good, adjust the dwell temperature and try another testing sample.

If annealing result is good, anneal samples by the successful recipe.

(5) [SEM] Exam the annealing result:

For each wafer, exam and take pictures for all the 4 sections (up, down, left and right).

6. PZT Sol Making

Refer to [28]: Appendix A - 5.0

<u>After sol gel is made, sit for 3 days before deposition.</u>

7. PZT Deposition and Sintering

(in clean room)

(1) Wafer clean:

(a) Sonicating bath with Acetone for 1 min.

(b) Sonicating bath with IPA for 1 min.

(c) Sonicating bath wit DI water for 1 min.

(d) Cascade and spin dry.

(outside of clean room)

(2) Preparation:

- one vial of PZT sol.
- bag of one-time pipettes
- 1/2” wide kapton tapes.
- craft knife, fine tip tweezers, wafer tweezers, long tweezers
- thermal proof gloves
- wipes, aluminum foil (should be available in lab)

(3) Furnace pre-heat:

(a) Put glass cassette into box furnace chamber.

(b) Set and run the following recipe on box furnace:

Target (c)	Time (hr . min)
660	0.00
660	>5.00

**This will tell the box furnace to ramp to 660 ^{o}C quickly and dwell that that temperature. This typically takes 10-20 min. During the ramping up, one can continue to do spin coater preparation.*

**Although 650 ^oC is previously used as sintering temperature in Probe V1 fabrication, that temperature is not good for box furnace. The chamber of the box furnace is small and shallow, the temperature usually drops by 20 ^oC every time the door is open at >600 ^oC. Therefore a slightly higher temperature is utilized to somehow compensate for the temperature drop and help the temperature to recover to higher than 650 ^oC quickly.*

(4) Spin coater preparation:

(a) Cover the spinner bowl with aluminum foil.

(b) Open the air valve. The spin coater will be automatically powered on.

(c) The spin recipe should be stored as “Recipe 2”. Double check the parameters:

(i) Ramp(s): 01.0
Dwell(s): 15
RPM: 15

**The spin coater will run a vacuum check every time before spin. If the vacuum check is not passed, the spin will not start. This will cause problem if one has already applied PZT sol to the sample. To prevent this, the first step spins at extremely low speed for 15 s to allow the system to do vacuum check. In this way, one can apply the PZT sol AFTER vacuum check is passed. Make sure to finish PZT sol application in 15 s.*

(ii) Ramp(s): 02.0
Dwell(s): 3
RPM: 500

** Fairly low spin speed for a short 5 s to spread the PZT sol out.*

(iii) Ramp(s): 02.0
Dwell(s): 18
RPM: 4500

** The high spin is to make sure the PZT sol layer is thin enough so that the liquid can be evaporated instantaneously in the sintering step.*

(iv) Ramp(s): 03.0
Dwell(s): 1
RPM: 0

**Slow down and stop in 3 s.*

(d) Use the whole wafer spin holder (the Teflon one), and run test spin on dummy wafer first. **DO NOT use smaller wafer holders, those wafer holders localized vacuum at the center, which will curve the wafer, causing uneven PZT sol distribution (center being thicker).*

(e) Wait for the temperature to reach 660 ^{o}C.

(5) Do the deposition and sintering by following the sequential steps below (i.e., two samples at a time):

-1- Tape sample with kapton tape as the following picture (follow the sequence from “1” to “7”, so that one can peel the tape off quickly after spin coating by starting from “1”).

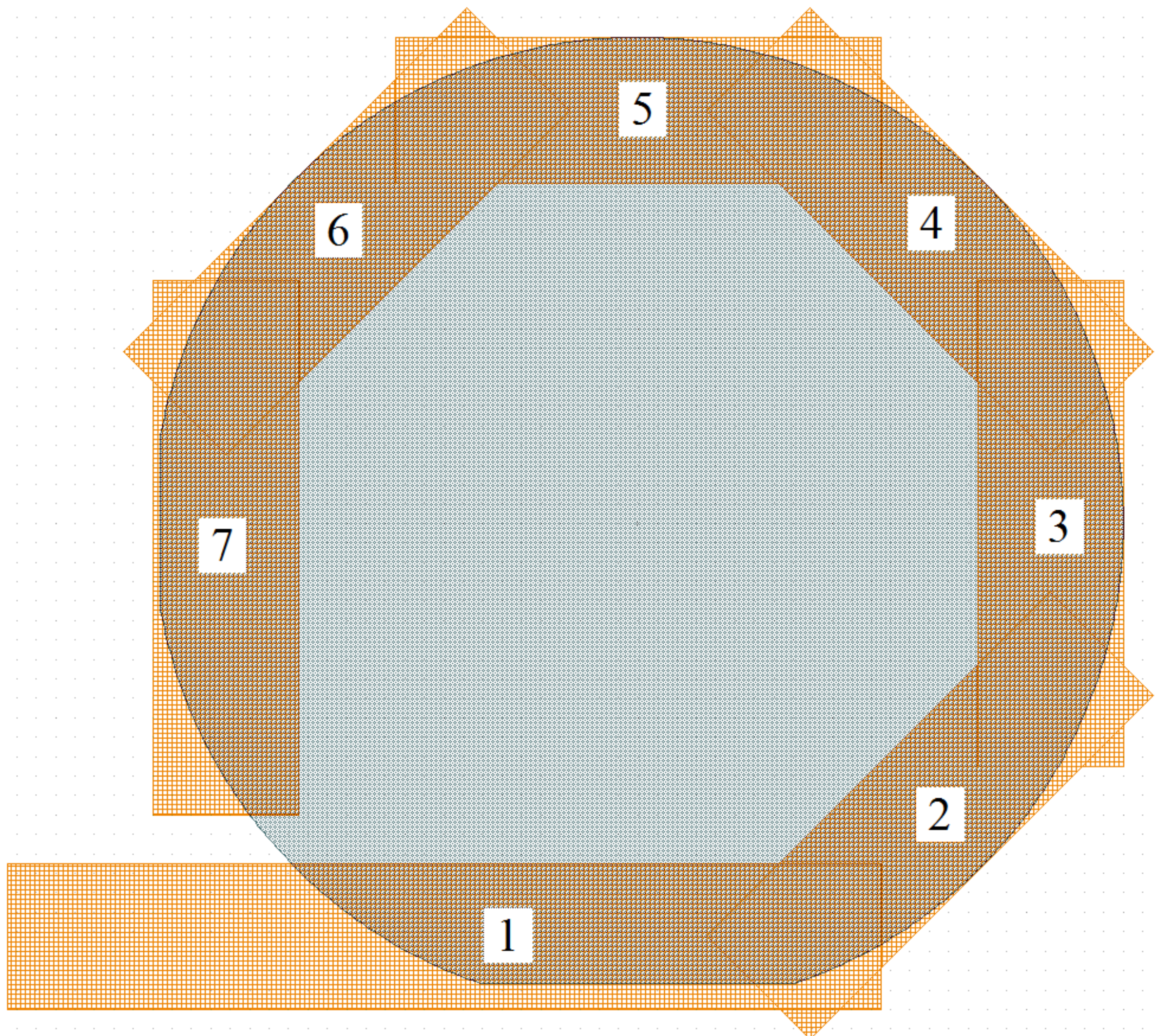

-2- Blow dust off the wafer using air nozzle.

-3- Spin coat PZT sol on sample using the pre-set spinning recipe.

-4- Quickly peel off the kapton tape. (i.e., start from tape “1”)

-5- Put on thermal gloves and tweeze sample by the long tweezers.

-6- Open box furnace door, quickly put sample in and close the box furnace door.

-7- Set timer = 15 min, monitor the temperature of the box furnace. Start timer when the temperature is above 630 ^{o}C.

-8- Wait for 15min sintering for the sintering to complete. (Can start processing the second sample as is shown in the sequential table below.)

-9- After 15 min is done, put on thermal gloves, use the long tweezers to take sample out. CAUTION: sample is very hot, DO NOT use hand! Hold the sample by tweezers in ambient air for at least 45s before putting sample back.

-10- PZT is not able to adhere well on silicon nitride, blow off PZT shred on sample surface using the air nozzle.

The sequential table:

Samples	Do above steps in the following order																	
Sample-A	1-7	8	9-10		1		2-7	8	9-10		1		2-7	8	9-10			
Sample-B		1		2-7	8	9-10		1		2-7	8	9-10		1		2-7	8	9-10

**Namely, each sample has gone through 3 layers of PZT deposition.*

(in clean room)

(6) Clean the samples: spin rinse & dry.

(7) **[Nikon microscope]** inspect the samples.

The following 3 pictures show: (a) a successful deposition (b) successful deposition with PZT shreds (forget to blow off the PZT shred as in “step -10-”) (c) PZT deposition failure due to craking.

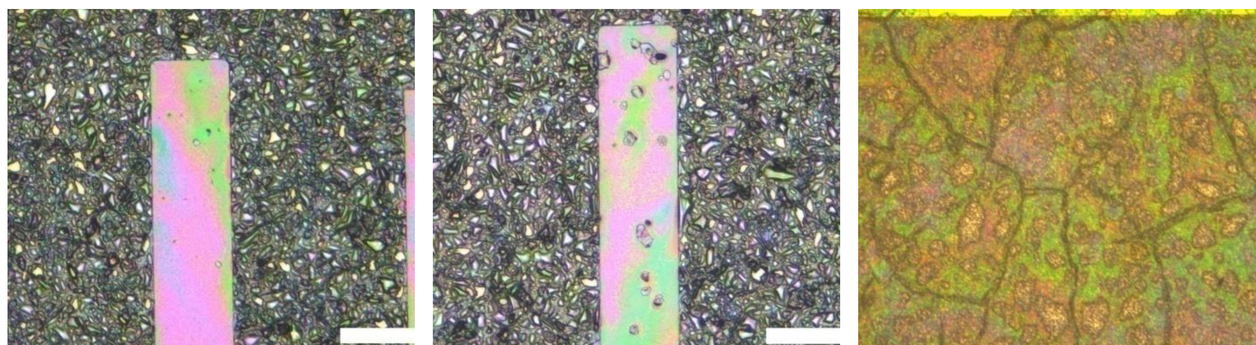

(a) Successful deposition (b) PZT shred not blown off (c) PZT layer crack

8. PZT patterning by etching

(1) Wafer clean: Cascade + Spin dry

**No EKC830 clean after PZT deposition.*

(2) **[HMDS oven]** HMDS adhesion layer application: run the standard recipe.

(3) Pattern by lithography:

(a) **[Spin-1 or 2]**:

(i) Resist: AZ-9260

Time (s)	Target (rpm)	Ramp (rpm/s)
5	500	250
45	3000	1000

(ii) Soft bake: 110°C for 90s, contact bake with vacuum.

(b) Exposure:

(i) By the “PZT Etching” mask

(ii) **[EVG aligner]** Time = 45s.

**If using ABM aligner, the exposure time = 39s.*

(iii)Develop: AZ400k:DI = 1:4 for 3 min 30 s with agitation.

(iv) **[Nikon microscope]** Exam pattern quality under green light.

(4) PZT etching:

(a) Preparation:

(i) Take two small Teflon containers (T-1 and T-2), and one large glass container (G-1). Wipes, the wafer cassette and tweezers.

(ii) Fill ~1/5 of the container T-1 with 10:1 BOE.

Fill ~1/5 of the container T-2 with 37.5% HCl.

Fill ~1/2 of the container G-1 with DI water.

(iii) Turn on the Cascade.

(b) Do etching one wafer at a time:

(i) Submerge into container T-1 (10:1 BOE) and dwell for 15minutes.

(ii) Submerge into container T-2 (37.5% HCl) and dwell for 2 minutes.

(iii) Submerge into container G-1 (DI water) and dwell for 5 minutes.

(iv) Add the substrate to the cassette and cascade.

(v) After all wafers are done, spin rinse and dry the whole cassette.

(c) Pattern cleaning:

(i) Sonicating bath by Acetone + IPA + ID water.

**Do not use EKC bath!*

(ii) Cascade and Spin dry.

(5) Quality check by **[Nikon]** optical microscope:

*Check the dimensions of etching undercut.

*Check the if all PZT is etched in the open areas.

9. Top electrode deposition and patterning

(1) Wafer clean: Cascade + spin dry.

(2) **[HMDS oven]** HMDS adhesion layer application: run the standard recipe.

(3) Pattern by lithography:

(a) **[Spin-1 or 2]**:

(i) Resist: NR 7-1000PY

**Use negative resist for better resolution.*

Time (s)	Target (rpm)	Ramp (rpm/s)
5	500	250
40	3000	1500

(ii) Soft bake: 150°C for 60s, contact bake with vacuum.

(b) Exposure:

(i) By the “Cr & Au negative” mask

(ii) **[EVG aligner]** Time = 35s.

**If using ABM aligner, the exposure time = 30s.*

(iii) Hard bake: 100°C for 60s, contact bake with vacuum.

* *Do not forget this step!*

(iv) Develop: RD-6 or AD10 for 30 s with agitation.

(v) **[Nikon microscope]** Exam pattern quality under green light.

** Make sure no residual resist in open area.*

(4) Cr & Au deposition:

(a) N_2 gun blow right before substrate loading.

(b) 250 Å of Cr @ 1 Å /s.

(c) 5000 Å of Au @ 5 Å/s.

** When doing Au deposition, set initial deposition rate = 1Å/s, and then gradually increase to 5 Å/s.*

(5) Lift-off by acetone:

** It is recommended to put the whole cassette into the big plastic tank filled with acetone. Keep the cassette vertical so that the metal shreds can come off under the effect of gravity.*

(a) Acetone dwell:

(i) Submerge substrates into acetone.

(ii) Should see metal shreds come off quickly right after submerging.

(iii) Better dwell for overnight.

(b) Sonicating bath by acetone and DI water.

(c) Cascade and spin dry.

(d) **[Nikon microscope]** Exam pattern quality.

10. Front Side DRIE

**This step is to partially etch the two diaphragm slots and the probe separation lines for future through etching by the backside DRIE.*

(1) Wafer clean: Cascade + Spin dry

(2) **[HMDS oven]** HMDS adhesion layer application: run the standard recipe.

(3) Pattern by lithography:

(a) **[Spin-1 or 2]**:

(i) Resist: AZ-9260

Time (s)	Target (rpm)	Ramp (rpm/s)
5	500	250
45	1200	1000

**Result in 11-13 µm thick photo-resist.*

(ii) Soft bake: 110°C for 165s, contact bake with vacuum.

(b) Exposure:

(i) By the "Front Side DRIE" mask

(ii) **[EVG aligner]** Time = 108s.

**If using ABM aligner, the exposure time = 94s.*

(iii)Develop: AZ400k:DI = 1:4 for 7 min with agitation.

(iv) **[Nikon microscope]** Exam pattern quality under green light.

(4) **[Vision RIE]** Etch exposed silicon nitride and silicon oxide.

(a) Tape the whole backside surface by blue kapton tape to protect from accidental etching.

(b) By "MFF: Silicon Nitride Etch" recipe, time = 5 min.

(c) Take out and exam by bare eyes: should be purple (i.e., color of silicon oxide).

(d) Again by "MFF: Silicon Nitride Etch" recipe, time = 15 min.

(e) Observe the color of the exposed area:

IF: color is not grey, adjust the positions of wafers and etch another 3 min.

IF: color is grey, silicon is exposed. Ready for the next step.

(5) **[DRIE]** Etch the front side by 50 µm:

(a) Choose recipe: "MFF Standard DRIE".

(b) Set number of loops = 24, and run the recipe.

(c) Rotate the substrate by 120° and do another etching for 24 loops.

(d) Rotate the substrate again by 120° and do another etching for 24 loops

**The DRIE etching rate is approximately 0.7 µm/loop. To etch 50 µm of silicon, need 50 / 0.7 = 72 loops. Therefore, we do 24 loops × 3.*

** The DRIE etching time rate is 5 loops/min. That means the total etching time for each 24 loops should be about 5 min (preparation) + 24 / 5 = 10 min.*

(6) Peel off the blue kapton tape.

(7) Clean the substrate:

(a) Acetone bath for 3 min with agitation.

(b) Cascade and spin dry.

(8) Measure the actual etching depth by **[P-15]** profilometer.

Acceptable if depth is 45-55 μm.

11. Backside DRIE

(1) Wafer clean: Cascade + Spin dry

(2) **[HMDS oven]** HMDS adhesion layer application: run the standard recipe.

(3) Spin coat on the **front side**:

(4) **[Spin-1 or 2]**:

(a) Resist: AZ-9260

Time (s)	Target (rpm)	Ramp (rpm/s)
5	500	250
45	3000	1000

(b) soft bake: 110ºC for 80s, contact bake with vacuum.

(5) Tape the whole front side surface by **blue kapton tape**.

(6) Pattern the **backside** by lithography:

(a) **[Spin-1 or 2]**:

(i) Resist: AZ-9260

Time (s)	Target (rpm)	Ramp (rpm/s)
5	500	250
45	1200	1000

**Result in 11-13 μm thick photo-resist.*

(ii) Soft bake: 110ºC for 165s, contact bake with vacuum.

(b) Exposure:

(i) By the "Backside DRIE" mask

(ii) **[EVG aligner]** Time = 108s.

**Still use front side alignment. Align to the backside shallow patterns done in step-2.*

**If using ABM aligner, the exposure time = 94s.*

(iii) Peel off the **blue kapton tape**.

(iv) Develop: AZ400k:DI = 1:4 for 7 min with agitation.

(7) **[Nikon microscope]** Exam pattern quality under green light.

(8) Carve the front **side blue tape** along the red lines shown below in the highlighted areas:

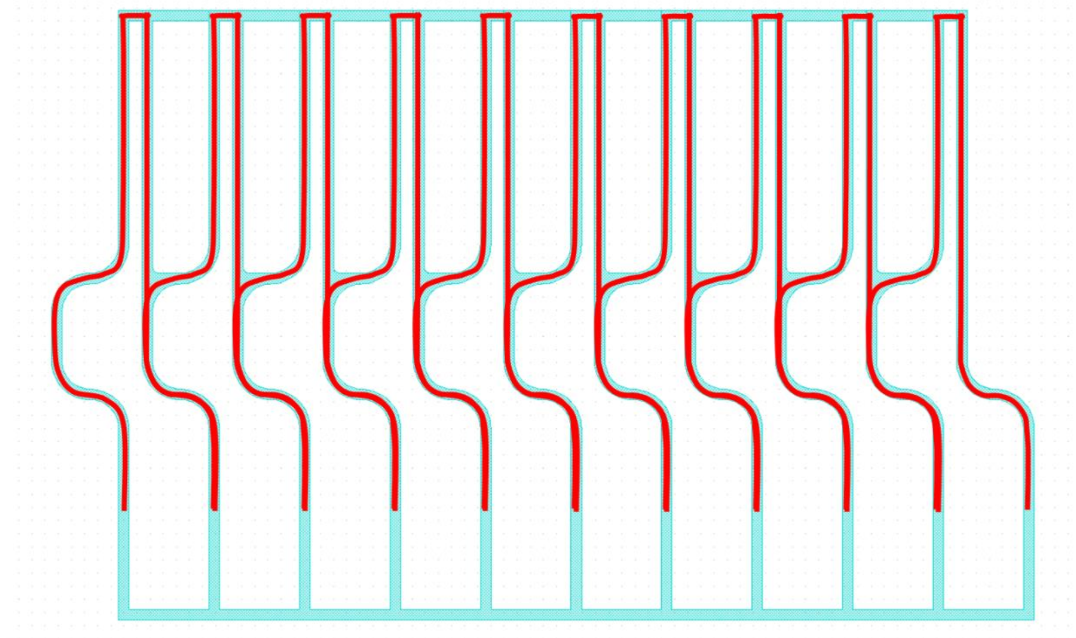

**The backside etching is non-uniform. That means the diaphragm will not form at the same time for different probes. Therefore, it is necessary to be able to release the probes from the substrate individually. The carve at the front side blue kapton tape will release most of the areas.*

**A small portion is still left un-carved because the probes still need to be connected to the substrate at this stage. Otherwise, the probes are likely to accidentally released in DRIE chamber.*

(9) Tape the whole surface of the buffer silicon wafer by **blue kapton tape**.

(10) Attach the blue tape side of the buffer silicon wafer to **the front side** of the sample substrate (i.e., two blue kapton taped sides attached together). Fix the attach by **kapton tapes.**

** Note that there is no photo-resist or any adhesion layers between the substrate and the sample wafer. This is for the later individual lease.*

(9) **[DRIE]** Course Etch the front side by ~ 220 μm:

(a) Choose recipe: "MFF Standard DRIE".

(b) Set number of loops = 105, and run the recipe.

(c) Check the actual etching depth by **[P-15]** profilometer.

- Target etching depth = 80 ~ 85 μm.

(d) Rotate the substrate by 120° and do another etching for 105 loops.

(e) Check the actual etching depth by **[P-15]** profilometer.

- Target etching depth = 150 ~ 160 μm.

(f) Rotate the substrate again by 120° and do another etching for 105 loops.

(g) Exam the etching results by **[Nikon]** optical microscope.

- Should see through etched at diaphragm slots and separation lines.
- The diaphragm area is released but the diaphragm is not yet formed.

**The DRIE etching rate is approximately 0.7 μm/loop. To etch 220 μm of silicon, need 220 / 0.7 = 315 loops. Therefore, we do 105 loops × 3.*

** The DRIE etching time rate is 5 loops/min. That means the total etching time for each 24 loops should be about 5 min (preparation) + 105 / 5 = 26 min.*

** By etching 220 μm down into the silicon from the backside. The area gone through the front side DRIE (i.e., the diaphragm slots and the separation lines) will have total etching of 220 + 50 = 270 μm > 250 μm => Through etched! The other open areas (i.e., the diaphragm central areas) will have total etching of 220 μm < 250 μm, which is not through etched.*

(11) Use blue tape to tape the area shown below to secure the probes on substrates.

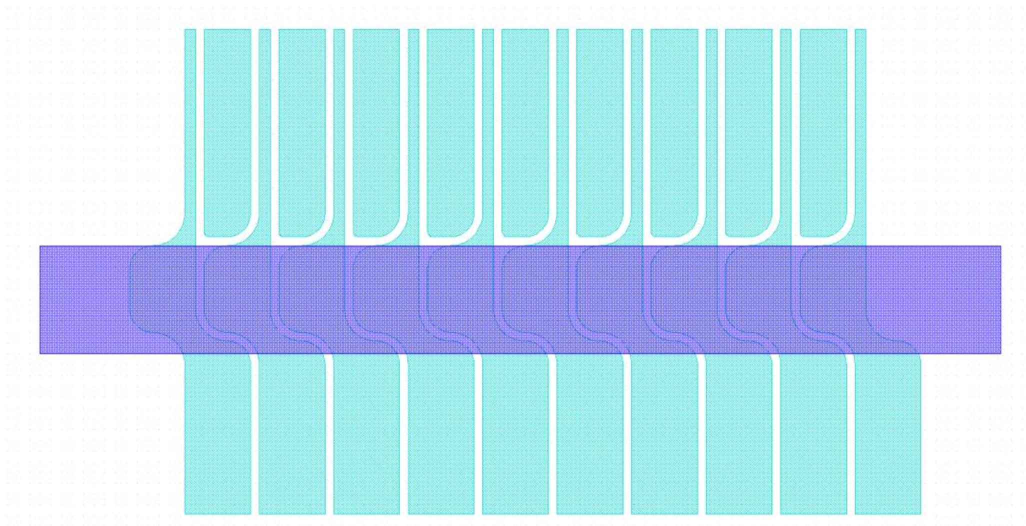

(12) **[DRIE]** Slow etch to form thin diaphragms:

(a) Choose recipe: “MFF Standard DRIE”.

(b) Set number of loops = 10, and run the recipe.

(c) Exam the etching results by **[Nikon]** optical microscope.

- IF: No front side silicon oxide (purple color) is exposed => repeat (a) - (c).
- IF: Front side silicon oxide is exposed, continue to (d).

(d) Exam the etching results by **[Nikon]** optical microscope **one by one**. For each probe:

- IF: the area is large enough (ideally expand to total width of the diaphragm.), Continue to (e).
- IF: the area is not large enough, etch another 2 - 3 loops and repeat (d).

(e) Carve the secure blue kapton tapes of the finished probe and release the probe from the substrate.

(f) Re-connect the carved parts as below:

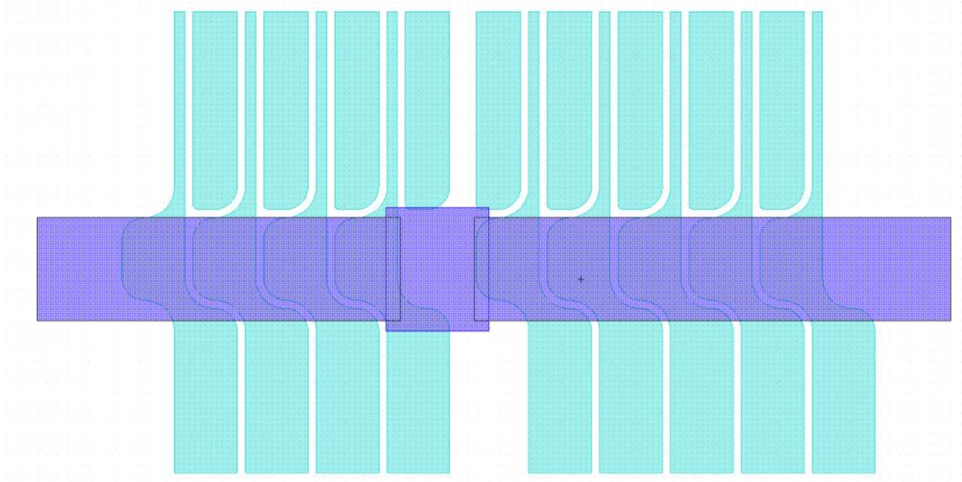

(g) Etch another 2 - 3 min and repeat (d) - (f), until all the probes are released.

**The etching in this step should be very slow to avoid over etching.*

**It is important to exam the result very time after etching to remove the finished probes in time.*

12. Release of Probes and Finish

**Probes are still attached by photo-resist and blue kapton tape. This step is to strip off these two layers.*

(1) Take two small containers: one glass container (G-1), one container with lid (T-1).

(2) Fill 1/2 of both containers with acetone.

(3) Submerge the previously released probes into the glass container G-1.

- Most of the photo-resist will dissolve in acetone quickly.
- The blue kapton tapes will automatically be released and roll up.

- Wait until all the blue kapton tapes are separated from the probes.

(4) Transfer to the other container (T-1).

(5) Dwell for 2 days.

**Long dwell time is required, because photo-resist is hard to dissolve in the diaphragm areas.*

(6) (After the dwell) Take one large glass container and fill 2/3 with DI water.

(7) Transfer the probes to the large glass container.

(8) Transfer probes to a wipe and dry naturally.

(9) Exam probes one by one using **[Nikon]** optical microscope for both the front side and the backside.